

國立臺灣大學 理學院物理學研究所

碩士學位論文

Graduate Institute of Physics

College of Science

National Taiwan University

Master Thesis

在KOTO實驗中尋找無質量暗光子： $K_L^0 \rightarrow \gamma\bar{\gamma}$

Search for a massless dark photon in  $K_L^0 \rightarrow \gamma\bar{\gamma}$  at the  
KOTO Experiment

吳桐

Tong Wu

指導教授：熊怡 教授

Advisor: Yee Bob Hsiung, Ph.D.

中華民國113年8月

August 2024



NATIONAL TAIWAN UNIVERSITY

MASTER THESIS

**Search for a massless dark photon in  
 $K_L^0 \rightarrow \gamma\bar{\gamma}$  at the KOTO Experiment**

*Author:*

Tong Wu

*Supervisor:*

Dr. Yee Bob HSIUNG



July 27, 2024

© 2024, by Tong Wu  
tong@hep1.phys.ntu.edu.tw



ALL RIGHTS RESERVED





# Acknowledgements

Thanks all

DRAFT



## 中文摘要

一二三

三二一

關鍵詞：暗光子、新物理。

DRAFT



# Abstract

This thesis presents the search for the massless dark photon ( $\bar{\gamma}$ ) in the  $K_L^0 \rightarrow \gamma\bar{\gamma}$  decay at the J-PARC KOTO experiment, based on the special run data collected in 2020.

Distinguished from the massive dark photon, the massless one does not directly mix with the ordinary photon but could interact with Standard Model (SM) particles through direct coupling to quarks. Some theoretical models propose that the branching ratio ( $\mathcal{BR}$ ) of the  $K_L^0 \rightarrow \gamma\bar{\gamma}$  decay could reach up to  $\mathcal{O}(10^{-3})$ .

The number of  $K_L^0$  decays that had been collected in the special run is estimated to be  $(1.29 \pm 0.02) \times 10^{10}$ . The single event sensitivity is calculated to be  $(2.91 \pm 0.02_{stat.} \pm 0.30_{syst.}) \times 10^{-8}$ . The total background level prediction is  $(12.66 \pm 4.42_{stat.} \pm 2.13_{syst.})$  with the agreement from the side-band region. We uncovered the blind region and observed 13 events. The Feldman-Cousins method is used to calculate the upper limit of the  $K_L^0 \rightarrow \gamma\bar{\gamma}$  branching ratio to be  $< 3.47 \times 10^{-7}$ (90%C.L.).

**Keywords:** Dark Photon, beyond Standard Model.



# Contents

<b>Approval</b>	i
<b>Acknowledgements</b>	iii
中文摘要	v
<b>Abstract</b>	vii
<b>Contents</b>	ix
<b>List of Figures</b>	xiii
<b>List of Tables</b>	xvii
<b>1 Introduction</b>	1
1.1 Dark Matter and Dark Photons . . . . .	1
1.2 Theoretical Predictions . . . . .	1
1.3 Basic Strategy of the $K_L^0 \rightarrow \gamma\bar{\gamma}$ Search . . . . .	2
1.3.1 Signal Identification . . . . .	2
1.3.2 Major Background Sources . . . . .	2
1.4 Thesis Overview . . . . .	3
<b>2 KOTO Experiment</b>	5
2.1 J-PARC and Proton Beamline . . . . .	5
2.2 $K_L^0$ Beamline . . . . .	6
2.3 Detectors . . . . .	7
2.3.1 CsI . . . . .	8
2.3.2 Charge Veto Counter . . . . .	10
2.3.3 Barrel Veto Counter . . . . .	10
2.4 Data Acquisition System . . . . .	12
<b>3 Event Reconstruction</b>	13
3.1 Photon Cluster Finding . . . . .	13
3.2 Reconstruction of $\pi^0$ . . . . .	15
3.3 Reconstruction of Decays . . . . .	16
3.3.1 Reconstruction of $K_L^0 \rightarrow 3\pi^0$ . . . . .	17
3.3.2 Reconstruction of $K_L^0 \rightarrow \gamma\bar{\gamma}$ . . . . .	18
3.3.3 Correction for Energy and Position of Photon Clusters . . . . .	18
3.4 Veto Hit Reconstruction . . . . .	20
3.4.1 Barrel Veto Counters . . . . .	21

3.4.2	CsI Calorimeter . . . . .	22
<b>4</b>	<b>Monte Carlo Simulation</b>	<b>25</b>
4.1	GEANT4 toolkit . . . . .	25
4.2	Detector Response . . . . .	26
4.3	Pulse Simulation . . . . .	26
4.4	$K_L^0$ Generation . . . . .	26
4.4.1	Beamline Simulation . . . . .	26
4.4.2	Empirical $K_L^0$ Spectrum Simulation . . . . .	27
4.5	Fast Simulation . . . . .	28
4.6	Accidental Overlay . . . . .	29
4.7	Neutron background Simulation . . . . .	30
<b>5</b>	<b><math>K_L^0</math> Yield Estimation</b>	<b>31</b>
5.1	Data Set . . . . .	31
5.2	Event Selections . . . . .	32
5.2.1	Trigger Cut . . . . .	32
5.2.2	Photon Selection . . . . .	32
5.2.3	$K_L^0$ Selection . . . . .	34
5.2.4	Veto Cut . . . . .	36
5.3	Yield Estimation . . . . .	37
5.3.1	Estimation by $K_L^0 \rightarrow 3\pi^0$ Decays . . . . .	38
5.4	Summary of $K_L^0$ Yield Estimation . . . . .	38
<b>6</b>	<b>Analysis of <math>K_L \rightarrow \gamma\bar{\gamma}</math></b>	<b>43</b>
6.1	Data Set . . . . .	44
6.2	Basic Strategy of the Single Cluster Study . . . . .	45
6.2.1	Signal Identification . . . . .	45
6.2.2	Major Background Sources . . . . .	45
6.3	Single Cluster Event Selection . . . . .	46
6.3.1	Trigger Selection . . . . .	46
6.3.2	Kinematic Cuts . . . . .	47
6.3.3	Veto Cuts . . . . .	48
6.4	Background Suppression . . . . .	50
6.4.1	$K_L$ Decay Background . . . . .	50
6.4.2	Neutron Background . . . . .	53
6.5	Single Event Sensitivity . . . . .	58
6.5.1	Systematic Uncertainty of SES . . . . .	59
6.6	Additional Background Source Study . . . . .	59
6.7	Background Level Estimation . . . . .	61
6.8	Unbind the Signal Region . . . . .	61
<b>7</b>	<b>Conclusion and Discussion</b>	<b>63</b>

7.1 Discussion for Next Step . . . . .	64
7.2 Massive Dark Photon Search . . . . .	64
<b>Bibliography</b>	<b>65</b>



# List of Figures

2.1	The entire view of J-PARC. [5]	5
2.2	Illustration of the Hadron Experimental Facility (HEF) at J-PARC.[9] The KL in the Figure indicated the KOTO detector	6
2.3	Structural drawings of the T1 production target [10]. One bar is used for production and the other is a spare.	7
2.4	Schematic diagram of the $K_L^0$ beamline.[11]	7
2.5	Beamline layout	8
2.6	Schematic diagram of CsI layout.	9
2.7	KOTO detector layout	10
2.8	The Schematic Diagram of Charge Veto Structure.	11
2.9	The Schematic Diagram of Barrel Veto Structure. Figure courtesy of [15].	11
2.10	The architecture of the KOTO DAQ system. [16]	12
3.1	The illustration of the cluster finding process. All the color crystals are the seed crystals, and the crystals with the same color belong to the same cluster. The black crystal is the isolated crystal hit.	14
3.2	Timing boundary for a cluster seed based on the scattered plot of crystal timing versus energy deposit. A Gaussian function is fitted at each energy bin and the boundary is defined by $\mu \pm 5\sigma$ , where $\mu$ and $\sigma$ are the Gaussian mean and standard deviation. The orange points indicate the boundary at the associated energy bin. The red curve connects all the points for the interpolation of the boundary value between the points. (Figure courtesy of [15])	15
3.3	The schematic diagram of the $\pi^0 \rightarrow 2\gamma$ decay process.	16
3.4	The schematic diagram of the $K_L^0$ travel and decay process and geometry relationships	18
3.5	The schematic diagram of the correction of the photon cluster position.	19
3.6	Schematic view of the timings used in the module-veto-timing calculation.	21
3.7	The Schematic diagram of a photon hit with the generated scintillation lights propagating to both directions and captured by PMTs. Figure courtesy of [15]	22
3.8	The Schematic diagram of geometry relationships of the Barrel veto counter.	22
4.1	Beam content at the KOTO detector entrance based on the beamline simulation. Figure courtesy of [15]	27

4.2	The $K_L^0$ momentum spectrum at the exit of the second collimator. Figure courtesy of [15] . . . . .	28
4.3	Comparison of $K_L^0$ beam profile at the exit of the second collimator between the beamline simulation and the empirical model. Figure courtesy of [15] . . . . .	28
4.4	An example of the accidental overlay on a simulated pulse, subtracting the pedestal. Figure courtesy of [15] . . . . .	30
5.1	Distribution of the photon selection variables for the $K_L^0 \rightarrow 3\pi^0$ decay. The photon selection cuts are applied except for the variable shown in the plot. The black point shows the data, and the fill histogram shows the Monte Carlo simulation. The red arrow indicates the cut-off value of the variable.	33
5.2	Distribution of the $K_L^0$ selection variables for the $K_L^0 \rightarrow 3\pi^0$ decay. The photon and $K_L^0$ selection cuts are applied except for the variable shown in the plot. The black point shows the data, and the fill histogram shows the Monte Carlo simulation. The red arrow indicates the cut-off value of the variable. . . . .	34
5.3	Distribution of the $K_L^0$ selection variables for the $K_L^0 \rightarrow 3\pi^0$ decay. The photon and $K_L^0$ selection cuts are applied except for the variable shown in the plot. The black point shows the data, and the fill histogram shows the Monte Carlo simulation. The red arrow indicates the cut-off value of the variable. . . . .	35
5.4	Distribution of isolated crystal hit energy(E) vs. its distance(D) from the nearest cluster. The red line shows the cut based on Equation 5.2. The sample was obtained from the $K_L^0 \rightarrow \pi^0\nu\bar{\nu}$ Monte Carlo simulation.[23] .	38
5.5	Beam profile at the exit of the second collimator via the $K_L^0 \rightarrow 3\pi^0$ decay analysis. All the selection cuts are imposed. Filled histograms are predicted by the Monte Carlo simulation. . . . .	39
5.6	Distribution of the kinematic variables for the $K_L^0 \rightarrow 3\pi^0$ decay. All the selections are applied except the variable shown in the plot. The black point shows the data, and the fill histogram shows the Monte Carlo simulation. The red arrow indicates the cut-off value of the variable. . . . .	40
5.7	Distribution of the kinematic variables for the $K_L^0 \rightarrow 3\pi^0$ decay. All the selections are applied except the variable shown in the plot. The black point shows the data, and the fill histogram shows the Monte Carlo simulation. The red arrow indicates the cut-off value of the variable. . . . .	41
6.1	Distribution of cluster timing after relative timing correction. The dot is from real physics data, and the filled histogram is the MC simulation. The red arrow is the cut-off region. . . . .	46
6.2	Distribution of total energy from Monte Carlo simulation. The histogram area is normalized to 1. The red arrow is the cut-off region. . . . .	47

6.3	An upstream view of the CsI calorimeter. The red region is the outermost boundary, while the blue region is the innermost boundary. . . . .	48
6.4	Distribution of veto timing of CC06. . . . .	49
6.5	Temporary plots of FBAR and NCC . . . . .	51
6.6	The schematic geometry diagram of the mechanism of the upstream decay background. . . . .	52
6.7	$E_\gamma - R_{XY}$ distributions of scattered $K_L^0 \rightarrow 2\gamma$ decays with various cut. The red frame indicates the signal region. The red number indicates the background level in each region. . . . .	52
6.8	The schematic geometry diagram of the mechanism of the fusion cluster background. . . . .	53
6.9	$E_\gamma - R_{XY}$ distributions of various background sources after applying all selection cuts. Left-hand side plots exclude the neutron cuts and the right-hand side plots include it. The red frame indicates the signal region. The red number indicates the background level in each region. (Region A indicates the Signal Region and Region B indicates the Blind Region excluding the signal region.) . . . . .	54
6.10	Example of the energy and timing shapes of photon cluster from the Monte Carlo simulation and neutron cluster from data. The color code represents the deposited energy in MeV and the timing in nanoseconds for each crystal in the cluster. [24] . . . . .	55
6.11	The architecture of CSD neural network training process. . . . .	56
6.12	The ROC curve of the training model. The x-axis is the photon acceptance, and the y-axis is the neutron rejection. . . . .	56
6.13	Average pulse shape of the neutron sample (blue dots) and photon sample (red dots) from one CsI crystal.[24] . . . . .	57
6.14	Distribution of the likelihood ratio for hadronic cluster events (red) and photon cluster events (blue). The photon cluster events are obtained through the $K_L^0 \rightarrow 3\pi^0$ decay analysis of data. The neutron sample is obtained from neutron data. . . . .	57
6.15	Illustration of shower depth means. An MPPC is installed on the upstream side. The time difference between the photon arriving upstream and downstream ( $\Delta T = T_{MPPC} - T_{PMT}$ ) is used to measure the depth of the reaction and distinguish between photon events (up) and neutron events (down). . . . .	58
6.16	Distribution of the $\Delta T$ for neutron events and photon events. The photon cluster events are obtained through the $K_L^0 \rightarrow 3\pi^0$ decay analysis of data. The neutron sample is obtained by scattering neutrons in the beam with an Al plate. . . . .	59
6.17	The $R_{XY}$ distribution of the region 2. The red line and arrow indicated the cutoff region . . . . .	60

6.18 $E_\gamma$ - $H_{XY}$ distribution of physics data after applying all the selection cuts. The black box is the blind region the red frame is the signal region. The black (red) number is the observed (expected) number of events. . . . .	62
6.19 $E_\gamma$ - $H_{XY}$ distribution of physics data after open the blind box. The black (red) number is the observed (expected) number of events. . . . .	62
7.1 Upper limit (left) and signal acceptance (right) for each mass dark photon from 0 MeV to 250 MeV . . . . .	64

# List of Tables

1.1	Theoretical predictions for the branching fractions of the Kaon decays involving massless dark photons. [3] . . . . .	2
1.2	Main $K_L^0$ decay background modes and their branching ratios. . . . .	3
5.1	Branching ratio of $K_L$ decays . . . . .	31
5.2	Summary of the veto cut . . . . .	37
6.1	Main $K_L^0$ decay background modes and their branching ratios. . . . .	45
6.2	Summary of Systematic Uncertainty for SES . . . . .	59
6.3	Number of events predicted for each source inside the signal region . . . . .	61



# <sup>1</sup> Chapter 1

## <sup>2</sup> Introduction

### <sup>3</sup> 1.1 Dark Matter and Dark Photons

<sup>4</sup> Dark matter (DM) is posited to constitute approximately 26.4% of the universe's critical  
<sup>5</sup> density, according to cosmological observations [1]. At this moment the fundamental na-  
<sup>6</sup> ture of dark matter remains one of the most profound mysteries in physics. The Standard  
<sup>7</sup> Model (SM) of particle physics provides no viable explanation for dark matter, prompt-  
<sup>8</sup> ing the motivation to explore physics beyond the Standard Model (BSM). Recent years  
<sup>9</sup> have seen a surge in research aimed at probing the dark sector, with numerous astrophys-  
<sup>10</sup> ical and high-energy physics (HEP) experiments making intensified efforts to explore the  
<sup>11</sup> dark matter.

<sup>12</sup> The dark photon is one of the most promising candidates in the dark sector, it is a new  
<sup>13</sup> type of gauge boson. Theatrical there are two kinds of dark photons, the massive dark  
<sup>14</sup> photon and the massless dark photon. The massive dark photon ( $A'$ )could mix coupling  
<sup>15</sup> with visible photons, to interact with the ordinary particles [1], which means the massive  
<sup>16</sup> dark photon is possible to be detected in the experiments. Consequently, the massive  
<sup>17</sup> dark photon gets most of the attention in the experimental search for dark photons [2].  
<sup>18</sup> However, the massive dark photon has been searched by several experiments, and no  
<sup>19</sup> evidence has been observed so far, the parameter space for the massive dark photon  
<sup>20</sup> has been increasingly constrained. Therefore, our investigation shifts focus towards the  
<sup>21</sup> search for the massless dark photon.

<sup>22</sup> The massless dark photon, denoted as  $\bar{\gamma}$  in this thesis, is different from the massive  
<sup>23</sup> dark photon, it will not directly couple with the Standard Model(SM) particles, and only  
<sup>24</sup> interact with the SM particles by coupling to the quark. [2] Therefore the massless dark  
<sup>25</sup> photon is more challenging to be searched in the experiments because it is undetectable.

### <sup>26</sup> 1.2 Theoretical Predictions

<sup>27</sup> There are some theoretical calculations predict that the existence of massless dark pho-  
<sup>28</sup> tons in the Kaon decay [3]. Assuming the flavor-changing neutral current (FCNC) cou-  
<sup>29</sup> pling to the  $d$  and  $s$  quarks, the Kaon meson can decay with missing energy by a massless  
<sup>30</sup> dark photon. The theories consider the neutral Kaon decay and the charge Kaon channels  
<sup>31</sup> shown in the below Table 1.1.

TABLE 1.1: Theoretical predictions for the branching fractions of the Kaon decays involving massless dark photons. [3]

Decay Channel	Branching Fraction
$K_L \rightarrow \gamma\bar{\gamma}$	$< 1.2 \times 10^{-3}$
$K_S \rightarrow \gamma\bar{\gamma}$	$< 2.1 \times 10^{-6}$
$K_L \rightarrow \pi^0\gamma\bar{\gamma}$	$< 1.0 \times 10^{-6}$
$K_S \rightarrow \pi^0\gamma\bar{\gamma}$	$< 1.8 \times 10^{-9}$
$K_L \rightarrow \pi^+\pi^-\bar{\gamma}$	$< 9.8 \times 10^{-6}$
$K_S \rightarrow \pi^+\pi^-\bar{\gamma}$	$< 1.7 \times 10^{-8}$
$K^+ \rightarrow \pi^+\gamma\bar{\gamma}$	$< 5.6 \times 10^{-7}$
$K^+ \rightarrow \pi^+\pi^0\bar{\gamma}$	$< 2.4 \times 10^{-6}$

32 Some decay channels decay by  $KLz$  is potentially searched in the KOTO experiment.  
 33 KOTO Experiment is a rare kaon decay experiment, it is designed to search for the  $K_L^0 \rightarrow$   
 34  $\pi^0\nu\bar{\nu}$  decay, which is a rare long-lifetime decay that can provide valuable insights into  
 35 the CP violation in the Standard Model.  $K_L^0 \rightarrow \pi^0\nu\bar{\nu}$  decay has neutrinos in the final  
 36 state, it will perform as the missing energy in the detector because it is undetectable.  
 37 To probe the missing energy of the neutrino pair, a hermetic veto system was designed  
 38 to enclose the kaon decay volume. This design can avoid the energy missing from the  
 39 detectable particle as much as possible, which is beneficial to the search for the missing  
 40 energy model.

### 41 1.3 Basic Strategy of the $K_L^0 \rightarrow \gamma\bar{\gamma}$ Search

42 From the theoretical perspective shown above, the massless dark photon can be produced  
 43 in the  $K_L^0 \rightarrow \gamma\bar{\gamma}$  decay with the branching fraction of this model up to  $10^{-3}$ . This is well  
 44 within the sensitivity of the KOTO experiment and is the search Objective of this thesis.

45 In the  $K_L^0 \rightarrow \gamma\bar{\gamma}$  decay, the final state is a photon and a massless dark photon, the  
 46 photon is detectable in the detector, and the massless dark photon is undetectable.

#### 47 1.3.1 Signal Identification

48  $K_L^0 \rightarrow \gamma\bar{\gamma}$  decay requires only one photon cluster to hit the CsI calorimeter and without  
 49 any in-time hit in the rest of the detector. A single cluster can only provide the energy  
 50 and position information. The lack of kinematic constraints will be the challenge of this  
 51 study. Moreover, single cluster signatures are easily mimicked by some unknown arbi-  
 52 trary background. Requiring a high photon energy may help to suppress this kind of  
 53 background but also reduce the signal efficiency.

#### 54 1.3.2 Major Background Sources

55 The major background sources are  $K_L^0$  decay background and neutron-like background.

<sup>56</sup>  **$K_L^0$  decay background**

<sup>57</sup> Table 6.1 shows the main  $K_L^0$  decay backgrounds. Other decay channels are unnecessary to be considered because of the low branching ratio. Only  $K_L^0 \rightarrow \pi^\pm e^\mp \nu_e$  and  $K_L^0 \rightarrow \pi^\pm \mu^\mp \nu_\mu$  are considered for the decay channel of charged particles in the final state, due to the high branching ratio. To suppress the  $K_L^0$  decay background, studying these decay channels and understanding their characteristics are important. All of these decay channels produce more than one photon in the final state. Therefore, it is easy to suppress these decay channels with the KOTO detector. Except for the decay of  $K_L^0 \rightarrow 2\gamma$ , whose final state is similar to the signal signature and may be a potentially non-eliminable source of background.

TABLE 1.2: Main  $K_L^0$  decay background modes and their branching ratios.

Decay mode	Branching Ratio
$K_L \rightarrow \pi^\pm e^\mp \nu_e$	$(40.55 \pm 0.11)\%$
$K_L \rightarrow \pi^\pm \mu^\mp \nu_\mu$	$(27.04 \pm 0.07)\%$
$K_L \rightarrow 3\pi^0$	$(19.52 \pm 0.12)\%$
$K_L \rightarrow \pi^+ \pi^- \pi^0$	$(12.54 \pm 0.05)\%$
$K_L \rightarrow 2\pi^0$	$(8.64 \pm 0.06) \times 10^{-4}$
$K_L \rightarrow 2\gamma$	$(5.47 \pm 0.04) \times 10^{-4}$

<sup>66</sup> **Neutron-like background**

<sup>67</sup> The neutron originating from the beamline poses a significant background challenge. Accurately simulating the in-beam neutron background is nearly impossible, especially without a defined mechanism to avoid it. The primary method to mitigate this background involves distinguishing the cluster from the photon event.

<sup>71</sup> **1.4 Thesis Overview**

<sup>72</sup> This thesis presents a detailed study of the  $K_L^0 \rightarrow \gamma\bar{\gamma}$  decay in the KOTO experiment. We begin with an overview of the KOTO experiment, describing its detector components and data acquisition (DAQ) system. The analysis section follows, where we elucidate the event reconstruction methods and Monte Carlo simulation techniques employed in the KOTO experiment. Special attention is given to the unique approaches developed for this particular analysis. Subsequently, we delve into the crucial process of Kaon yield estimation and provide an in-depth exploration of the  $K_L^0 \rightarrow \gamma\bar{\gamma}$  analysis. This includes background estimation and systematic uncertainty evaluation. In conclusion, we summarize our findings and discuss their implications. The thesis culminates with an outlook on the prospects of the  $K_L^0 \rightarrow \gamma\bar{\gamma}$  search within the KOTO experiment, considering potential improvements and challenges.



<sup>83</sup> **Chapter 2**

<sup>84</sup> **KOTO Experiment**

<sup>85</sup> The KOTO Experiment is a rare decay experiment. The main goal of this experiment is  
<sup>86</sup> to search for the  $K_L \rightarrow \pi^0 \nu \bar{\nu}$  decay. The branching ratio of this decay is predicted to be  
<sup>87</sup>  $(3.00 \pm 0.30) \times 10^{-11}$  by the Standard Model (SM) [4]. The branching ratio of this decay  
<sup>88</sup> is sensitive to the new physics beyond the SM because of the accuracy. Therefore, the  
<sup>89</sup> KOTO experiment is a good place to search for new physics.

<sup>90</sup> This chapter will introduce the KOTO detector, outlining the sequence from proton  
<sup>91</sup> generation through to data capture within the detector.

<sup>92</sup> **2.1 J-PARC and Proton Beamlne**

<sup>93</sup> The KOTO experiment is located at the Japan Proton Accelerator Research Complex (J-  
<sup>94</sup> PARC)[5] Hadron Experimental Facility (HEF) in Tokai, Japan. Figure 2.1 shows the flow  
<sup>95</sup> of proton beam acceleration, HEF (Hadron Beam Facility) is one of the delivered exper-  
<sup>96</sup> iment facilities. The proton beam has been generated at the end of the linear particle  
<sup>97</sup> accelerator (LINAC)[6], then into a 3 GeV rapid cycling synchrotron (RCS)[7], and finally  
<sup>98</sup> into the main ring synchrotron (MR) to accelerate to 30 GeV[8]. At the end extracted from  
<sup>99</sup> the synchrotron and directed to the HEF, as shown in Figure 2.2.

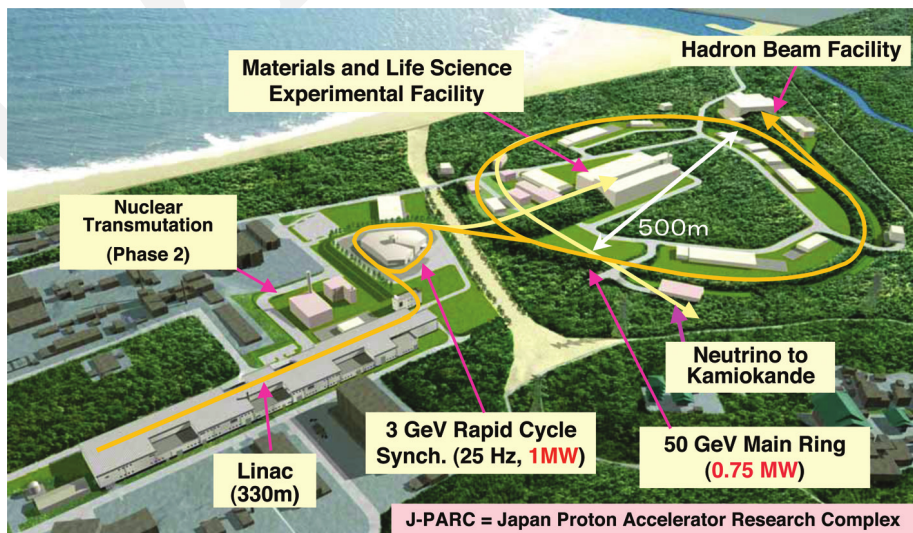


FIGURE 2.1: The entire view of J-PARC. [5]

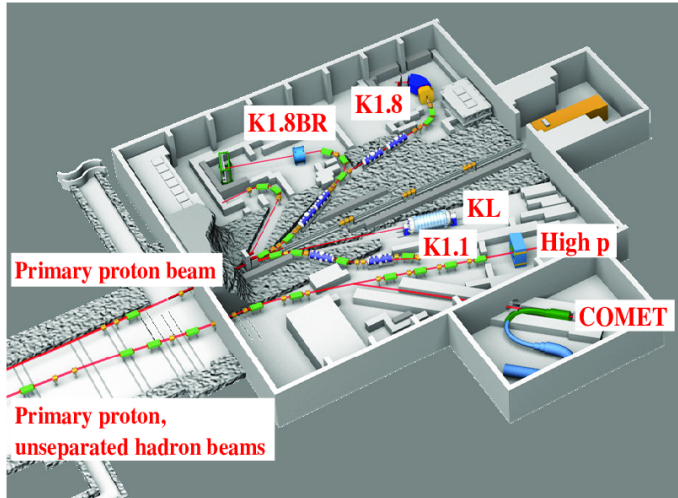


FIGURE 2.2: Illustration of the Hadron Experimental Facility (HEF) at J-PARC.[9] The KL in the Figure indicated the KOTO detector

To reduce the instantaneous rate of particles coming into detectors to prevent the event pileup, a slow-extraction (SX) technique is used. The proton beam was extracted for 2 seconds as a "spill" every 4.22 seconds in 2024 for the beam power of 82 kW. The beam power is calculated by

$$\text{Beam Power} = E_{\text{proton}} F_{\text{proton}}, \quad (2.1)$$

$$F_{\text{proton}} = N_{\text{spill}}^{\text{proton}} / s_{\text{spill}} \quad (2.2)$$

where  $E_{\text{proton}}$  is the extracted energy of the proton beam,  $F_{\text{proton}}$  is the protons flux,  $N_{\text{spill}}^{\text{proton}}$  is the number of protons per spill, and  $s_{\text{spill}}$  is the spill duration.

In HEF, the extracted proton beam collides with the T1 target to produce secondary particles. As shown in Figure 2.3, the T1 target consists of two 66 mm long gold bars with dimensions of  $15 \times 11$  mm in cross-section. One bar is used for production and the other one is a spare. The secondary particles are then directed to the KOTO detector at a  $16^\circ$  to the beamline.

## 2.2 $K_L^0$ Beamline

After the p-gold collides, a  $16^\circ$  to the beamline was chosen to direct the Kaon beamline for KOTO. Figure 2.4 shows the schematic diagram of the  $K_L^0$  beamline. To reduce the photon in the beamline, a 7 cm thick lead photon absorber was installed after the T1 target. Two collimators follow that to narrow the beamline and make it pencil-like. A sweeping magnet with a 1.2 T magnetic field was installed between the two collimators to reduce the charged particles in the beamline. A rotatable beam plug is placed between the sweeping magnet and the 2nd collimator, it is made of brass that could stop the beamline with most particles. The total length of the beamline is 20 m, which is long enough to allow the short-life particles, such as the  $K_s$  and hyperons, to decay before reaching the KOTO detector. Figure 4.1 shows the possible remaining particle at the end of the 2nd

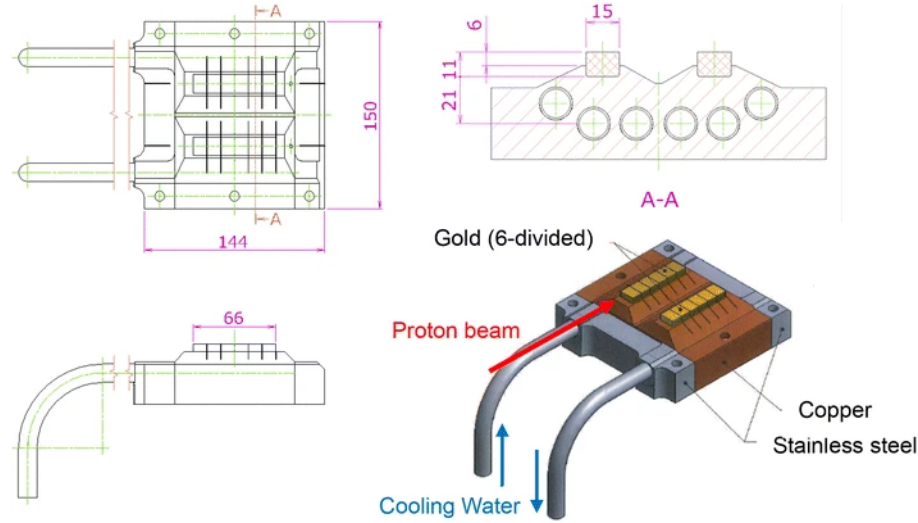


FIGURE 2.3: Structural drawings of the T1 production target [10]. One bar is used for production and the other is a spare.

122 collimator in the beamline which is estimated by the beamline simulation. These particles  
123 will enter the KOTO detector.

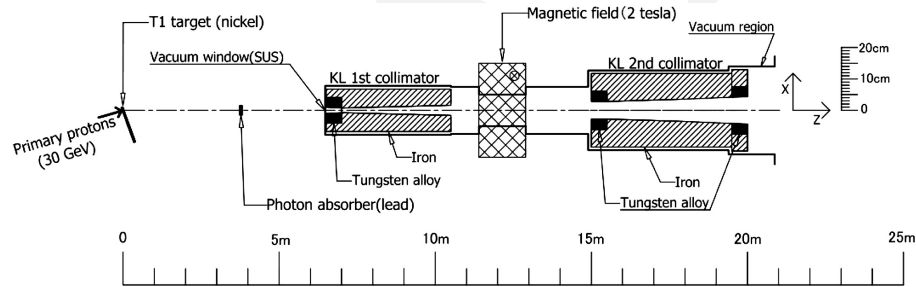


FIGURE 2.4: Schematic diagram of the  $K_L^0$  beamline.[11]

## 124 2.3 Detectors

125 The KOTO detector is designed to study the decay of  $K_L^0$  particles. Its main components  
126 are an electromagnetic calorimeter and a hermetic veto system. As  $K_L^0$  particles enter the  
127 detector, they decay within a highly evacuated volume maintained at  $5 \times 10^{-5}$  Pa. The  
128 resulting decay products are then detected by various subdetectors. The electromagnetic  
129 calorimeter, positioned perpendicular to the beamline, serves primarily as a photon de-  
130 tector. Surrounding the decay volume, the hermetic veto system comprises multiple veto  
131 counters, including barrel vetoes, charge vetoes, and additional specialized veto coun-  
132 ters. This comprehensive veto system ensures efficient detection and differentiation of  
133 particle interactions. Figure 2.7 provides a schematic overview of the KOTO detector's  
134 layout and components. In this section, the Calorimeter and some important veto coun-  
135 ters will be introduced in detail.

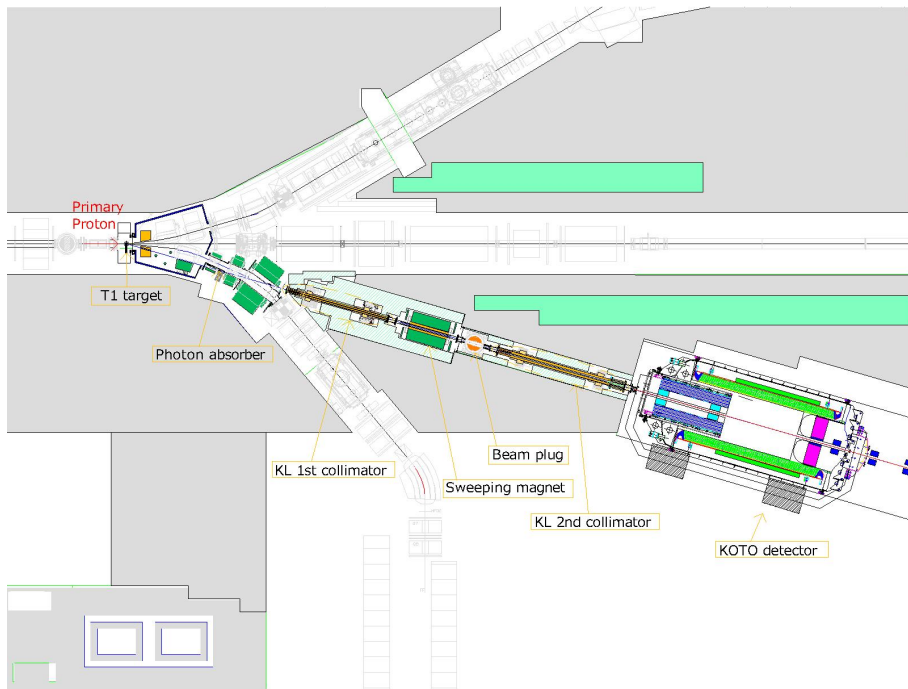


FIGURE 2.5: Beamlne layout

### <sup>136</sup> 2.3.1 CsI

<sup>137</sup> The electromagnetic calorimeter is the main detector of the KOTO experiment. It is used  
<sup>138</sup> to detect the photon from the  $K_L$  decay. The electromagnetic calorimeter consists of 2716  
<sup>139</sup> undoped cesium iodide crystals (CsI). The cross-section of crystals has 2 types of units:  
<sup>140</sup> the small crystal is  $25 \times 25$  mm with 2240 crystals, and the large one is  $50 \times 50$  mm with  
<sup>141</sup> 476 crystals. The arrangement of those crystals is shown in Figure 2.6. The depth of the  
<sup>142</sup> crystal is 500 mm corresponding to 27 radiation lengths( $X_0$ ), in which the  $X^0$  of CsI is  
<sup>143</sup> 18.5 mm. The large crystal depth can contain all the photon energy that can allow us to  
<sup>144</sup> ignore the detection inefficiency of the photon. The small crystal size is smaller than the  
<sup>145</sup> Molère radius of 35.7 mm, which provides a good resolution of position and the cluster  
<sup>146</sup> shape in the x-y plant. That allows us to use the shower shape to distinguish the different  
<sup>147</sup> types of clusters on CsI.

<sup>148</sup> A both-end readout system was used in the CsI calorimeter. A photon multiplier tube  
<sup>149</sup> (PMT) was connected to the end of each CsI crystal. When a photon hits the CsI, the EM  
<sup>150</sup> shower will be induced and the PMT can observe the deposited energy on each crystal.  
<sup>151</sup> In front of the CsI crystal, 4096 Multi-pixel photon counters (MPPC) were glued. It could  
<sup>152</sup> detect the signal of the photon hit from the front end. This readout system can be used to  
<sup>153</sup> measure the shower depth in the calorimeter, by evaluating the time difference between  
<sup>154</sup> both ends of the crystal. Which is potentially useful for discriminating the photon cluster  
<sup>155</sup> and hadronic-like cluster. Because a hadronic shower is generally deeper than an EM  
<sup>156</sup> shower cluster.

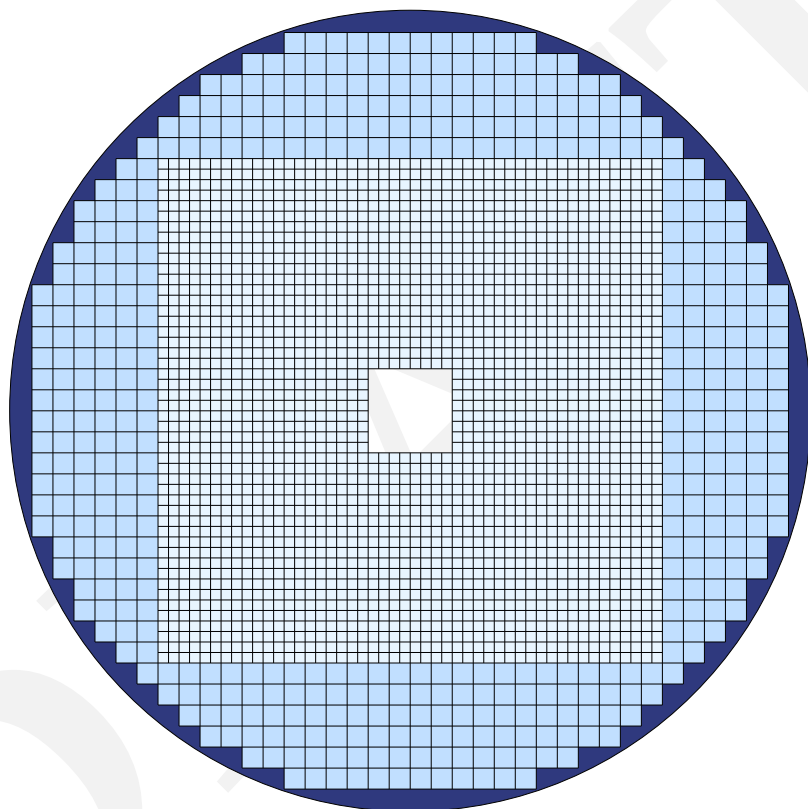


FIGURE 2.6: Schematic diagram of CsI layout.

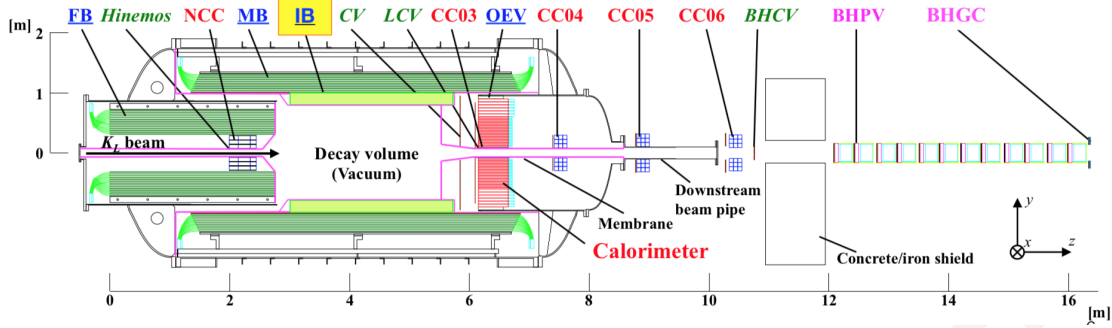


FIGURE 2.7: KOTO detector layout

### 157 2.3.2 Charge Veto Counter

158 The Charge Veto Counter (CV) is placed in front of the CsI [12, 13, 14]. It is a plant com-  
 159 posed of plastic scintillator strips, the arrangement of the strips is shown in Figure 2.8.  
 160 Because the CV plant is also perpendicular to the beamline, a square hole was made in  
 161 the center of the CV to allow the beamline to pass through. The CV consists of two layers  
 162 of 3-mm thick scintillator strips and wavelength-shifting (WLS) fibers, the direction of  
 163 the two layers' strips is perpendicular to each other. The front CV is placed 30 cm up-  
 164 stream of the CsI, and the Rare CV is placed 5 cm upstream. An MPPC was attached to  
 165 both ends of the strip to detect the light emitted by the scintillator.

166 This veto counter was used to detect the charged particle that could hit the CsI calorime-  
 167 ter. Because the  $K_L^0 \rightarrow \pi^\pm e^\mp \nu_e$  and  $K_L^0 \rightarrow \pi^\pm \mu^\mp \nu_\mu$  have a very large branching ratio, the  
 168 charged particle could hit the CsI calorimeter and produce a fake photon cluster. The  
 169 main purpose of the CV is to veto the charged particle and reduce these two decay chan-  
 170 nels. The inefficiency of the CV to a single charge particle is  $1.5 \times 10^{-5}$ .

### 171 2.3.3 Barrel Veto Counter

172 The Barrel veto counters surround the decay volume which is the main body of the her-  
 173 metic veto system to ensure all the photons will not escape from the detector. There are  
 174 3 Barrel Veto Counters in the KOTO detector, Front Barrel(FB), Main Barrel(MB), and In-  
 175 ner Barrel(IB). The place relation of the three barrel veto counters was shown in Figure  
 176 2.9. The MB covered the decay volume, and the IB was placed in the center of the MB,  
 177 these two veto counters are used to detect the photon hit escape from the CsI calorime-  
 178 ter. The front barrel covers the upstream of the decay region to veto the event decay in  
 179 the upstream region. All the barrel veto counters are composed of the lead-scintillator  
 180 sandwich structure, as shown in Figure 2.9. The lead was used to absorb the photon and  
 181 the scintillator was used to emit the light when the photon hit. After the light emitted by  
 182 the scintillator, it will be transferred to the PMT attached to the end of the barrel by WSL  
 183 fiber. At the innermost of the MB and IB, a 10 mm thick Charge Veto is attached, which is  
 184 called MBCV and IBCV. The MBCV and IBCV consisted of the scintillator and WLS fiber,  
 185 which was used to veto the charged particle.

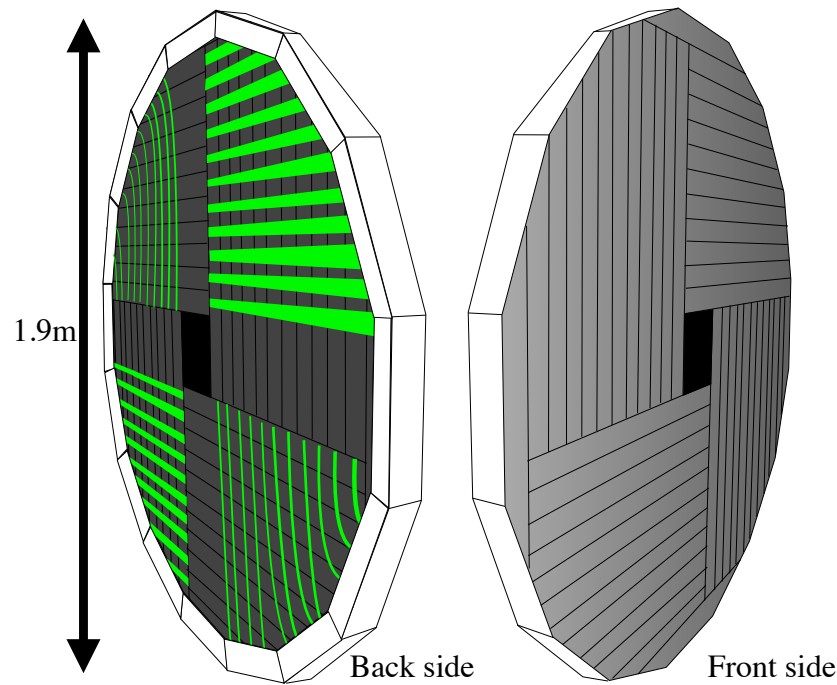


FIGURE 2.8: The Schematic Diagram of Charge Veto Structure.

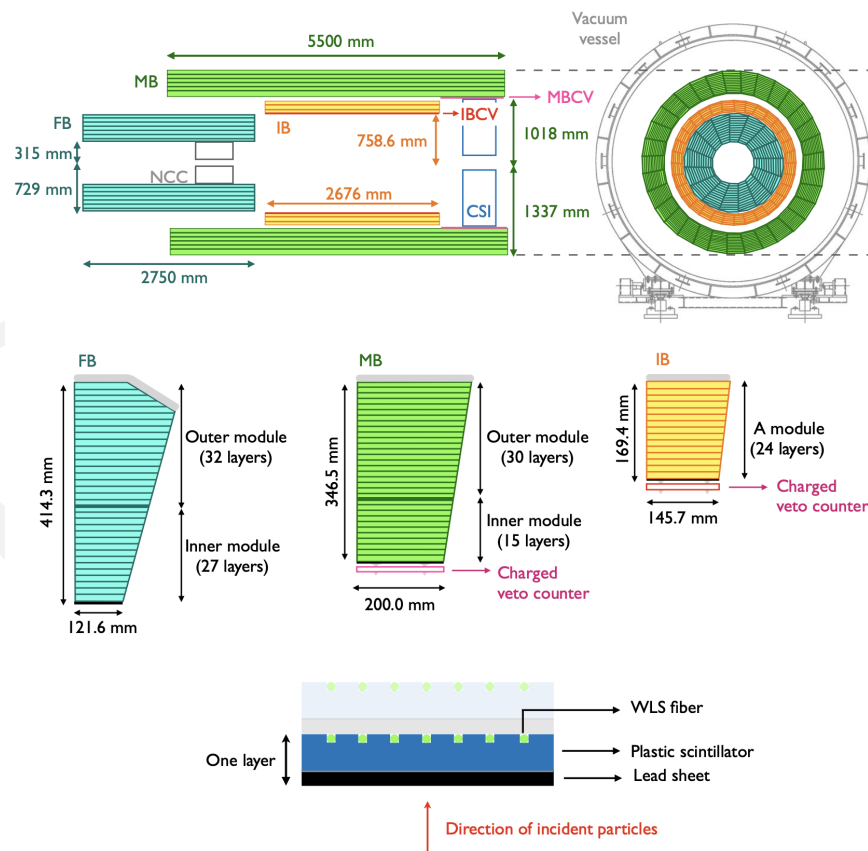


FIGURE 2.9: The Schematic Diagram of Barrel Veto Structure. Figure courtesy of [15].

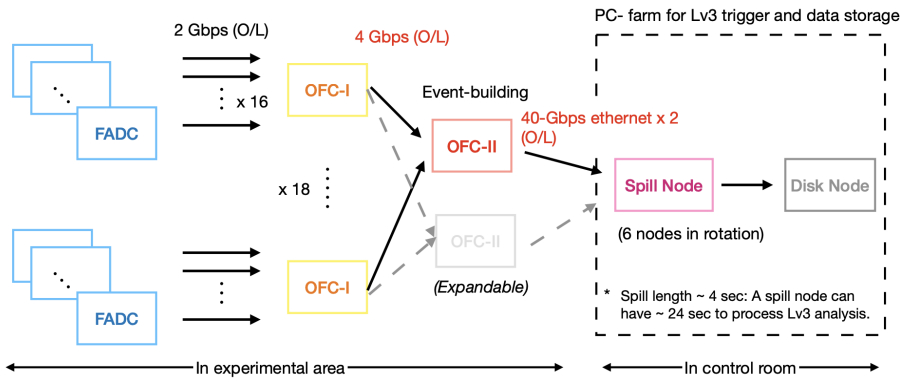


FIGURE 2.10: The architecture of the KOTO DAQ system. [16]

## <sup>186</sup> 2.4 Data Acquisition System

<sup>187</sup> When a particle hits the detectors, the electronic signal will be generated. To determine  
<sup>188</sup> whether this signal is interesting, a trigger system is used to decide the candidate events.  
<sup>189</sup> If an event passes any trigger criteria, the data acquisition system (DAQ) will collect and  
<sup>190</sup> store the data.

<sup>191</sup> The DAQ system of the KOTO experiment consists of 3 levels: the first-level (L1) and  
<sup>192</sup> second-level (L2) trigger placed in the experiment area, and the third-level trigger (L3) at  
<sup>193</sup> the PC farm. The architecture of the DAQ system is shown in Figure 2.10.

<sup>194</sup> KOTO detector has nearly 4000 channels in total, all these channels are connected to  
<sup>195</sup> the flash analog-to-digital converter (FADC) board to digitize the signal. There are two  
<sup>196</sup> types of FADC boards in the KOTO detector, with 125 MHz and 500 MHz sampling rates.  
<sup>197</sup> We have a total of 288 FADC boards and separate them into 18 crates with 16 boards in  
<sup>198</sup> each crate.

<sup>199</sup> For the 125 MHz FADC, 16 channels are connected to each board, and the 500 MHz  
<sup>200</sup> FADC has 4 channels on each board.

201 **Chapter 3**

202 **Event Reconstruction**

203 Event reconstruction is a crucial step in the analysis of decay events. After the reconstruction,  
204 the kinematic variable of the  $K_L^0$ , such as the decay vertex, energy, and momentum,  
205 can be obtained. With kinematic information, precise event selection can be achieved and  
206 the performance of physical analysis can be improved.

207 To reconstruct a  $K_L^0$  decay event, it is necessary to accurately model the decay process.  
208 The primary strategy involves initially identifying photon clusters. Subsequently, the  
209 clusters' energy, timing, and position on the CsI are utilized to reconstruct the parent  
210 particle. This includes determining kinematic properties such as the decay vertex, energy,  
211 and momentum of the parent particle. The specific details of the reconstruction process  
212 vary depending on the decay mode. For channels involving pions, such as  $K_L^0 \rightarrow 3\pi^0$  and  
213  $K_L^0 \rightarrow \pi^0\pi^0$ , the photon clusters are mapped to pions, which are then used to reconstruct  
214 the Kaon. In simpler decay channels like  $K_L^0 \rightarrow 2\gamma$ , the  $K_L^0$  is directly reconstructed from  
215 the photon data.

216 **3.1 Photon Cluster Finding**

217 In this step, we need to find the photon cluster and then reconstruct the energy, timing,  
218 and the hit position of the cluster. This process is called "clustering".

219 First, need to find the cluster. The crystal which has deposited energy larger than 3  
220 MeV and the hit timing is within 150 ns is considered a "seed crystal". Then, scanning  
221 the neighboring crystals in a 140 mm wide square box around the seed crystal. The  
222 neighboring crystals will add to the same cluster if the neighboring crystal is also a seed  
223 crystal. And do the same scanning process for the neighboring crystals of the neighboring  
224 crystals, til there is not a neighboring friend that can be found. This process will be  
225 applied to all the seed crystals that have not been assigned to any cluster yet. A seed  
226 crystal without any neighboring friend will be defined as an "isolated crystal hit". The  
227 isolated crystal hit will be used in the CsI veto. The algorithm is illustrated in Figure 3.1.

228 Because of the wide 150 ns timing window, the cluster may contain the hits not belong  
229 to the cluster shower. A seed crystal is assigned to a cluster, but it does not come from  
230 the cluster shower will be defined as an "accidental hit" and should be removed from the

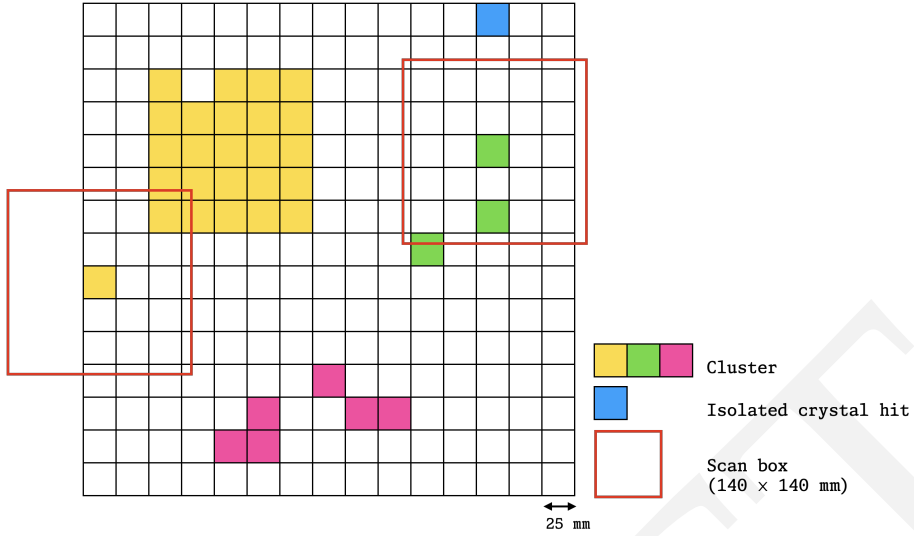


FIGURE 3.1: The illustration of the cluster finding process. All the color crystals are the seed crystals, and the crystals with the same color belong to the same cluster. The black crystal is the isolated crystal hit.

<sup>231</sup> cluster. To avoid the accidental hit, the cluster timing was used to do the selection. The  
<sup>232</sup> cluster timing ( $T_{cluster}$ ) is defined by the equation 3.1.

$$T_{cluster} = \frac{\sum_{n=1}^{i=1} T_i / \sigma_t^2}{\sum_{n=1}^{i=1} 1 / \sigma_t^2} \quad (3.1)$$

$$\sigma_t = 0.13 \oplus \frac{3.63}{\sqrt{E_i}} \oplus \frac{5}{E_i} \quad (3.2)$$

<sup>233</sup> Where  $n$  is the number of crystals in the cluster,  $i$  is the  $i$ -th crystal, and  $e$  is the energy  
<sup>234</sup> of the cluster. The  $\sigma_t$  is the timing uncertainty of each crystal, which is a function of  
<sup>235</sup> the energy of each crystal[17]. If a seed crystal from a cluster with timing outside the  
<sup>236</sup>  $\pm 5\sigma$  boundary of its cluster timing, it will be defined as an accidental hit and will be  
<sup>237</sup> removed. Figure 3.2 shows the timing boundary for a crystal seed after subtracting the  
<sup>238</sup> cluster timing. The cluster timing will recalculate after removing the accidental hit and  
<sup>239</sup> iterate this process until all accidental hits have been removed.

<sup>240</sup> Moreover, a timing selection will apply to the clusters. Because the cluster should be  
<sup>241</sup> produced by the same Kaon decay, the timing of the cluster should be within a certain  
<sup>242</sup> range. Therefore, the maximum timing difference between all clusters should be within  
<sup>243</sup> 30 ns. Otherwise, the cluster that has the largest timing difference with the average timing  
<sup>244</sup> of all clusters will be removed. This process will be repeated until all clusters satisfy the  
<sup>245</sup> timing selection.

<sup>246</sup> The cluster after the above process will be used in the next step of the reconstruction.  
<sup>247</sup> The below information on the cluster will be calculated and provided to the next step.

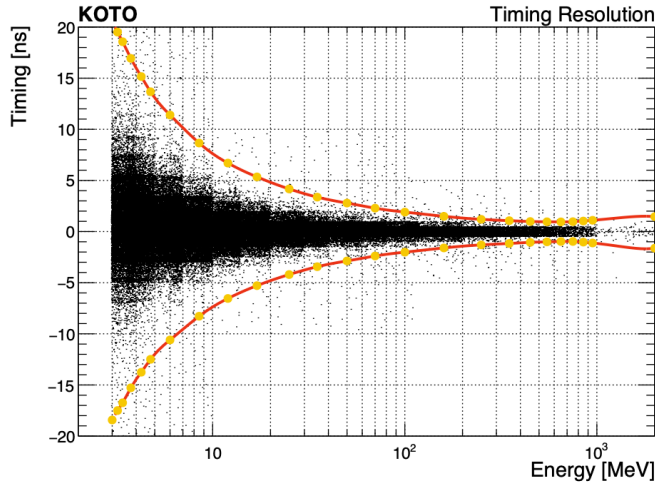


FIGURE 3.2: Timing boundary for a cluster seed based on the scattered plot of crystal timing versus energy deposit. A Gaussian function is fitted at each energy bin and the boundary is defined by  $\mu \pm 5\sigma$ , where  $\mu$  and  $\sigma$  are the Gaussian mean and standard deviation. The orange points indicate the boundary at the associated energy bin. The red curve connects all the points for the interpolation of the boundary value between the points. (Figure courtesy of [15])

248      **Cluster Energy ( $E_{cluster}$ )**

249      The energy of the cluster is the sum of the energy of all crystals in the cluster.

$$E_{cluster} = \sum_{i=1}^n E_i \quad (3.3)$$

250      **Cluster Position ( $x_{cluster}, y_{cluster}$ )**

251      The position of the cluster is defined by its center of energy, and the position is  
252      calculated by the equation below.

$$x_{cluster} = \frac{\sum_{i=1}^n E_i x_i}{E_{cluster}} \quad (3.4)$$

$$y_{cluster} = \frac{\sum_{i=1}^n E_i y_i}{E_{cluster}} \quad (3.5)$$

253      **3.2 Reconstruction of  $\pi^0$**

254      The  $\pi^0$  is reconstructed by two photon clusters. Figure 3.3 shows the schematic diagram  
255      of the  $\pi^0 \rightarrow 2\gamma$  decay process. First, the decay vertex needs to be determined, assum-  
256      ing the decay vertex is  $(0, 0, z_{vtx})$ . Therefore, the three momenta of the photon can be  
257      calculated by

$$\vec{P}_\gamma = k \cdot (x, y, \Delta z) \quad (3.6)$$

258      where the  $k$  is a constant does not determine yet. And the  $\Delta z$  is the difference between  
259      the z position of the cluster and the decay vertex.

$$\Delta z = z_{CsI} - z_{vtx} \quad (3.7)$$

260      Based on four-momentum conservation, the opening angle ( $\theta$ ) between two photons is  
261      calculated by

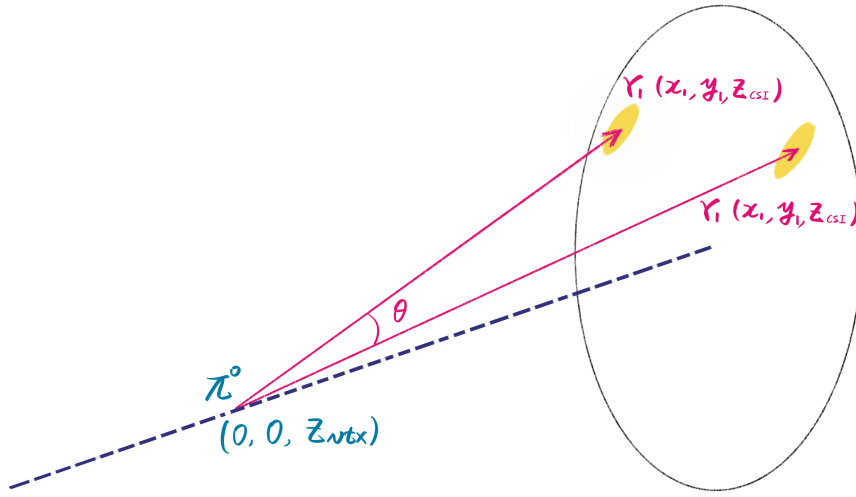


FIGURE 3.3: The schematic diagram of the  $\pi^0 \rightarrow 2\gamma$  decay process.

$$\cos(\theta) = 1 - \frac{M_{\pi^0}^2}{2 \cdot E_{\gamma 1} \cdot E_{\gamma 2}} \quad (3.8)$$

and combine with the inner product of two photons' momentum, the following equation can derive the  $z_{vtx}$ .

$$1 - \frac{M_{\pi^0}^2}{2 \cdot E_{\gamma 1} \cdot E_{\gamma 2}} = \frac{\vec{P}_{\gamma 1} \cdot \vec{P}_{\gamma 2}}{|\vec{P}_{\gamma 1}| \cdot |\vec{P}_{\gamma 2}|} \quad (3.9)$$

After determining the  $z_{vtx}$ , the momentum of the photon can be calculated by

$$|\vec{P}_\gamma| = E_\gamma \quad (3.10)$$

The energy and momentum of the  $\pi^0$  can be calculated by

$$E_{\pi^0} = E_{\gamma 1} + E_{\gamma 2} \quad (3.11)$$

$$\vec{P}_{\pi^0} = \vec{P}_{\gamma 1} + \vec{P}_{\gamma 2} \quad (3.12)$$

### 3.3 Reconstruction of Decays

In this section, the reconstruction algorithm for the  $K_L^0 \rightarrow 3\pi^0$  and  $K_L^0 \rightarrow \gamma\bar{\gamma}$  decay will be introduced. The  $K_L^0 \rightarrow 3\pi^0$  decay is used to evaluate the  $K_L^0$  yield, and the  $K_L^0 \rightarrow \gamma\bar{\gamma}$  decay is for the physics analysis. In other KOTO experiment studies, the  $K_L^0 \rightarrow \pi^0\pi^0$  and  $K_L^0 \rightarrow 2\gamma$  decay are also used in the yield estimation and are not covered in this section. Because the  $K_L^0 \rightarrow 3\pi^0$  is the only decay channel used for the yield estimation.

All the  $K_L^0$  decay reconstruction is based on the result from the clustering process. A minimal energy selection of 20 MeV is required for the photon cluster. Also, the number of photon cluster requirement need to be equal to the final state of the decay. For the

<sup>275</sup>  $K_L^0 \rightarrow 3\pi^0$  decay, the event needs to have exactly 6 photon clusters. For the  $K_L^0 \rightarrow \gamma\bar{\gamma}$   
<sup>276</sup> decay, the event should contain only 1 photon cluster.

<sup>277</sup> After the  $K_L^0$  decay vertex reconstruction, then calculate the kinematic variables. The  
<sup>278</sup> kinematic variable will be utilized in the next step analysis.

<sup>279</sup> **3.3.1 Reconstruction of  $K_L^0 \rightarrow 3\pi^0$**

<sup>280</sup>  $K_L^0 \rightarrow 3\pi^0$  decay has three  $\pi^0$  in the decay process, the reconstruction of  $\pi^0$  will use  
<sup>281</sup> the same algorithm as the previous section. The special situation is there are six photon  
<sup>282</sup> clusters on the CsI, and the  $\pi^0$  can be reconstructed in different combinations. All the  
<sup>283</sup> combinations will be considered because the true combination is unknown. The most  
<sup>284</sup> number of combinations for  $K_L^0 \rightarrow 3\pi^0$  is

$$\binom{6}{2} \binom{4}{2} \binom{2}{2} / 3! = 15$$

<sup>285</sup> Because of the short lift time of the  $\pi^0$ , the decay vertex of the  $\pi^0$ 's should be very close.  
<sup>286</sup> Therefore, the  $\chi_z^2$  could be used to select the best combination.

$$\chi_z^2 = \sum_i^{N_{\pi^0}} \left( \frac{z_{vtx}^i - \bar{z}_{vtx}}{\sigma_i^2} \right)^2 \quad (3.13)$$

<sup>287</sup> where  $N_{\pi^0}$  is the number of  $\pi^0$  in the decay,  $z_{vtx}^i$  is the decay vertex z of the  $i$ -th  $\pi^0$ ,  $\bar{z}_{vtx}$   
<sup>288</sup> is the average decay vertex z of all  $\pi^0$ , and  $\sigma_i$  is the uncertainty propagated from the  
<sup>289</sup> calorimeter of the  $i$ -th  $\pi^0$ . The best combination of  $\pi^0$  should have the smallest  $\chi_z^2$ . The  
<sup>290</sup> weighted average decay vertex z is also defined as the decay vertex z of  $K_L^0$ , calculated  
<sup>291</sup> by

$$\bar{z}_{vtx} = \frac{\sum_i^{N_{\pi^0}} z_{vtx}^i / \sigma_i^2}{\sum_i^{N_{\pi^0}} 1 / \sigma_i^2} \quad (3.14)$$

<sup>292</sup> From the  $\pi^0$  reconstruction, the  $\pi^0$  decay vertex was assumed in the center of the CsI.  
<sup>293</sup> To determine the real decay vertex, a correction process was applied. As shown in Figure  
<sup>294</sup> 3.4, the  $K_L^0$  travels start from the target and end at the decay vertex, then decay to the  $\pi^0$ s  
<sup>295</sup> and  $\gamma$ s hit on the CsI, and  $K_L^0$  project to the center of energy (COE). Therefore, the  $K_L^0$   
<sup>296</sup> decay vertex can be calculated based on the geometry, by the following equation.

$$x_{vtx} = x_{COE} \cdot \frac{z_{vtx} - z_{target}}{z_{CsI} - z_{target}} \quad (3.15)$$

$$y_{vtx} = y_{COE} \cdot \frac{z_{vtx} - z_{target}}{z_{CsI} - z_{target}} \quad (3.16)$$

<sup>297</sup> where  $z_{target}$  is the z position of the target. The  $x_{COE}$  and  $y_{COE}$  can calculate by

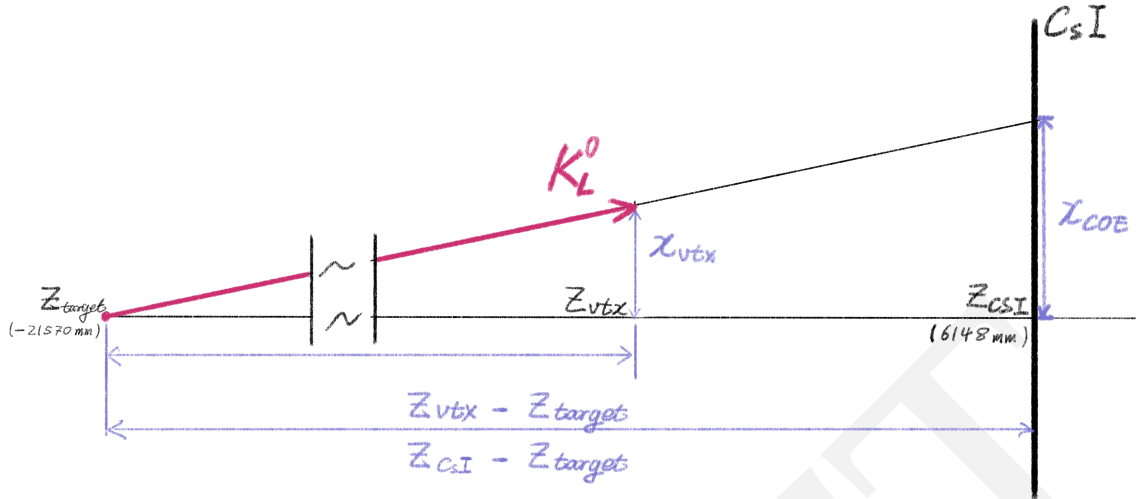


FIGURE 3.4: The schematic diagram of the  $K_L^0$  travel and decay process and geometry relationships

$$x_{COE} = \frac{\sum_{i=1}^{n_\gamma} E_i x_i}{\sum_{i=1}^{n_\gamma} E_i} \quad (3.17)$$

$$y_{COE} = \frac{\sum_{i=1}^{n_\gamma} E_i y_i}{\sum_{i=1}^{n_\gamma} E_i} \quad (3.18)$$

After obtaining the corrected decay vertex, the energy and momentum of the  $K_L^0$  can be obtained intuitively from the summation of all the  $\pi^0$ 's energy and momentum, as same as the Equation 3.11.

$$E_{K_L^0} = \sum_{i=1}^{N_{\pi^0}} E_{\pi^0} \quad (3.19)$$

$$\vec{P}_{K_L^0} = \sum_{i=1}^{N_{\pi^0}} \vec{P}_{\pi^0} \quad (3.20)$$

### 3.3.2 Reconstruction of $K_L^0 \rightarrow \gamma\bar{\gamma}$

$K_L^0 \rightarrow \gamma\bar{\gamma}$  Decay is the primary target of this analysis. The final state of  $K_L^0 \rightarrow \gamma\bar{\gamma}$  is similar to  $K_L^0 \rightarrow 2\gamma$ , but one photon is a dark photon. Due to the missing energy, the signature on CsI of  $K_L^0 \rightarrow \gamma\bar{\gamma}$  decay is only one photon cluster hit. Based on Section 3.1, the information that could be obtained from one photon cluster is only its energy, timing, and position on the CsI surface. With this limited information, it is impossible to reconstruct the  $K_L^0$  decay vertex. Therefore, the lack of kinematic information is the biggest challenge of the  $K_L^0 \rightarrow \gamma\bar{\gamma}$  decay search study.

### 3.3.3 Correction for Energy and Position of Photon Clusters

After the reconstruction of the  $K_L^0$  decay, and also obtaining the corrected decay vertex, the energy and position of the photon clusters will be possible to correct. Because this

312 correction process needs the incident angle of the photon, this process has to be done  
 313 after the  $K_L^0$  decay reconstruction. After the correction, we will use the new position to  
 314 recalculate the decay vertex.

315 **Position Correction**

316 The position of the photon cluster obtained from the clustering process is the position of  
 317 the center of energy of the cluster. As shown in the Figure 3.5. The  $z$  position for the  
 318 center of energy of the cluster is inside the crystal. However, the  $z$  position of the CsI  
 319 we used in the reconstruction is the position of the crystal surface. This difference will  
 320 introduce a bias for the reconstruction of the vertex position. To eliminate this bias, the  $x$   
 321 and  $y$  positions of the photon cluster need to be corrected to the real incident position.

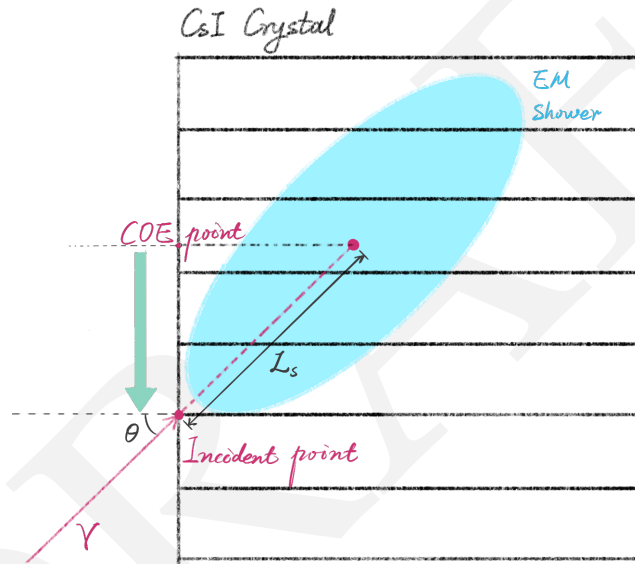


FIGURE 3.5: The schematic diagram of the correction of the photon cluster position.

322 From the decay vertex reconstruction, the incident angle ( $\theta$ ) of the photon was ob-  
 323 tained. And the corrected distance ( $L_c$ ) can be calculated by

$$L_c = L_s \cdot \sin(\theta) \quad (3.21)$$

324 where the  $L_s$  is the distance from the incident point to the cluster COE of the EM shower,  
 325 and the  $L_s$  can be calculated by

$$L_s/X_0 = p_0 + p_1 \ln(E[\text{GeV}]) \quad (3.22)$$

326 where the  $X_0 = 18.5$  is the radiation length of the CsI,  $E$  is the cluster energy in GeV, and  
 327 the  $p_0 = 6.490$  and  $p_1 = 0.993$  are the parameters obtains from the MC simulation.

328 **Energy Correction**

329 In the clustering process, a 3 MeV energy threshold was applied to the seed crystal. And  
 330 EM shower also possibly has leakage energy from the crystals and is not included in the  
 331 cluster. These factors will cause the energy lost from the measurement. To correct these  
 332 energy losses, a correction function dependence on energy was obtained from the MC  
 333 simulation.

$$E_{corr} = E \cdot (1 + w(E)) \quad (3.23)$$

334 where  $w(E)$  is the correction function.

335 After the correction of the energy and position of the photon cluster, the decay recon-  
 336 struction will be repeated. The final result will be used in the next step of the analysis.

337 **3.4 Veto Hit Reconstruction**

338 The veto counter is used in the background rejection. The rejection is based on the tim-  
 339 ing of the veto hit and the deposited energy. And that is the information we need to  
 340 reconstruct from the veto hit.

341 The reject criteria require an energy deposit over the energy threshold, which can dis-  
 342 tinguish the signal from the background noise, and a hit timing within the timing win-  
 343 dow to ensure the hit is from the same  $K_L^0$  decay event, this kind of hit is called an "on-  
 344 time" hit. Because the veto information is exclusively utilized for background rejection  
 345 criteria in this study, the hit timing was selected as the hit that was closest to the nominal  
 346 timing if there was more than one hit on the veto counter.

347 To do the timing criteria, a veto timing( $T_{veto}$ ) was defined, which is the difference  
 348 between the veto hit timing and the  $K_L^0$  decay timing. The veto timing is defined as

$$\begin{cases} T_{veto} = T_{mod} - T_{vtx} - TOF \\ TOF = D/c, \end{cases} \quad (3.24)$$

349 where the  $T_{mod}$  is the veto hit timing,  $T_{vtx}$  is the  $K_L^0$  decay timing,  $TOF$  is the time-of-  
 350 flight of the particle,  $D$  is the distance between the decay vertex and the veto hit position.  
 351 As shown in the Figure 3.6.

352 However, this equation has to involve the vertex information, which is not available  
 353 in the  $K_L^0 \rightarrow \gamma\bar{\gamma}$  analysis. Therefore, the  $T_{veto}$  needs to be modified to be independent of  
 354 the vertex information. The vertex timing  $T_{vtx}$  can be approximated by

$$T_{vtx} \approx T_{CsI} - \Delta z/c \quad (3.25)$$

355 where the  $T_{CsI}$  is the corrected average timing of the CsI clusters, and the  $\Delta z$  is the  
 356 difference between the z position of the CsI surface and the decay vertex. And with the

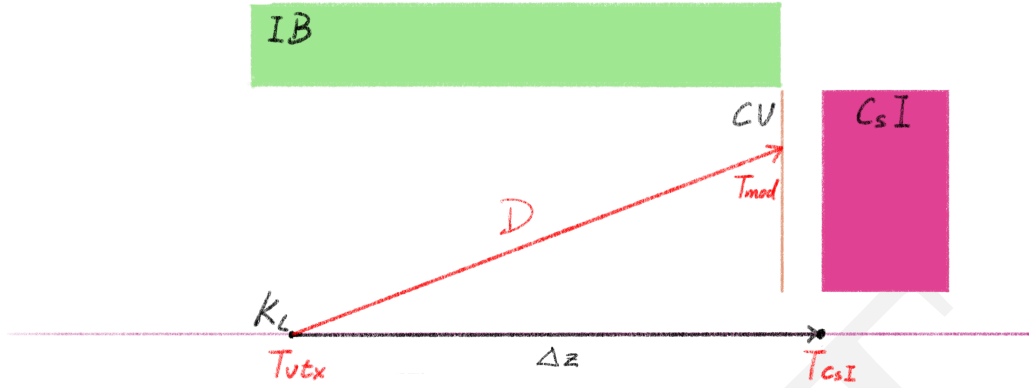


FIGURE 3.6: Schematic view of the timings used in the module-veto-timing calculation.

357 Equation 3.24 the  $T_{veto}$  can be derived as

$$T_{veto} \approx T_{mod} - T_{CsI} + (\Delta z - D)/c \quad (3.26)$$

358 The  $(\Delta z - D)$  is an uncontrolled variable because  $D$  still needs the vertex position information. Thankfully, most veto counters do not have a large scale along the z-axis, thus 359 the variant of the  $(\Delta z - D)$  is small. Therefore,  $(\Delta z - D)$  can be treated as a constant in 360 most cases, and the  $T_{veto}$  can be equivalent to 361

$$T_{veto} \equiv T_{mod} - T_{CsI} \quad (3.27)$$

362 This definition can be used in the all downstream veto count and also the FBAR and the 363 NCC veto counter. However, the Barrel veto counter does not satisfy the condition that 364 has a large scale along the z-axis, and the  $(\Delta z - D)$  is not negligible.

365 In the following section, some special treatment of the veto hit will be explained,

### 366 3.4.1 Barrel Veto Counters

367 The Barrel veto counters contain the Main Barrel(MB) and the Inner Barrel(IB), which 368 have a Both-End Readout system. The mechanism of the both-end readout veto hit is 369 shown in Figure 3.7. And the  $T_{mod}$  could be calculated by the upstream and downstream 370 PMT timing.

$$\begin{cases} T_{mod} = T_u - L_u/v, \\ T_{mod} = T_d - L_d/v \end{cases} \quad (3.28)$$

371 where the  $T_u$  and  $T_d$  are the timing of the upstream and downstream, and  $L_u(L_d)$  is the 372 distance between the hit position to the upstream (downstream) PMT,  $v$  is the propagated 373 velocity in the module. Therefore, the  $T_{mod}$  can be calculated by

$$T_{mod} = \frac{T_u + T_d}{2} - \frac{L}{2v} \quad (3.29)$$

<sup>374</sup> The hit position  $z_{hit}$  of the veto counter can be derived as

$$z_{hit} = z_{center} + \frac{v \cdot (T_u - T_d)}{2} \quad (3.30)$$

<sup>375</sup> where the  $z_{center}$  is the  $z$  position of the center of the barrel veto counter.

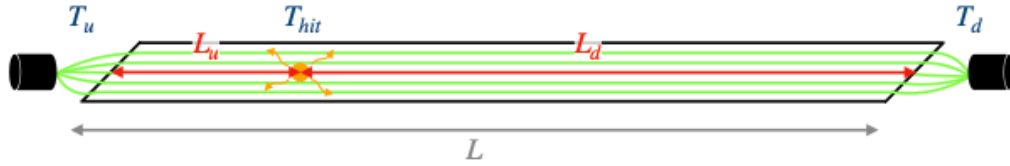


FIGURE 3.7: The Schematic diagram of a photon hit with the generated scintillation lights propagating to both directions and captured by PMTs. Figure courtesy of [15]

<sup>376</sup> The geometry relationships of the Barrel veto hit are shown in Figure 3.8. The  $(\Delta z - D)$  from Equation 3.26 can be approximated by

$$\Delta z - D \approx \Delta S, \quad (3.31)$$

$$\Delta S = \sqrt{R^2 + (z_{hit} - z_{CsI})^2} \quad (3.32)$$

<sup>378</sup> where  $R$  is the radius of the Barrel veto counter. And the  $T_{veto}$  can be derived as

$$T_{veto} = T_{mod} - T_{CsI} + \Delta S/c \quad (3.33)$$

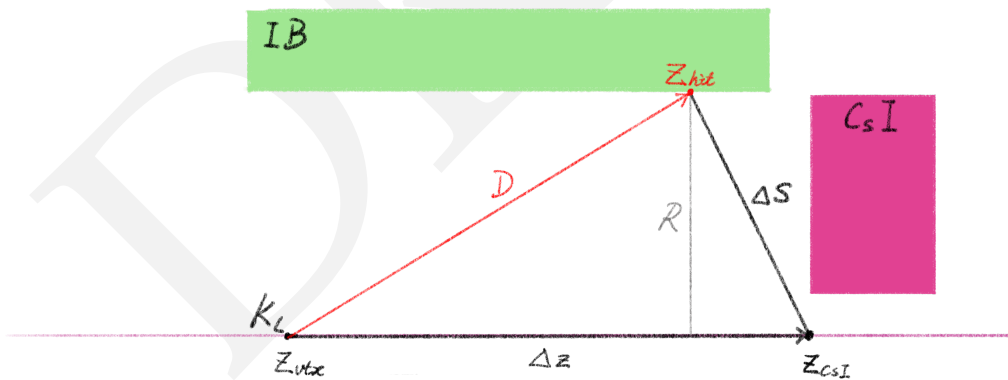


FIGURE 3.8: The Schematic diagram of geometry relationships of the Barrel veto counter.

### <sup>379</sup> 3.4.2 CsI Calorimeter

<sup>380</sup> As Section 3.1 mentioned, the CsI calorimeter is used to reconstruct the photon cluster.  
<sup>381</sup> All the crystal hits on the CsI Calorimeter will be used in the clustering process. How-  
<sup>382</sup> ever, some crystal hits cannot be assigned to any cluster, and these hits are defined as  
<sup>383</sup> "Isolated Crystal Hits". Even though a cluster has been constructed, if it does not satisfy

384 the  $\pi^0$  reconstruction criteria, it will not be assigned to any  $K_L^0$  or  $\pi^0$ , and these clusters  
 385 are defined as "Extra Clusters". The mechanism of these hits could come from a photo-  
 386 nuclear reaction in the shower propagation. These two types of hits will be used in the  
 387 veto rejection.

388 Because this detector is also the calorimeter, the veto timing definition needs to be  
 389 modified. For the "extra clusters" the timing of the decay vertex ( $T_{vtx}$ ) is not recalculated  
 390 for each cluster,

$$T_{vtx} = T_{cluster} - L/c \quad (3.34)$$

391 where  $L$  is the distance between the decay vertex and the cluster.

392 For the "isolated crystal hits", because it possibly split from the other cluster. To avoid  
 393 this situation, the selection criteria variables are correlated to the nearest cluster. The  
 394 variable that needs to be reconstructed is the distance ( $D$ ) and the timing difference ( $T$ )  
 395 between the isolated crystal hit and the nearest cluster.

$$T_{veto} = T_{crystal} - T_{cluster} \quad (3.35)$$

$$D = \sqrt{(x_{crystal} - x_{cluster})^2 + (y_{crystal} - y_{cluster})^2} \quad (3.36)$$



<sup>396</sup> **Chapter 4**

<sup>397</sup> **Monte Carlo Simulation**

<sup>398</sup> In this chapter, the Monte Carlo (MC) simulation of the KOTO experiment is described,  
<sup>399</sup> which is used for the  $K_L^0 \rightarrow \gamma\bar{\gamma}$  analysis. In the HEP analysis field, there are so many  
<sup>400</sup> physics mechanisms behind the physics data, to verify these mechanisms, the MC simu-  
<sup>401</sup> lation is used to simulate the physics process to help us understand the data behaviors.  
<sup>402</sup> The simulations were performed to reproduce real physics data and to estimate the  $K_L^0$   
<sup>403</sup> source background events. The MC simulation should reproduce the real data as much  
<sup>404</sup> as possible. Ideally, if all the background sources and mechanisms are well considered,  
<sup>405</sup> the MC simulation should reproduce the real data perfectly.

<sup>406</sup> The simulation procedure consists of the following steps. First, generate a set of  $K_L^0$   
<sup>407</sup> particles to enter the KOTO detector, simulate the decay of such particles in the detec-  
<sup>408</sup> tor, and simulate the detector response with the interaction of the decay products. The  
<sup>409</sup> simulation is performed using the GEANT4 toolkit [18, 19, 20]. Then convert the MC sim-  
<sup>410</sup> ulation result to the same format as the real data. To reproduce the same conditions of  
<sup>411</sup> the  $K_L^0$  as the real data run, a  $K_L^0$  momentum spectrum and beam structure are prepared  
<sup>412</sup> based on the real data. The MC simulation is performed with the same beam structure  
<sup>413</sup> and detector conditions as the real data. In addition, some other MC simulation is also  
<sup>414</sup> performed in this analysis to estimate the background events, such as the beamline sim-  
<sup>415</sup> ulation, upstream  $\pi^0$  background.

<sup>416</sup> **4.1 GEANT4 toolkit**

<sup>417</sup> GEANT4 (GEometry ANd Tracking) is a comprehensive software toolkit, which is pop-  
<sup>418</sup> ular in high energy physics, used for the simulation of the passage of particles through  
<sup>419</sup> matter. In the GEANT4 simulation, the simulation is performed step by step. In each  
<sup>420</sup> step, the particle interacts with the detector material, and the energy deposits and the  
<sup>421</sup> direction change of the particle are calculated. The particle quantities are all stored in the  
<sup>422</sup> simulation output, thus it is easy to analyze the particle decay because its whole proce-  
<sup>423</sup> dure is traceable.

## 424 4.2 Detector Response

425 The GEANT4 simulation toolkit can provide the timing, energy deposit, and position of  
 426 the particle interaction, but it is the ideal information, called "true information", which  
 427 cannot be directly compared with the real data. The kinematic information is recon-  
 428 structed from the data detected by sensors. Therefore, simulations are necessary to repli-  
 429 cate the information given by the detector readout.

430 The KOTO detector contains several sub-detectors with different detected principles.  
 431 The majority method uses the scintillation process, to detect the propagated light by PMT.  
 432 The Čerenkov radiation was used in the BHPV and BHGC, and the gas ionization was  
 433 used in the BHCV.

## 434 4.3 Pulse Simulation

435 The FADC digitized pulses can be described by an asymmetric Gaussian function  $f(t)$  as  
 436

$$f(t) = A \exp \left( - \left( \frac{t - \mu}{(\sigma_0 + a(t - \mu))} \right)^2 \right) \quad (4.1)$$

437 where  $t$  is the time of the pulse,  $\mu$  is the peak timing,  $\sigma_0$  and  $a$  are the parameters that  
 438 determine the shape of the pulse which are given for each detector channel.  $A$  is the  
 439 normalization factor determined by the integration of  $f(t)$  to energy.

## 440 4.4 $K_L^0$ Generation

441 In the Monte Carlo simulation, the  $K_L^0$  particles are generated at the  $K_L^0$  beam exit which  
 442 is 1507 mm upstream of the detector. Given the momentum and production position of  
 443 the  $K_L^0$  particles, the decay process can be simulated. There are two methods that can  
 444 obtain the momentum and position distribution, one is called beamline simulation and  
 445 the other is called the empirical  $K_L^0$  momentum spectrum.

### 446 4.4.1 Beamline Simulation

447 The  $K_L^0$  beam in the KOTO experiment is produced from the proton-gold fix target colli-  
 448 sions. The simulation that starts from the proton collisions is called the beamline simula-  
 449 tion. Because the beamline simulation simulates the whole beamline, the  $K_L^0$  momentum  
 450 and position can be obtained directly.

451 In the simulation, a 30 GeV proton beam hit the gold target was simulated. The beam-  
 452 line simulation simulates all the structures between the target and the 2nd collimator exit,  
 453 such as the photon absorber, sweeping magnet, and two collimators. If any particles re-  
 454 main at the 2nd collimator exit, the event will be recorded as an event seed. However,  
 455 the beamline simulation is inefficient to generate and cannot reproduce the  $K_L^0$  spectrum

perfectly. In the KOTO experiment, the empirical method is used to obtain the  $K_L^0$  momentum and position distribution.

Although the beamline simulation cannot be used to obtain the  $K_L^0$  spectrum, it is still useful to study the beam contents other than the  $K_L^0$  particles. Figure 4.1 shows the beam content population simulated by the beamline simulation under  $10^{12}$  POT.

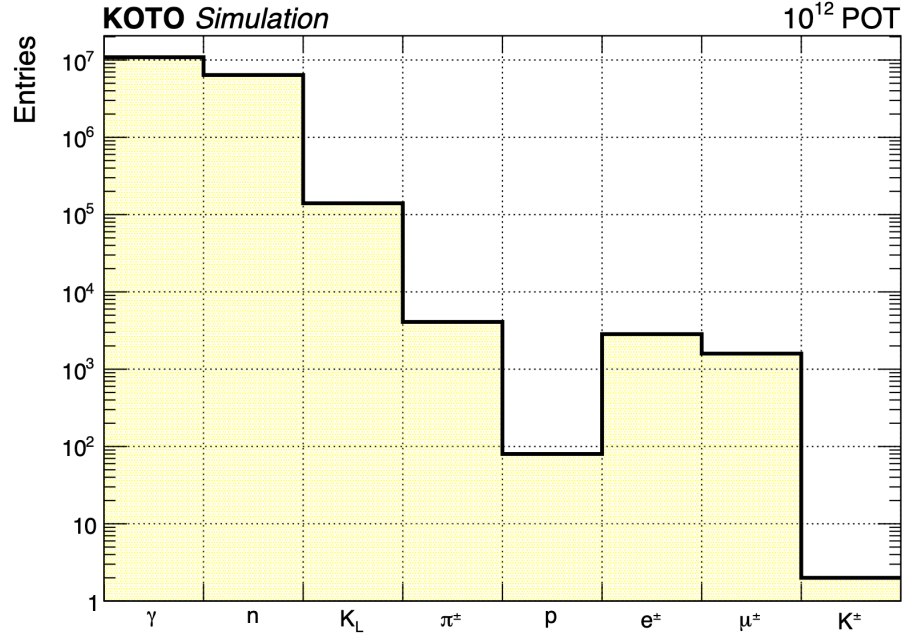


FIGURE 4.1: Beam content at the KOTO detector entrance based on the beamline simulation. Figure courtesy of [15]

In the KOTO experiment, the beamline simulation is used to study some background sources caused by the in-beam particle interaction, such as the NCC background, the halo  $K_L^0$  background, and the Charge Kaon background.

#### 4.4.2 Empirical $K_L^0$ Spectrum Simulation

The  $K_L^0$  momentum spectrum was obtained from the measurement result of the  $K_L^0 \rightarrow \pi^+ \pi^-$  and  $K_L^0 \rightarrow \pi^+ \pi^- \pi^0$  decays in 2012 engineering run [21]. Figure 4.2 shows the  $K_L^0$  momentum spectrum which is fitting by the asymmetry Gaussian function as

$$f(p) = \exp\left(-\frac{(p - \mu)^2}{2\sigma_0(1 - (A + Sp)(p - \mu))^2}\right) \quad (4.2)$$

where  $p$  is the momentum of the  $K_L^0$ ,  $\mu = 1.420$  GeV/c is the mean value of the momentum,  $\sigma_0 = 0.8102$  GeV/c is the width of the momentum,  $A = -0.3014$  and  $S = 0.01709$  (GeV/c)<sup>-1</sup> are the asymmetry parameters to be determined by fitting.

However, compared to the beamline simulation and empirical model, the  $K_L^0$  particles around the beam core (halo  $K_L^0$  particle) are not reproduced by the empirical model, as

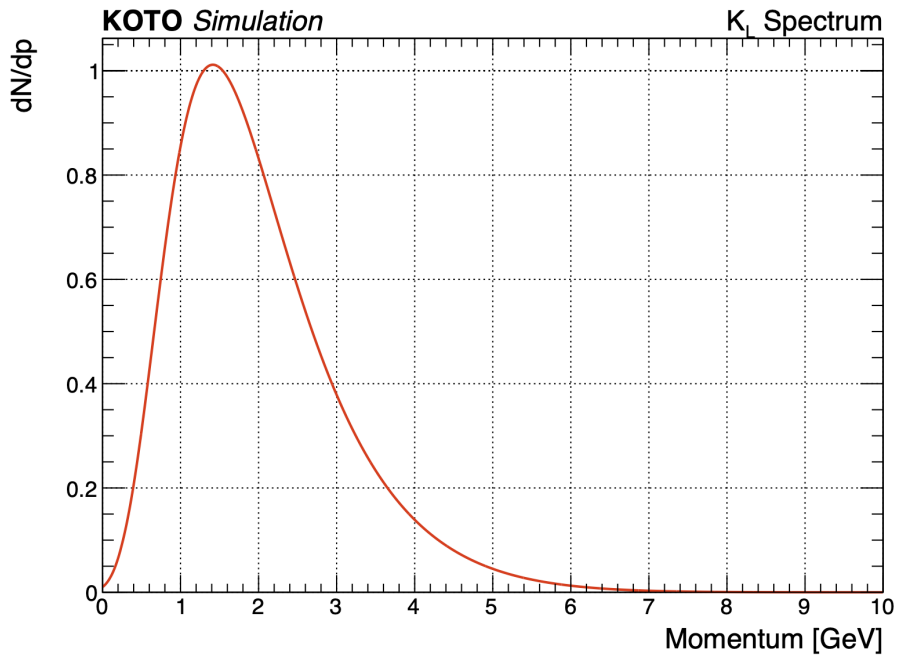


FIGURE 4.2: The  $K_L^0$  momentum spectrum at the exit of the second collimator. Figure courtesy of [15]

473 shown in Figure 4.3. This is because the empirical model does not consider the interactions  
 474 in the beamline. Therefore, the halo  $K_L^0$  may contribute to a background source and  
 475 need to be emulated by the beamline simulation.

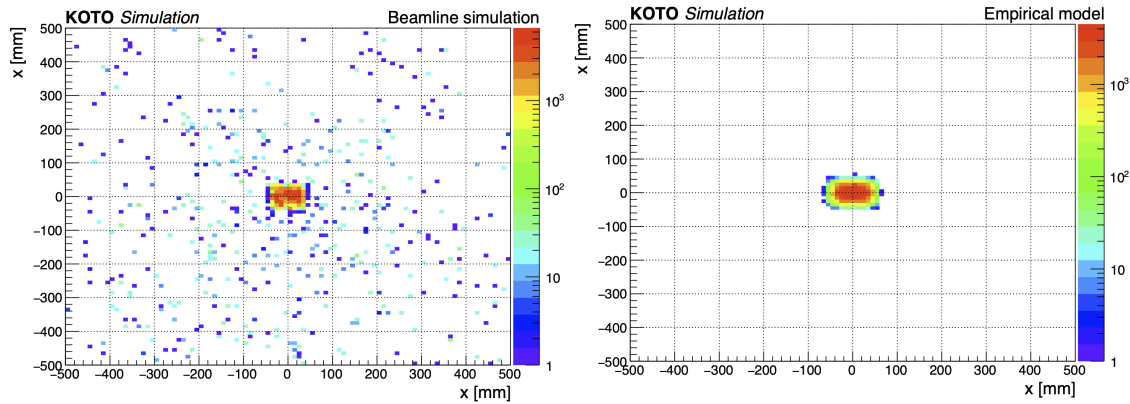


FIGURE 4.3: Comparison of  $K_L^0$  beam profile at the exit of the second collimator between the beamline simulation and the empirical model. Figure courtesy of [15]

## 476 4.5 Fast Simulation

477 Because the KOTO experiment has a large amount of data, the Monte Carlo simulation is  
 478 time-consuming. Especially for the large branching ratio  $K_L^0$  decay channels, such as the  
 479  $K_L^0 \rightarrow \pi^\pm e^\mp \nu_e$  and  $K_L^0 \rightarrow 3\pi^0$  decays. It not only takes a long time to simulate the decay  
 480 process but also occupies a large amount of disk space.

481 Take this study as an example, there are only 2-hour physics data with the protons  
 482 on target (POT) of  $5.03 \times 10^{16}$ . A full MC simulation of a  $K_L^0 \rightarrow 3\pi^0$  decay would take  
 483 approximately 3 days to generate the same decay statistics as data. In this study, we  
 484 ended up generating 12 times as many  $K_L^0 \rightarrow 3\pi^0$  decays as the same amount of data.  
 485 If we use the full MC simulation method, it would take around 30 days to generate the  
 486 same statistics. The time consumption does not consider the priority of the batch job  
 487 system, which consumes more time in real time. The branching ratio of  $K_L^0 \rightarrow \pi^\pm e^\mp \nu_e$   
 488 and  $K_L^0 \rightarrow \pi^\pm \mu^\mp \nu_\mu$  are even larger than the  $K_L^0 \rightarrow 3\pi^0$  decay. To prevent wasting the  
 489 whole life being spent on the MC simulation, a fast simulation method is developed to  
 490 speed up the MC simulation.

491 The fast simulation method is the same as the full simulation but breaks the generation  
 492 process into three steps. In the first step, the  $K_L^0$  and its daughter particles are generated,  
 493 and stop the simulation when they hit any detectors. Record the information that we are  
 494 interested in. In the second step, make a simple selection of the events to reject the events  
 495 that are not interested in. Take the  $K_L^0 \rightarrow 3\pi^0$  decay as an example, only the photon  
 496 decay from the  $\pi^0$  was considered. The photon has to hit the CsI fiducial region and the  
 497 decay vertex has to be before the CsI. Retention events pass the above selection, require a  
 498 minimal number of photons which depends on the study, and require the total energy of  
 499 the photon to be larger than the online trigger threshold. In the third step, based on the  
 500 information of the retained events, restarted the simulation and simulated the detector  
 501 response.

502 The fast simulation method is much faster than the full simulation. In the  $K_L^0 \rightarrow 3\pi^0$   
 503 decay case, the total MC simulation is done in 10 days which is 3 times faster than the  
 504 full simulation. The enhancement of the speed depends on the selection criteria, if a more  
 505 strict selection is applied, the enhancement of the speed will be more significant.

## 506 4.6 Accidental Overlay

507 Because the MC simulation is generated one by one  $K_L^0$  decays which is the ideal simulation  
 508 To reproduce the real data situation, the accidental activities need to be considered.  
 509 For example, the triggered  $K_L^0$  decay event with another  $K_L^0$  decay coincidently, or the  
 510 particle in the beam has some interaction and produces a cluster. To reproduce the acci-  
 511 dental activities, the accidental activities were overlaid on the MC simulated events. The  
 512 accidental activities' information was taken from the TMON-triggered data, which could  
 513 reflect the accidental rate of the real data beam.

514 When doing the accidental overlay, an accidental event is randomly selected from the  
 515 library, and superimposed to each channel of the event data. Figure 4.4 shows an example  
 516 of an accidental overlay on a simulated pulse for a channel in the FBAR detector.

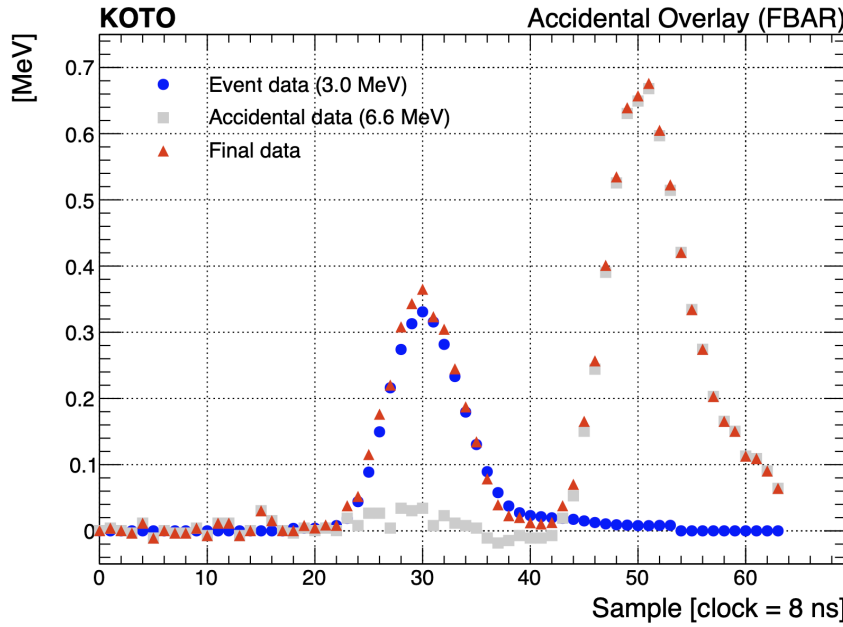


FIGURE 4.4: An example of the accidental overlay on a simulated pulse, subtracting the pedestal.  
Figure courtesy of [15]

## 517 4.7 Neutron background Simulation

518 Neutron background is one of the serious background sources in the KOTO experiment.  
 519 As shown in Figure 4.1, there is a large amount of neutron background in the beam.  
 520 The mechanism is simply neutron directly interacts with the CsI calorimeter. Because  
 521 the GEANT4 toolkit cannot generate a good reliable neutron interaction simulation, a  
 522 data-driven method is used to estimate the neutron background. An aluminum plate  
 523 target was inserted in front of the KOTO detector entrance perpendicularly to the beam  
 524 direction to enhance the neutron in the beam. This target is called the "Z0-Al target" and  
 525 the run with the Z0-Al target is called the "Z0-Al run". The Z0-Al run data is used to be  
 526 the neutron sample in the background suppression and the estimation study.

<sup>527</sup> **Chapter 5**

<sup>528</sup>  **$K_L^0$  Yield Estimation**

<sup>529</sup> The yield of  $K_L$  is an important parameter for most analysis in KOTO. To normalize the  
<sup>530</sup> Monte Carlo Simulation number of events to the real data, the yield of the  $K_L z$  was  
<sup>531</sup> required. The  $K_L$  yield is usually estimated by well-known neutral decay channels with  
<sup>532</sup> large branching ratios, which are  $K_L^0 \rightarrow 3\pi^0$ ,  $K_L^0 \rightarrow \pi^0\pi^0$ , and  $K_L^0 \rightarrow 2\gamma$ . The branching  
<sup>533</sup> ratio of these three decays is shown in the Table 5.1. The background source of these three  
<sup>534</sup> channels is also limited.

TABLE 5.1: Branching ratio of  $K_L$  decays

Decay mode	Branching ratio
$K_L^0 \rightarrow 3\pi^0$	$(19.52 \pm 0.12)\%$
$K_L^0 \rightarrow \pi^0\pi^0$	$(8.64 \pm 0.06) \times 10^{-4}$
$K_L^0 \rightarrow 2\gamma$	$(5.47 \pm 0.04) \times 10^{-4}$

<sup>535</sup> The ideal decay channel for the normalization study is  $K_L^0 \rightarrow 2\gamma$  decay because the  
<sup>536</sup> diphoton final state is relatively similar to the  $K_L^0 \rightarrow \gamma\bar{\gamma}$  decay. However, due to insuffi-  
<sup>537</sup> cient time for collecting special run data, the statistics of  $K_L^0 \rightarrow \pi^0\pi^0$  and  $K_L^0 \rightarrow 2\gamma$  decay  
<sup>538</sup> are inadequate to estimate the  $K_L^0$  yield. The  $K_L^0 \rightarrow 3\pi^0$  decay is a good place to estimate  
<sup>539</sup> the  $K_L$  yield because its branching ratio is far greater than other neutral decay channels,  
<sup>540</sup> and a restrictive requirement of the signal signature. Therefore, the  $K_L^0 \rightarrow 3\pi^0$  decay was  
<sup>541</sup> accepted to estimate the  $K_L^0$  yield and do the normalization study in this search. If we  
<sup>542</sup> can get more statistics from the data set, we could do On further study of this search with  
<sup>543</sup> better statistics, the normalization study could be based on  $K_L^0 \rightarrow 2\gamma$  decay, and use the  
<sup>544</sup> other two decays to do the cross-check.

<sup>545</sup> **5.1 Data Set**

<sup>546</sup> The whole special run physics data with the normalization trigger was treated as the data  
<sup>547</sup> sample. The pre-scaling factor used to scale the number of events collected is set as 13.  
<sup>548</sup> The control sample uses the Monte Carlo simulation of  $K_L^0 \rightarrow 3\pi^0$  including the acciden-  
<sup>549</sup> tal overlay. Because of the restrictive signal signature of the  $K_L^0 \rightarrow 3\pi^0$ , the contribution  
<sup>550</sup> of other decay modes can be ignored in the normalization study.

551 In this study,  $1 \times 10^9 K_L^0 \rightarrow 3\pi^0$  decays were prepared for the control sample.

## 552 5.2 Event Selections

553 In the  $K_L^0$  Yield study, the event selection aims to purify the  $K_L^0 \rightarrow 3\pi^0$  decay events  
 554 and reject corresponding background events. The event selection consists of the veto  
 555 cut and kinematic cut. The veto cut is a simple criterion of an in-time hit in the veto  
 556 counter. The kinematic cut is based on the photon information and the reconstructed  
 557 physics quantities of  $K_L^0$  and  $\pi^0$ . The kinematic cut could be categorized by Trigger Cut,  
 558 Photon Selection, and  $K_L^0$  Selection. A detailed explanation of the cut is shown in the  
 559 following section.

### 560 5.2.1 Trigger Cut

561 Because the Monte Carlo simulation could not reproduce the online DAQ system. Thus,  
 562 it doesn't have the same trigger condition as the real data. The trigger cut was introduced  
 563 to eliminate the online trigger effect.

### 564 Trigger Timing Window

565 In one 64-sample window, there may maybe more than one trigger hit. If there are sep-  
 566 arate events, it may cause a double counting of overlay events. To eliminate the bias  
 567 from this effect, an average photon timing window of  $\pm 15$  ns of the nominal timing was  
 568 required.

### 569 Total Energy in CsI

570 The online Total energy in CSI (CSIET) threshold is set as 500 MeV in the special physics  
 571 run normalized trigger. To eliminate this online effect, a CSIET threshold offline was  
 572 required higher than the online threshold. In this study, an offline  $CSIET$  threshold of  
 573 650 MeV was required, which is the same as the  $K_L^0 \rightarrow \pi^0\nu\bar{\nu}$  study. The offline CSIET  
 574 threshold is determined by examining the ET efficiency curve, as explained in Section  
 575 6.3.1 of Jay's dissertation[15].

### 576 5.2.2 Photon Selection

577 Figure 5.1 shows the distribution of the photon selection variables for the  $K_L^0 \rightarrow 3\pi^0$   
 578 decay. The photon selection cuts include the photon energy, photon hit position, and  
 579 minimum cluster distance. These cuts are based on the photon information and are used  
 580 to select photons with good reconstruction reproducibility.

#### 581 Photon Energy ( $E_\gamma$ )

582 To improve the reconstruction quality of the photon, the ultra-soft photon with energy  
 583 less than 50 MeV was rejected.

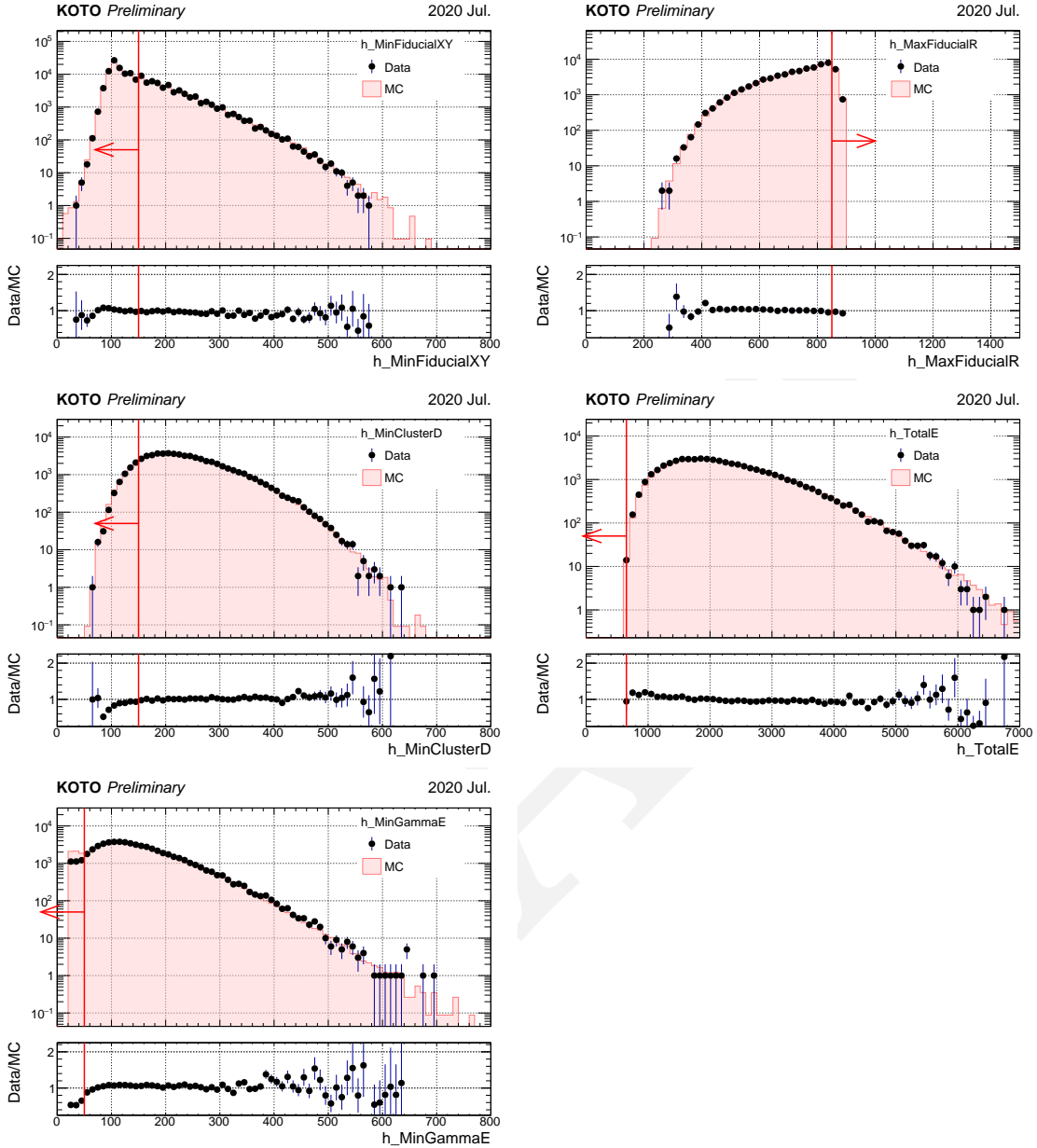


FIGURE 5.1: Distribution of the photon selection variables for the  $K_L^0 \rightarrow 3\pi^0$  decay. The photon selection cuts are applied except for the variable shown in the plot. The black point shows the data, and the fill histogram shows the Monte Carlo simulation. The red arrow indicates the cut-off value of the variable.

#### 584 Photon Hit Position (Fiducial Cut)

585 To ensure the EM shower was well contained in the CsI calorimeter, a photon hit position  
 586 cut was applied. Any photon in an event that hit the outermost and innermost edge  
 587 of the CsI calorimeter was rejected. This cut is also called the Fiducial Cut. The outer  
 588 boundary requires the radius of the photon hit position within 850 mm,  $R_\gamma < 850$  mm,  
 589 while the inner boundary requires the photons 150 mm away from the square beam hold,  
 $\min\{|x_\gamma|, |y_\gamma|\} > 150$  mm.

591 **Minimum Cluster Distance**

592 If two-photon clusters are too close to each other, the EM shower may overlap, and the  
 593 energy reconstruction will be incorrect, or the two photons may be misidentified as one  
 594 photon. To avoid this situation, a minimum cluster distance of 150 mm was required.

595 **5.2.3  $K_L^0$  Selection**

596 Figure 5.2 and 5.3 show the distribution of the  $K_L^0$  selection variables for the  $K_L^0 \rightarrow 3\pi^0$   
 597 decay. The  $K_L^0$  selection cuts include the  $\chi^2$  of the decay Z,  $\Delta T$  of the vertex,  $K_L^0$  decay  
 598 vertex Z,  $K_L^0$  mass,  $K_L^0 P_T$ ,  $\Delta\pi^0$  mass, and  $K_L^0 \Delta Z_{vtx}$ .

599  $\chi_z^2$

600 To make sure the reconstructed  $\pi^0$  is good quality, the  $\chi_z^2$  cut was applied. The  $\chi_z^2$  could  
 601 indicate the goodness of the photon pair to the  $\pi^0$  reconstructed, defined in Equation

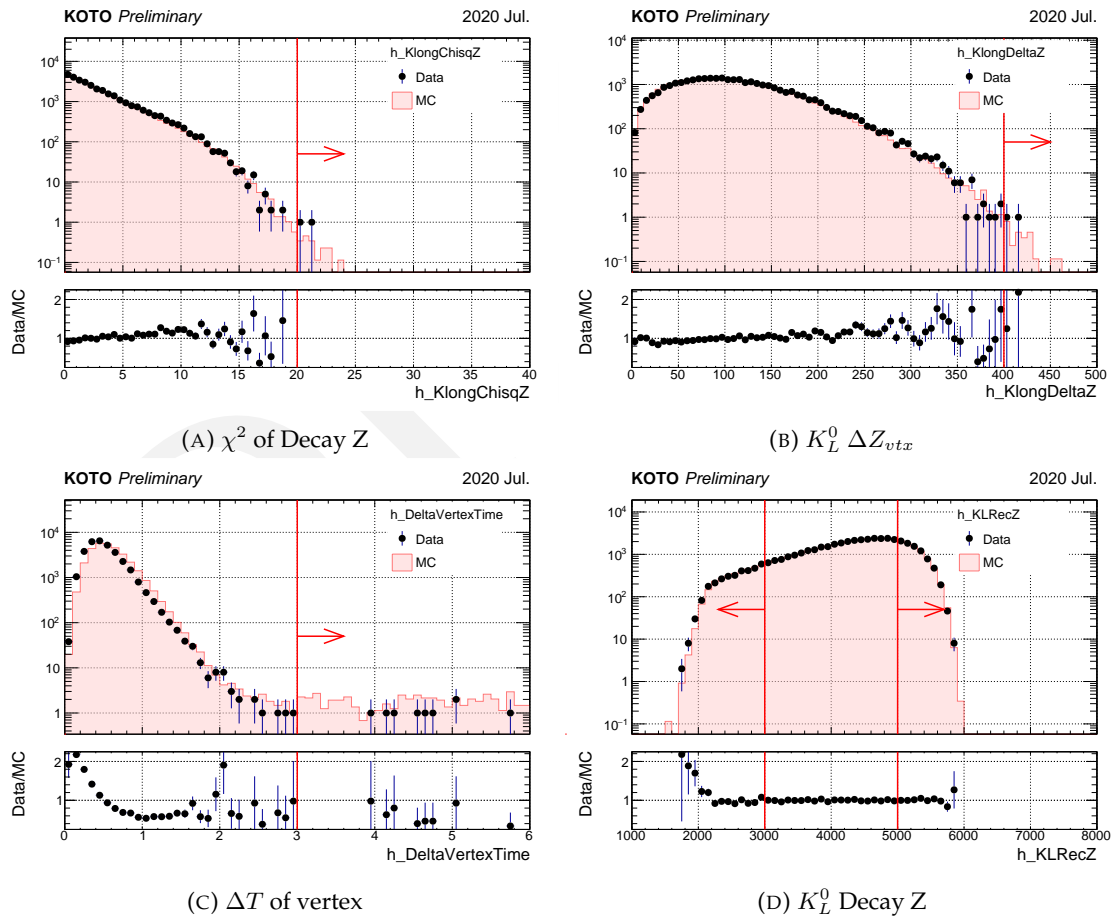


FIGURE 5.2: Distribution of the  $K_L^0$  selection variables for the  $K_L^0 \rightarrow 3\pi^0$  decay. The photon and  $K_L^0$  selection cuts are applied except for the variable shown in the plot. The black point shows the data, and the fill histogram shows the Monte Carlo simulation. The red arrow indicates the cut-off value of the variable.

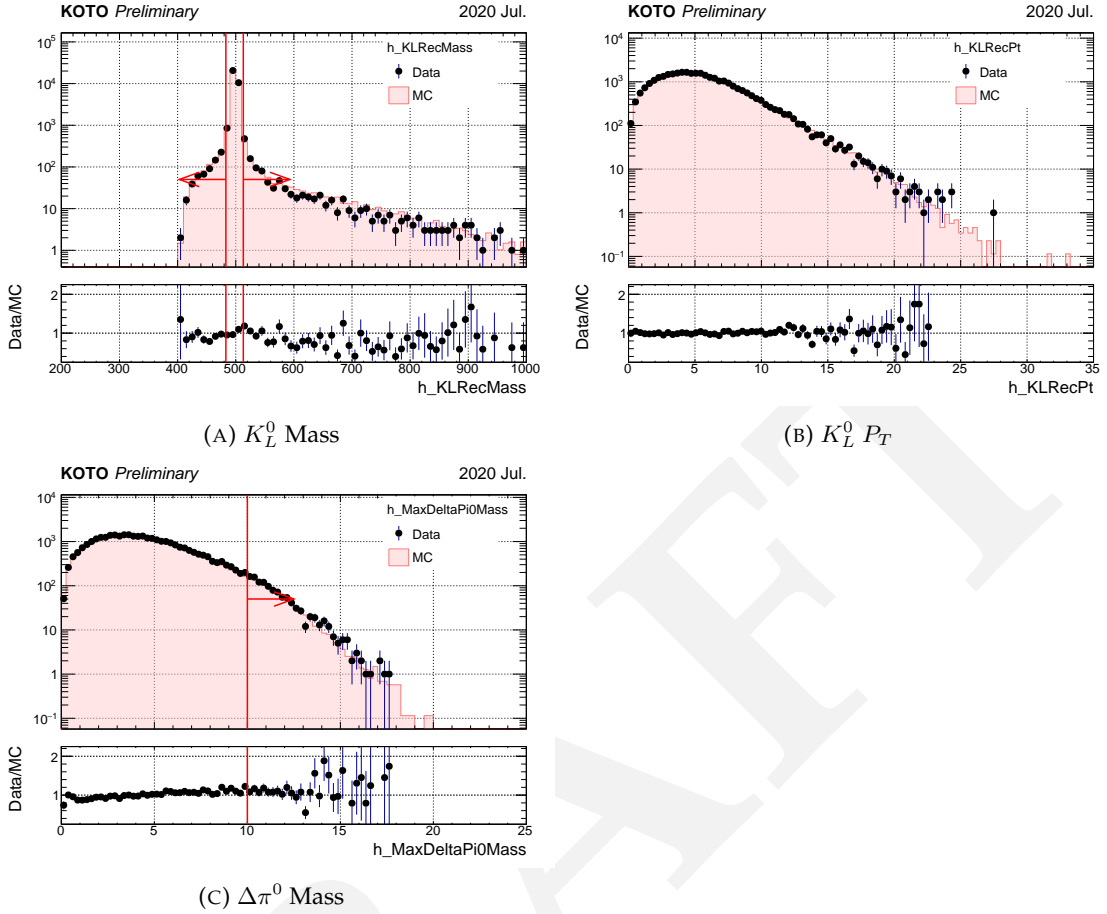


FIGURE 5.3: Distribution of the  $K_L^0$  selection variables for the  $K_L^0 \rightarrow 3\pi^0$  decay. The photon and  $K_L^0$  selection cuts are applied except for the variable shown in the plot. The black point shows the data, and the fill histogram shows the Monte Carlo simulation. The red arrow indicates the cut-off value of the variable.

602    3.13. This cut was used to ensure the consistency of the reconstructed  $\pi^0$  vertex, and the  
 603     $\chi_z^2$  was required to be less than 20.

#### 604    $K_L^0 \Delta Z_{vtx}$

605    The  $\Delta Z_{vtx}$  is defined as the maximum difference between the reconstructed  $\pi^0$ 's, as  
 606    shown in Equation 5.1. This cut is also used to ensure the consistency of the reconstructed  
 607     $\pi^0$  vertexes. The  $\Delta Z_{vtx}$  was required to be less than 400 mm.

$$\Delta Z_{vtx} = \max \left( |Z_{vtx}^i - Z_{vtx}^j| \right) \quad (5.1)$$

#### 608    Maximum Difference of Vertex Timing ( $\Delta T_{vtx}$ )

609    The vertex timing of each photon cluster that belongs to the same event should be con-  
 610    sistent with each other. The maximum vertex timing difference between reconstruc-  
 611     $K_L^0$  and each photon cluster was required to be less than 3 ns.

612  **$K_L^0$  Decay Vertex Z ( $Z_{vtx}$ )**

613 The Decay vertex of the  $K_L^0$  was required within the decay volume of the KOTO detector,  
 614  $3000 \text{ mm} \leq Z_{vtx} \leq 5000 \text{ mm}$ .

615  **$K_L^0$  Mass**

616 In the reconstruction of  $K_L$ , the invariant mass of photons was required to be within  
 617  $\pm 15 \text{ MeV}/c^2$  of the nominal  $K_L$  mass of  $497.614 \text{ MeV}/c^2$ [22]. This criterion significantly  
 618 reduces event contamination from mispairing in both the  $K_L \rightarrow 3\pi^0$  analyses. It also  
 619 minimizes the interference of  $K_L \rightarrow 3\pi^0$  decays in the analysis.

620  **$K_L^0 P_T$**

621 In the normalization study,  $K_L^0$  should not have missing particles, so the reconstructed  
 622 transverse momentum ( $P_T$ ) of the  $K_L^0$  is expected to be small. The  $P_T$  of the  $K_L^0$  was  
 623 required to be less than  $50 \text{ MeV}/c$ .

624  **$\Delta\pi^0$  Mass**

625 The  $\Delta\pi^0$  mass is the difference between the reconstructed  $\pi^0$  mass and the nominal  $\pi^0$   
 626 mass of  $134.9766 \text{ MeV}/c^2$ [22]. The  $\pi^0$  mass was calculated by the reconstructed  $K_L^0$  de-  
 627 cay vertex. A large  $\Delta\pi^0$  mass indicates a bad pairing of the photon cluster, which may  
 628 come from the accidental hit. The reconstructed  $\Delta\pi^0$  mass was required to be within  
 629  $\pm 10 \text{ MeV}/c^2$  of the nominal  $\pi^0$  mass.

630 **5.2.4 Veto Cut**

631 All the veto cuts applied to the yield study are the same as the veto cuts used in the  
 632  $K_L^0 \rightarrow \pi^0\nu\bar{\nu}$  analysis[15]. The summary of the veto cut is shown in Table 5.2.

633 In the following section, a detailed explanation of the Veto Cut is shown.

634 **Isolated Crystal Veto**

635 An isolated crystal hit very close in time to the photon clusters are possibly comes from  
 636 the same  $K_L^0$  decay. To reject this kind of background, a timing window of  $\pm 10 \text{ ns}$  of the  
 637 nearest photon cluster timing is required in this veto. A multistep cut based on the hit  
 638 Energy(E) and Distance(D) from the closest cluster is applied, as the following equation:

$$\begin{cases} E > 10 \text{ [MeV]} & , \text{if } D < 200 \text{ [mm]} \\ E > 10 - \frac{7 \cdot (D - 200)}{400} \text{ [MeV]} & , \text{if } 200 \leq D \leq 600 \text{ [mm]} \\ E > 3 \text{ [MeV]} & , \text{if } D > 600 \text{ [mm]} \end{cases} \quad (5.2)$$

639 As shown in Figure 5.4, a higher energy threshold is required for the isolated crystal  
 640 to hit nearer to the cluster, to bypass the shower propagation effect.

TABLE 5.2: Summary of the veto cut

Veto Counter	Energy Threshold	Timing Window
FB	1 MeV	51ns
NCC and HINEMOS	1 MeV	40ns
MB	1 MeV	20ns
IB	1 MeV	20ns
MBCV	0.5 MeV	60ns
IBCV	0.5 MeV	60ns
CV	0.2 MeV	20ns
LCV	0.6 MeV	30ns
CSI (isolated crystal)	see Sec. 5.2.4	20ns
CSI (extra cluster)	see Sec. 5.2.4	20ns
OEV	1 MeV	20ns
CC03	3 MeV	30ns
CC04, CC05, CC06 (CSI crystal)	3 MeV	30ns
CC04, CC05, CC06 (plastic scintillator)	1 MeV	30ns
BPCV	1 MeV	24ns
BHCV <sup>1</sup>	221 eV	25ns
BHPV <sup>2</sup>	2.5 p.e.	15ns
BHGC <sup>3</sup>	2.5 p.e.	15ns

<sup>1</sup> BHCV requires hits in more than two modules.

<sup>2</sup> BHPV requires hits in more than three consecutive modules.

<sup>3</sup> BHGC veto accepts the number of equivalent photons instead of energy.

#### 641 Extra Cluster Veto

642 A cluster hit in the CsI calorimeter that is not associated with the  $\pi^0 \rightarrow \gamma\gamma$  decay is considered  
 643 an extra cluster. If the timing of the extra cluster is within  $\pm 10$  ns of the reconstructed  $\pi^0$   
 644 vertex time, it is considered as a background and rejected.

## 645 5.3 Yield Estimation

646 The Yield of the  $K_L^0$  ( $Y$ ) in the data set is defined by the following equation:

$$Y = \frac{N_{mode}}{\mathcal{BR}_{mode} \times A_{mode}} \quad (5.3)$$

647 where  $N_{mode}$  is the number of events,  $\mathcal{BR}_{mode}$  is the branching ratio, and  $A_{mode}$  is the  
 648 acceptance. The mode could be any decay channel of the  $K_L^0$ . The acceptance( $A_{mode}$ ) can  
 649 be evaluated by the Monte Carlo simulation, as the following equation:

$$A_{mode} = \frac{N_{remaind}}{N_{gen}} \quad (5.4)$$

650 where  $N_{remaind}$  is the number of events that pass the event selection, and  $N_{gen}$  is the  
 651 number of generated  $K_L^0$  decays. And because the  $K_L^0$  yield is proportional to the number  
 652 of protons on target (POT), the  $K_L^0$  flux ( $F$ ) can be defined as the yield per POT, as shown

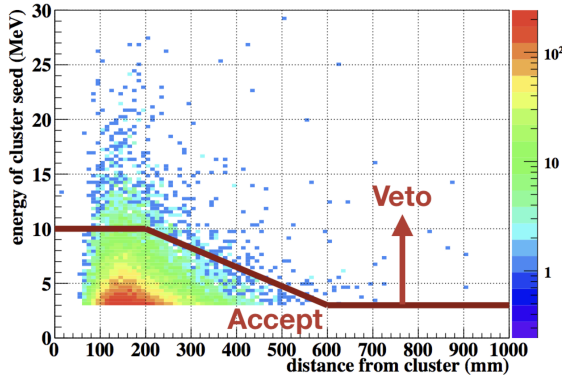


FIGURE 5.4: Distribution of isolated crystal hit energy( $E$ ) vs. its distance( $D$ ) from the nearest cluster. The red line shows the cut based on Equation 5.2. The sample was obtained from the  $K_L^0 \rightarrow \pi^0 \nu \bar{\nu}$  Monte Carlo simulation.[23]

653 in the following equation:

$$F = \frac{Y}{\text{POT}} \quad (5.5)$$

654 As mentioned in Section 5.1, the normalization trigger was used to be the data sample.  
 655 Because the normalization trigger was taken simultaneously with the physics trigger, the  
 656  $K_L^0$  yield is the same as the physics trigger. Therefore, the  $K_L^0$  yield evaluated by the  
 657 normalization trigger can be used directly in the physics analysis.

658 In this study, the  $K_L^0$  yield was estimated by the  $K_L^0 \rightarrow 3\pi^0$  decay. All the kinematic  
 659 cuts introduced in Section ?? and the veto cuts summarized in Table 5.2 were imposed.

### 660 5.3.1 Estimation by $K_L^0 \rightarrow 3\pi^0$ Decays

661 Figure 5.6 and 5.7 show the distribution of the kinematic variables for the  $K_L^0 \rightarrow 3\pi^0$   
 662 decay after imposed all selection cuts referred in Section 5.2. The purity of the  $K_L^0 \rightarrow 3\pi^0$   
 663 decay is high because there is no other  $K_L^0$  decay mode that can mimic the six-cluster  
 664 signature on CSI. The most discrepancy comes from the statistics of the special physics  
 665 data is not enough to match the Monte Carlo simulation.

666 Figure 5.5 shows the beam shape of the x and y projection at the exit of the second  
 667 collimator. The beam core shows a good agreement between the data and the Monte  
 668 Carlo simulation.

## 669 5.4 Summary of $K_L^0$ Yield Estimation

670 The  $K_L^0$  yield of the special physics run was estimated to be  $1.29 \times 10^{10}$  by the  $K_L^0 \rightarrow 3\pi^0$   
 671 decay as shown in Figure ???. The systematic uncertainty will be considered in the Single  
 672 Event Sensitivity (SES) study in Section 6.5.1.

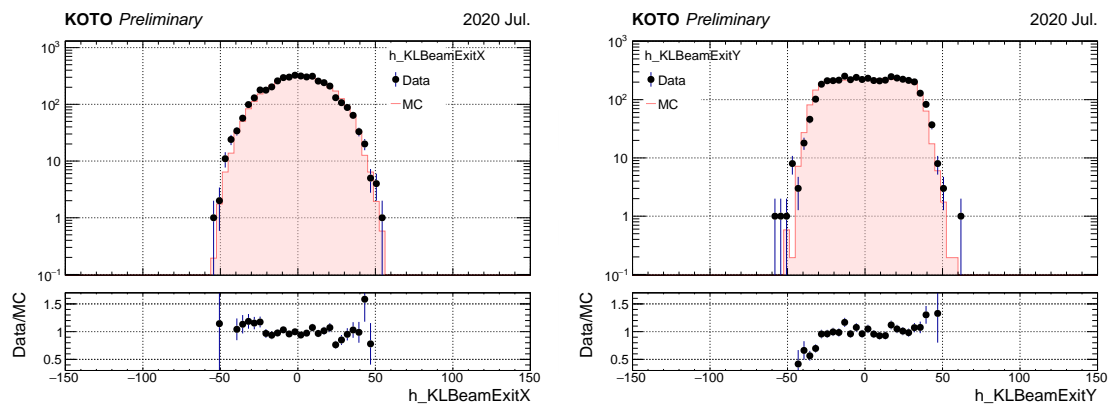


FIGURE 5.5: Beam profile at the exit of the second collimator via the  $K_L^0 \rightarrow 3\pi^0$  decay analysis. All the selection cuts are imposed. Filled histograms are predicted by the Monte Carlo simulation.

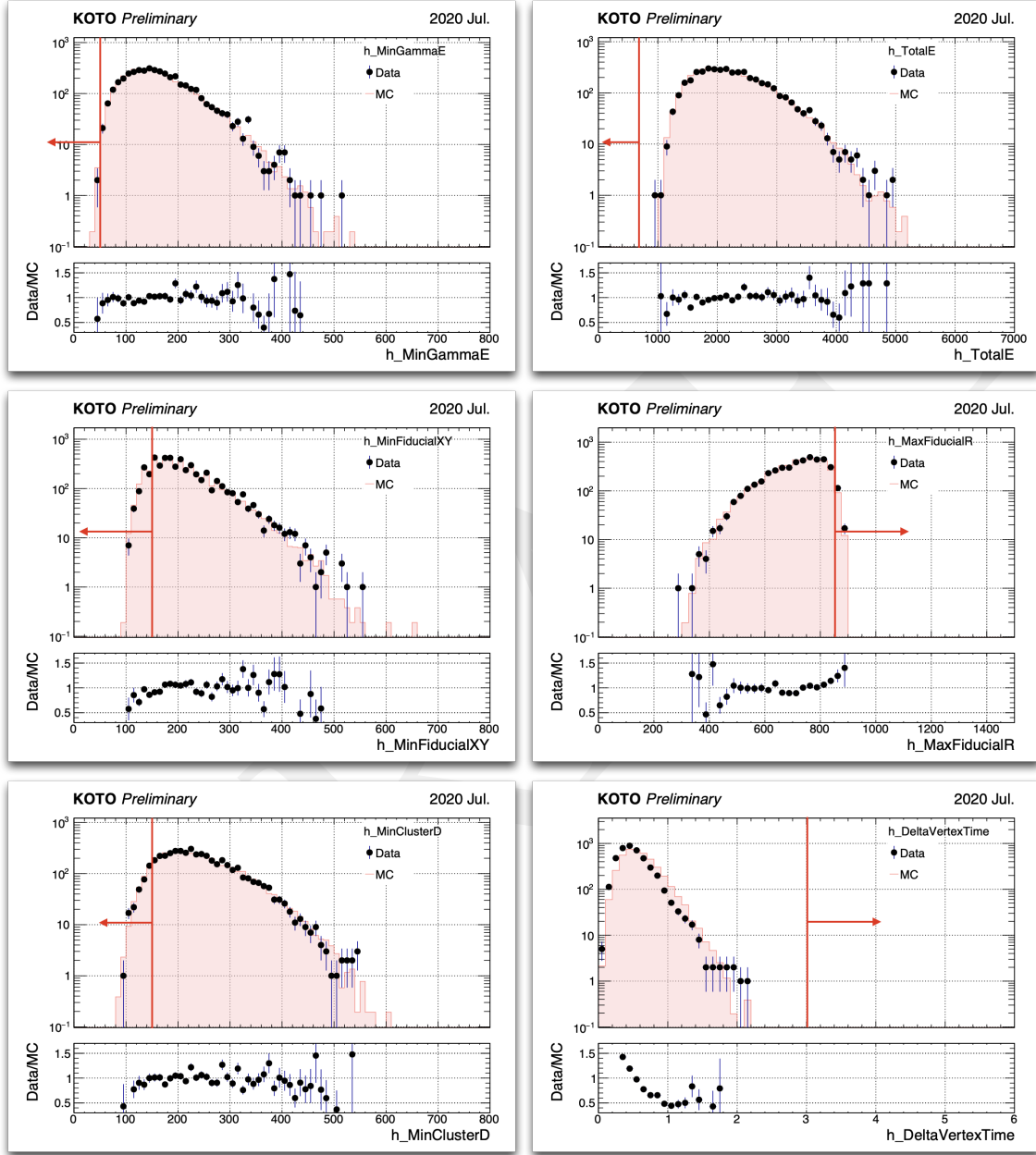


FIGURE 5.6: Distribution of the kinematic variables for the  $K_L^0 \rightarrow 3\pi^0$  decay. All the selections are applied except the variable shown in the plot. The black point shows the data, and the fill histogram shows the Monte Carlo simulation. The red arrow indicates the cut-off value of the variable.

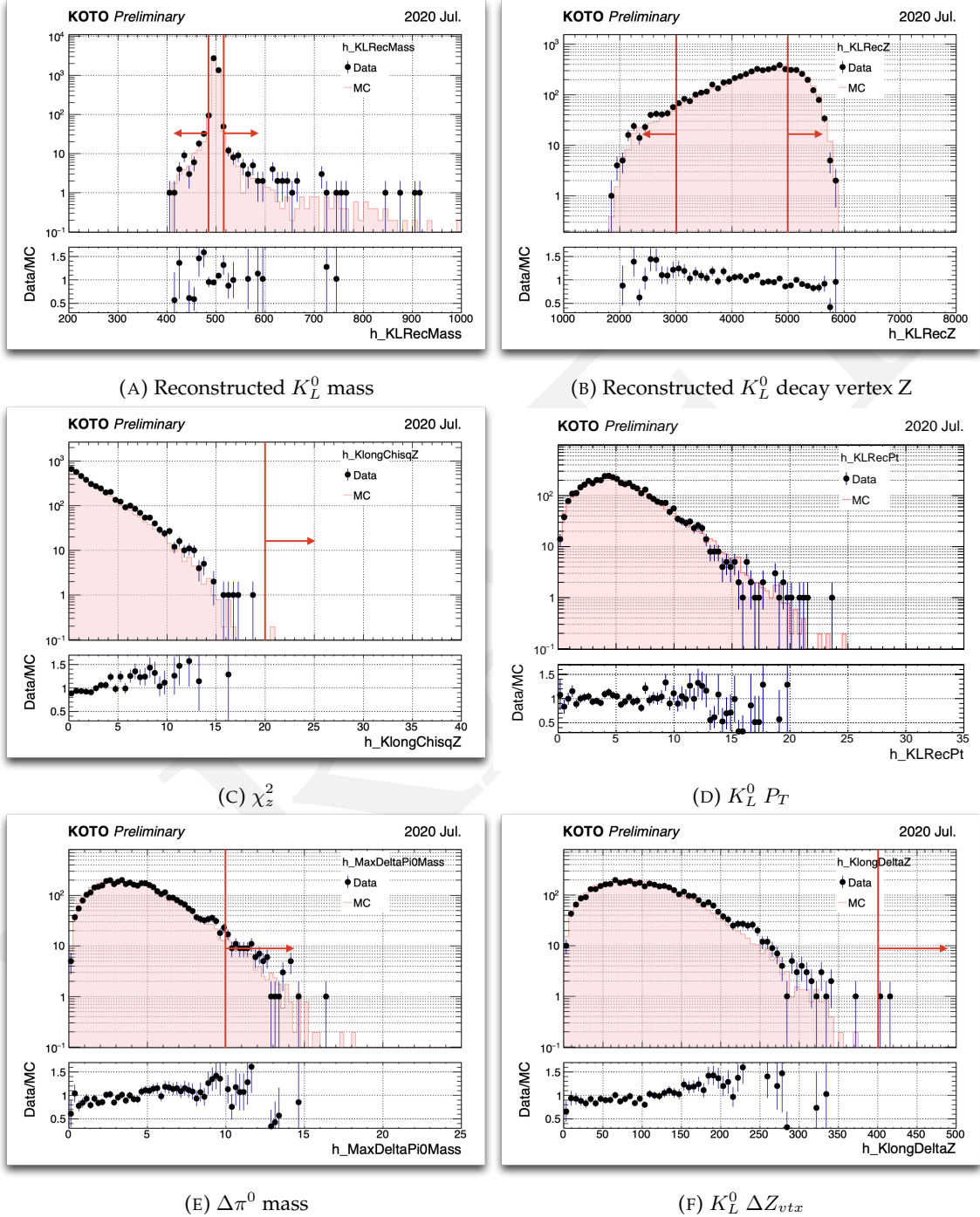


FIGURE 5.7: Distribution of the kinematic variables for the  $K_L^0 \rightarrow 3\pi^0$  decay. All the selections are applied except the variable shown in the plot. The black point shows the data, and the fill histogram shows the Monte Carlo simulation. The red arrow indicates the cut-off value of the variable.



<sup>673</sup> **Chapter 6**

<sup>674</sup> **Analysis of  $K_L \rightarrow \gamma\bar{\gamma}$**

<sup>675</sup> The goal of the  $K_L^0 \rightarrow \gamma\bar{\gamma}$  analysis is to estimate the branching ratio ( $\mathcal{BR}$ ) of this decay,  
<sup>676</sup> we took a 2-hour special run with a single cluster trigger in 2020. The distinctive signal  
<sup>677</sup> signature of  $K_L^0 \rightarrow \gamma\bar{\gamma}$  manifests as a singular photon hit on the CsI calorimeter, devoid  
<sup>678</sup> of any in-time hits on other detectors.

<sup>679</sup> Employing a blind analysis method, we define a specific region, characterized by en-  
<sup>680</sup> ergy deposition  $800 \text{ MeV} < E_\gamma < 3000 \text{ MeV}$  and a spatial constraint of  $300 \text{ mm} < H_{XY}$   
<sup>681</sup>  $< 850 \text{ mm}$ , where  $H_{XY}$  denotes the maximum distance between the hit location and the  
<sup>682</sup> center of the CsI crystal along the x and y axes. The signal region has to be within the  
<sup>683</sup> blind region and has been optimized.

<sup>684</sup> Our principal objective revolves around suppressing background noise and accentu-  
<sup>685</sup> ating signal events through event selection. Subsequently, we estimate the residual back-  
<sup>686</sup> ground events within the signal region post-selection. Under the assumption of negli-  
<sup>687</sup> gible background noise, we calculate the Single Event Sensitivity (SES) to estimate the  
<sup>688</sup> branching ratio upon observing signal events within the defined signal region. The SES,  
<sup>689</sup> representing the reciprocal of the product of the total  $K_L^0$  yield and the acceptance of  
<sup>690</sup> signal decays, is expressed mathematically as:

$$\text{SES} = \frac{1}{Y \times A_{sig}} \quad (6.1)$$

<sup>691</sup> Here,  $Y$  represents the  $K_L^0$  yield, and  $A_{sig}$  signifies the signal acceptance. The branching  
<sup>692</sup> ratio ( $\mathcal{BR}$ ) is then inferred from SES and the observed number of signal events ( $N_{sig}$ )  
<sup>693</sup> within the signal region, as articulated by:

$$\mathcal{BR} = \text{SES} \times N_{sig} \quad (6.2)$$

<sup>694</sup> However, when background contributions cannot be negligible, a statistical methodol-  
<sup>695</sup> ogy becomes imperative to ascertain the upper and lower bounds of signal event counts.  
<sup>696</sup> The background level ( $N_{bg}$ ) is estimated through two approaches in this study. For  $K_L$   
<sup>697</sup> decay backgrounds, Monte Carlo simulations are employed to evaluate  $N_{bg}$ , defined by:

$$N_{bg} = Y \times \mathcal{BR}_{bg} \times A_{bg} \quad (6.3)$$

698 Where  $\mathcal{BR}_{bg}$  represents the branching ratio of specific background decays (e.g.,  $K_L \rightarrow$   
 699  $2\gamma$ ), and  $A_{bg}$  denotes the acceptance corresponding to this background decay. For neu-  
 700 tron backgrounds, a dedicated neutron data run is utilized, employing a data-driven  
 701 approach for background-level evaluation through normalization against the neutron-  
 702 dominant region between physics data and neutron data sample. Upon combining all  
 703 background sources, a prediction of the background level within the signal region is de-  
 704 termined. After an examination of reliability through the side-band region, uncover the  
 705 blind region.

706 This chapter unfolds with a presentation of the event selection criteria, followed by  
 707 a discussion on background suppression methodologies. Subsequently, the reliability  
 708 of our analysis is assessed through a comparison between physics data and simulation  
 709 results in the side-band region. The computation of background levels and SES is then  
 710 detailed. With the final estimation in hand, we will proceed to open the box and the  
 711 interpretation of the statistical result will be presented at the latest.

## 712 6.1 Data Set

713 As mentioned in the above section, for this analysis a special 2-hour run was taken in June  
 714 2020 (RUN85). In this special run, a single cluster trigger was adopted as the physics data,  
 715 the energy threshold was set at 300 MeV with online veto and a pre-scale factor in 1. To  
 716 normalize this run, a normalization trigger is also accepted, this trigger does not contain  
 717 the cluster number trigger, and only adopts CV as the online veto, with a pre-scale factor  
 718 in 13. The POT of the 2-hour special is around  $5.03 \times 10^{-6}$  with the total  $1.29 \times 10^{10}$   
 719 number of  $K_L^0$  enter KOTO detector, as shown in Chapter 5.

720 For the neutron background study, a neutron sample run was taken. As Section 4.7  
 721 mentions, the GEANT4 MC toolkits cannot simulate the neutron interaction correctly,  
 722 so the data-driven method was adopted to do the neutron background study. Ideally,  
 723 for the single cluster study, a single cluster trigger neutron should be used in the study.  
 724 Following this thought, a special single cluster Z0-Al run was taken in RUN85. However,  
 725 after further study, we notice that the single cluster Z0-Al run cannot stand the neutron  
 726 sample. Because we don't have a good method to purify the neutron event from the Z0  
 727 data. Therefore, as a compromise, we use the 2-cluster trigger Z0 run in RUN85 which is  
 728 taken for the  $K_L^0 \rightarrow \pi^0 \nu\bar{\nu}$  decay study. The mechanism of the 2-cluster neutron event is  
 729 that a neutron hits the CsI calorimeter and generates a new hadron through the hadronic  
 730 interactions. Because there are two clusters on the CsI, the reconstruction was possible.  
 731 Consequently, use the kinematic variable to select the neutron event, then a pure neutron  
 732 sample data set was obtained. For the single cluster study, only the cluster with higher  
 733 energy was selected because the primary neutron usually has higher energy than the  
 734 second one.

Because the neutron flux is unable to be obtained, the background was normalized by the number of events in the neutron-dominated region in the neutron study. In this study, we adopt all Z0 data in RUN85, and the scale factor obtained by the normalization was around 1.6. This means the statistic of the neutron sample is far away to compare with physics data, it will behave on the statistical uncertainty.

## 6.2 Basic Strategy of the Single Cluster Study

### 6.2.1 Signal Identification

$K_L^0 \rightarrow \gamma\bar{\gamma}$  decay requires only one photon cluster to hit the CsI calorimeter and without any in-time hit in the rest of the detector. A single cluster can only provide the energy and position information. The lack of kinematic constraints will be the challenge of this study. Moreover, single cluster signatures are easily mimicked by some unknown arbitrary background. Requiring a high photon energy may help to suppress this kind of background but also reduce the signal efficiency.

### 6.2.2 Major Background Sources

The major background sources are  $K_L^0$  decay background and neutron-like background.

#### $K_L^0$ decay background

Table 6.1 shows the main  $K_L^0$  decay backgrounds. Other decay channels are unnecessary to be considered because of the low branching ratio. Only  $K_L^0 \rightarrow \pi^\pm e^\mp \nu_e$  and  $K_L^0 \rightarrow \pi^\pm \mu^\mp \nu_\mu$  are considered for the decay channel of charged particles in the final state, due to the high branching ratio. To suppress the  $K_L^0$  decay background, studying these decay channels and understanding their characteristics are important. All of these decay channels produce more than one photon in the final state. Therefore, it is easy to suppress these decay channels with the KOTO detector. Except for the decay of  $K_L^0 \rightarrow 2\gamma$ , whose final state is similar to the signal signature and may be a potentially non-eliminable source of background.

TABLE 6.1: Main  $K_L^0$  decay background modes and their branching ratios.

Decay mode	Branching Ratio
$K_L \rightarrow \pi^\pm e^\mp \nu_e$	$(40.55 \pm 0.11)\%$
$K_L \rightarrow \pi^\pm \mu^\mp \nu_\mu$	$(27.04 \pm 0.07)\%$
$K_L \rightarrow 3\pi^0$	$(19.52 \pm 0.12)\%$
$K_L \rightarrow \pi^+ \pi^- \pi^0$	$(12.54 \pm 0.05)\%$
$K_L \rightarrow 2\pi^0$	$(8.64 \pm 0.06) \times 10^{-4}$
$K_L \rightarrow 2\gamma$	$(5.47 \pm 0.04) \times 10^{-4}$

760 **Neutron-like background**

761 The neutron originating from the beamline poses a significant background challenge.  
 762 Accurately simulating the in-beam neutron background is nearly impossible, especially  
 763 without a defined mechanism to avoid it. The primary method to mitigate this back-  
 764 ground involves distinguishing the cluster from the photon event.

765 **6.3 Single Cluster Event Selection**

766 The event selection included trigger cuts, kinematic cuts, and veto cuts. The trigger cuts  
 767 were designed to mimic the online trigger effect, while the kinematic cuts and veto cuts  
 768 were implemented to suppress background noise. The kinematic cuts were based on the  
 769 reconstruction quantities of the photon cluster, while the veto cuts were just the criteria  
 770 of hit on the veto counters. In the single cluster study, the signal significance of  $K_L \rightarrow \gamma\bar{\gamma}$   
 771 is only one photon cluster hit on the CsI calorimeter. And other vetoes keep silent in  
 772 time. Which means a very loose condition for hitting events. It is also a challenge for this  
 773 study.

774 **6.3.1 Trigger Selection**

775 The online trigger effect is the source of the difference between the collected data and the  
 776 Monte Carlo simulation. To mimic the online trigger effect and ensure the consistency of  
 777 the data and MC simulation, two trigger selections were implemented: the trigger timing  
 778 cut and the total energy cut.

779 • **Timing window**

780 The online trigger will reject all events with any on-time veto hit, thus a trigger  
 781 timing window as shown in Figure 6.1 is required to eliminate the online trigger  
 782 effect. In the real data taking, due to the 8-ns clock dead time, the real physics data  
 783 timing distribution will be wider than the Monte Carlo simulation. A wide enough  
 784 timing window is selected to cover the distribution inconsistency between the data  
 and the MC simulation.

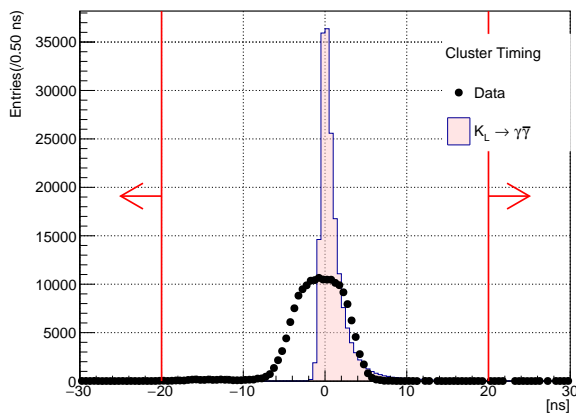


FIGURE 6.1: Distribution of cluster timing after relative timing correction. The dot is from real physics data, and the filled histogram is the MC simulation. The red arrow is the cut-off region.

785     • **Total Energy**

786     The offline energy cut should be larger than the online ET threshold to eliminate the  
 787     online ET trigger effect. The online ET threshold of 300 MeV was required in the  
 788     special run, Thus, the offline energy cut is set as 500 MeV. As shown in the Figure  
 6.2, the signal acceptance is 91.0%

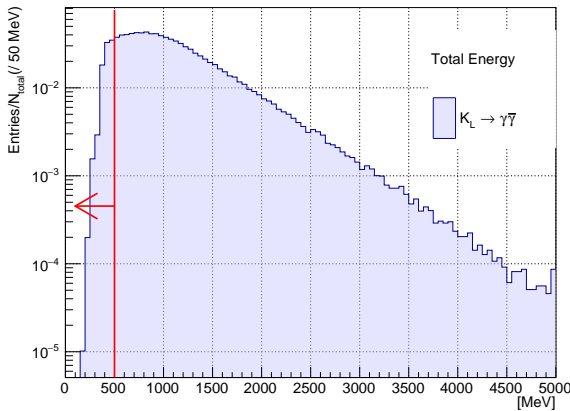


FIGURE 6.2: Distribution of total energy from Monte Carlo simulation. The histogram area is normalized to 1. The red arrow is the cut-off region.

789     790     6.3.2 Kinematic Cuts

791     The  $K_L \rightarrow \gamma\bar{\gamma}$  decays require only one photon cluster on the CsI calorimeter. Therefore,  
 792     the reconstruction of the mother particle is not possible, and also some variables based  
 793     on multiple photon clusters will be absent, such as the vertex position, cluster distance,  
 794     and KL kinematic quantities. As kinematic constraints are lacking, kinematic selection is  
 795     determined by only two variables: the photon hit position and photon energy.

796     • **Innermost and Outermost Photon Hit Position**

797     To prevent the edge of the calorimeter from affecting cluster reconstruction, any  
 798     event that hits the boundary will be removed. Based on the geometry of the calorimeter,  
 799     the outer boundary is evaluated using a radius of hit position,  $R_\gamma$ , while the  
 800     inner boundary is evaluated using the maximum of the absolute values of x and y  
 801     of the photon hit position,  $\max\{|x_\gamma|, |y_\gamma|\}$ . The inner boundary is set as a  $300 \times 300$   
 802     mm<sup>2</sup> box, while the outer boundary is a circle with a radius of 850 mm, as shown  
 803     in Figure 6.3.

804     • **Photon energy**

805     Because of the 1 cluster study, the photon energy is almost equivalent to the total  
 806     energy. Therefore, simply required photon energy to be larger than 500 MeV, which  
 807     is the same as the total energy cut.

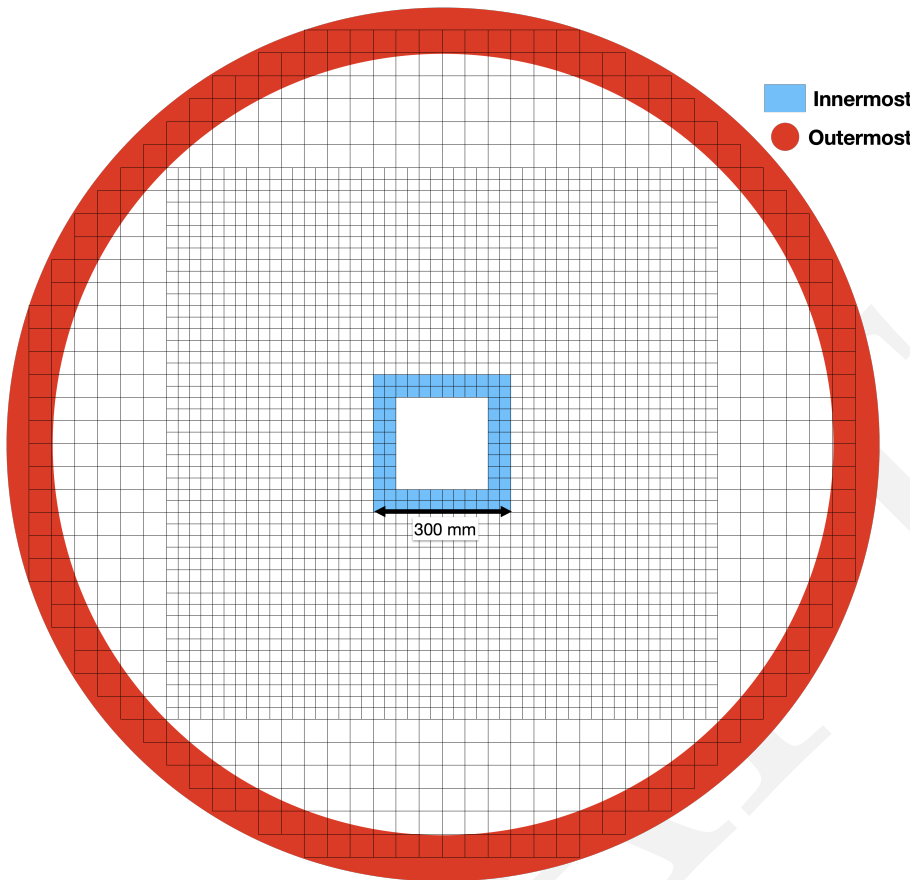


FIGURE 6.3: An upstream view of the CsI calorimeter. The red region is the outermost boundary, while the blue region is the innermost boundary.

### 6.3.3 Veto Cuts

Veto counters are the primary tool for Kaon decay background suppression in the KOTO experiment. The veto hits within the veto timing window and above the veto energy threshold will be tagged as an in-time veto hit. The event with any in-time veto hits will be treated as a background event and rejected. To determine a veto cut, the veto timing window and the energy threshold were required. The energy threshold was simply selected over the online veto and within the precision of the veto counter. The veto timing for veto hits is defined as talk in Section 3.4. To determine the reject window of the veto timing a timing study of each veto counter is required. First, the nominal timing should be determined, the hit close to the nominal timing should be considered as a background hit. Then determined the exact reject window of this veto, because the hit could be produced by the accidental hit not from the  $K_L^0$  decay source. The window decision should consider the signal loss from the accidental hits.

In some veto counters, the source of the veto is predominantly the  $K_L^0$  decay, which results in a Gaussian-like timing distribution, as an example shown in Figure 6.4. For these types of veto counters, the decision on the timing window is straightforward: it involves selecting a range of  $\pm$  a few nanoseconds around the peak position. The width

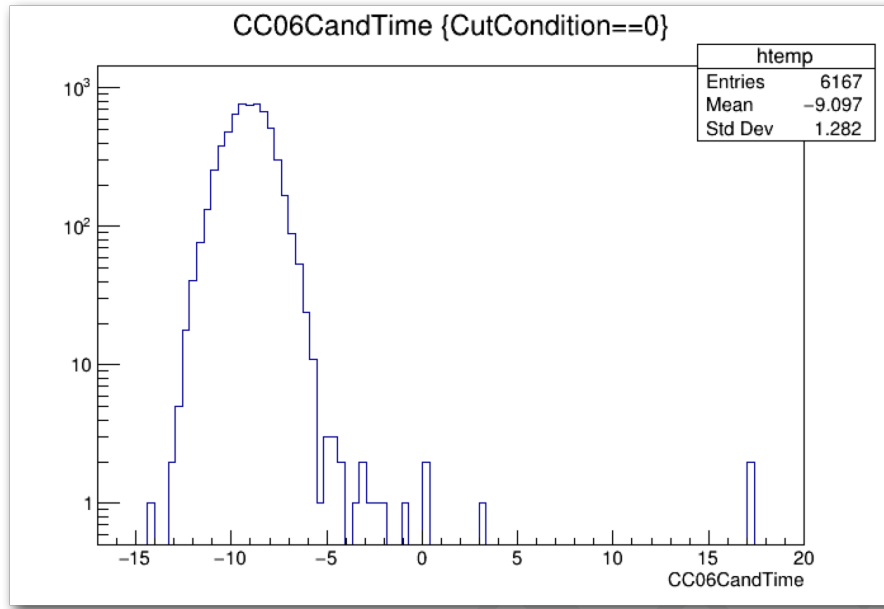


FIGURE 6.4: Distribution of veto timing of CC06.

825 of this window is determined based on the shape of the distribution.

826 However, in some veto counters especially for those surrounding the decay volume,  
 827 the accidental hits are mixed with the background hit. In the following subsection, the  
 828 veto study for these veto counters will be discussed.

### 829 FBAR and NCC

830 The veto timing is defined by the Equation 3.26 The FBAR and NCC are placed upstream  
 831 of the decay volume, the distribution of timing is shown in Figure 6.5. The mechanisms  
 832 of the hits can be categorized into these three types.

- 833 • **Upstream decays**

834 If a  $K_L^0$  decays inside the FBAR chamber, the photon product can hit the FBAR or  
 835 NCC, and the timing accumulated is the nominal time. In the Figure 6.5, is the event  
 836 in decay vertex Z less than 2719 mm region. For NCC the veto timing in this region  
 837 does not have a large variant which is because the  $K_L^0$  decay before the NCC and  
 838 the  $(\Delta z - D)$  in Equation 3.26 is almost a constant and equivalent to the distance  
 839 between NCC and CsI, regardless the decay position. However, because the  $K_L^0$   
 840 decays inside the FBAR, and it has a large volume, the  $(Deltaz - D)$  will variant in  
 841 a large range depending on the decay position.

842 In Figure 6.5, the veto timing of FBAR is broken into two peaks around the nominal  
 843 time, which is because the NCC covers a part of the FBAR detector. In the Figure  
 844 6.5a can show the agreement.

845 • **Backward hit**

846 When a  $K_L^0$  decay in the decay volume, the photon could fly backward and hit the  
 847 NCC and FBAR. Based on the Equation 3.26, the  $(\Delta z - D)/c$  term will be a variant  
 848 and the veto timing will depend on the decay vertex. However, the variate of this  
 849 term is controllable,

$$\Delta z - D \approx \Delta z - (L - \Delta z) = 2\Delta z - L \quad (6.4)$$

$$T_{veto}(\Delta z) \approx \frac{2}{c}\Delta z + T_{mod} - T_{CsI} - L/c \quad (6.5)$$

850 where  $L$  represents the distance between veto and CsI. Equation 3.26 could be seen  
 851 as a function to  $\Delta z$  with a slope  $2/c$ . Which explained the slope of the backward hit  
 852 distribution in Figure 6.5a and 6.5b

853 • **CsI backsplash**

854 As shown in Figure 6.5a and 6.5b, a set of events with a veto timing independent  
 855 of the decay vertex  $z$ . This phenomenon is called "backsplash" which is because the  
 856 calorimeter did not consume all the EM shower but splashed upstream. Because  
 857 the distance of the trajectory is constant, the veto timing will also be constant.

858 Based on these three mechanisms, only the CsI backsplash is the fake signal and the  
 859 other two are the backgrounds. Therefore, the veto timing window for NCC and FBAR  
 860 excludes the backsplash peak, as shown in Figure ?? and ??.

861 **6.4 Background Suppression**

862 There are two main category background sources in this analysis:  $K_L$  decay events and  
 863 Hadronic cluster. Besides these two main background sources, we will also discuss the  
 864 other background sources that we study in this analysis, such as Charge Kaon decays,  
 865 NCC background, and Halo Kaon backgrounds. In the following section, we will talk  
 866 about the background suppression strategy for each category.

867 **6.4.1  $K_L$  Decay Background**

868 In this analysis, we have studied the major three  $K_L^0$  neutral decay channels, like  $K_L^0 \rightarrow$   
 869  $3\pi^0$ ,  $K_L^0 \rightarrow \pi^0\pi^0$ , and  $K_L^0 \rightarrow 2\gamma$ . And also the  $K_{e3}^0$ ,  $K_{\mu 3}^0$ , and  $K_L^0 \rightarrow \pi^+\pi^-\pi^0$ , which is the  
 870 charge decay channel with a large branching ratio.

871 There are 3 kinds of possible mechanisms from  $K_L^0$  decays were found:

872 • **Missing photon**

873 One photon hits the CsI, but other particles hit the dead material of the KOTO  
 874 detector or missing in the beam hole.

875 • **Upstream decay**

876  $K_L^0$  decay upstream of the FBAR, one photon hits the CsI, and the other photon  
 877 missing outside the detector.

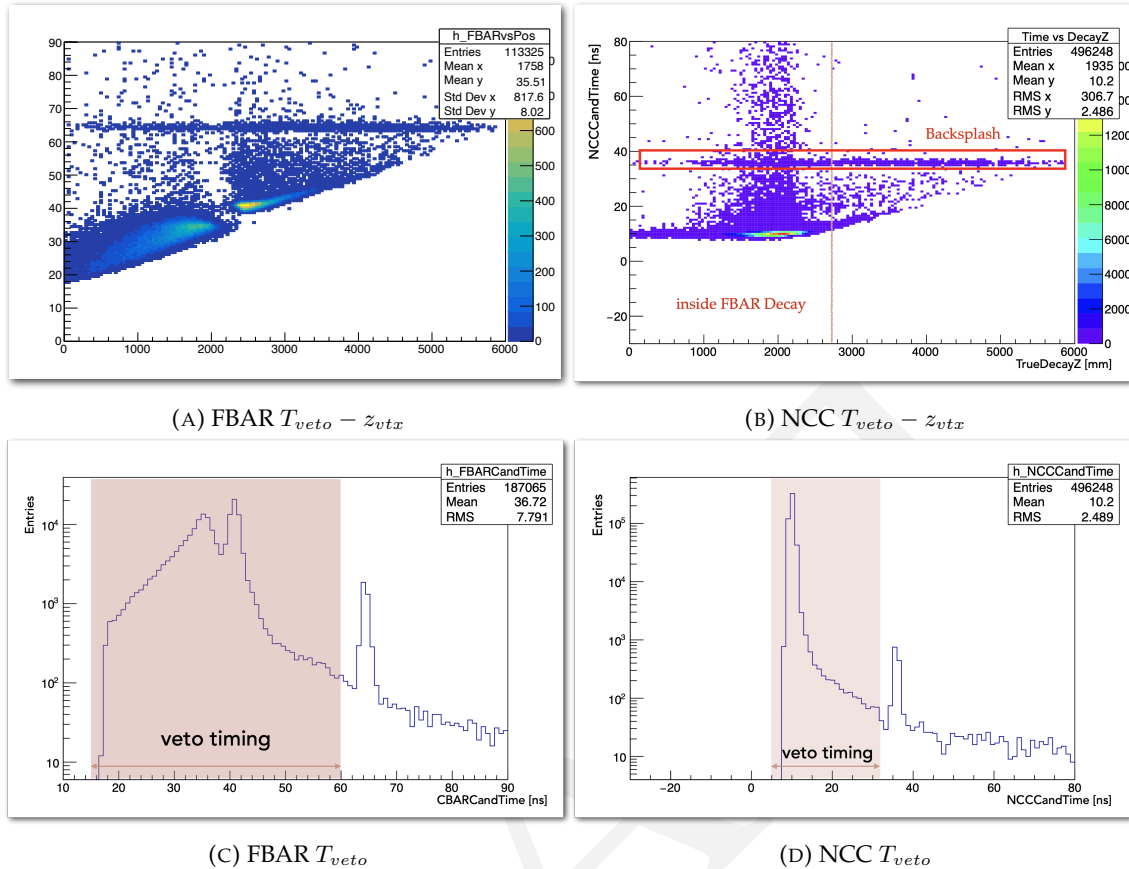


FIGURE 6.5: Temporary plots of FBAR and NCC

878 • **Fusion cluster**

879 The decay position along the Z-axis ( $Z_{vtx}$ ) is too close to the CsI, all decay products  
 880 hit the nearby crystal and are noted as a single cluster by the clustering process. As  
 881 shown in Figure 6.8

882 In this section, all the studied  $K_L^0$  backgrounds will be discussed. All the Monte Carlo  
 883 simulations were applied the accidental overlay.

884  **$K_L^0 \rightarrow 2\gamma$  Background**

885 Because of the extreme hermetic of the KOTO detector, the possibility of missing multiple  
 886 particles is very low. And with our powerful charge veto counter, it is also very difficult  
 887 to miss a charged particle. Therefore,  $K_L^0 \rightarrow 2\gamma$  decay with one missing photon will be  
 888 the primary  $K_L^0$  decay background in this study.

889  $K_L^0 \rightarrow 2\gamma$  background consists of two mechanisms, missing photon and upstream de-  
 890 cay.  $K_L^0 \rightarrow 2\gamma$  has very similar signature with the  $K_L^0 \rightarrow \gamma\bar{\gamma}$ , the only difference is another  
 891 photon is visible. This means if the other photon of  $K_L^0 \rightarrow 2\gamma$  is missing detecting, this  
 892 event will be an ineliminable background in this study. The upstream decay mechanism  
 893 is also having a missing photon. But its decay position is upstream of the FBAR, which

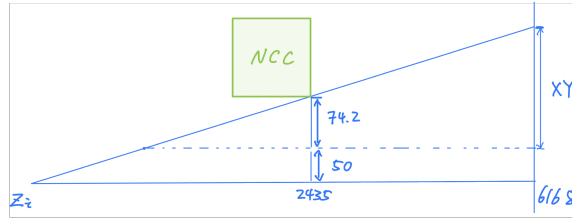


FIGURE 6.6: The schematic geometry diagram of the mechanism of the upstream decay background.

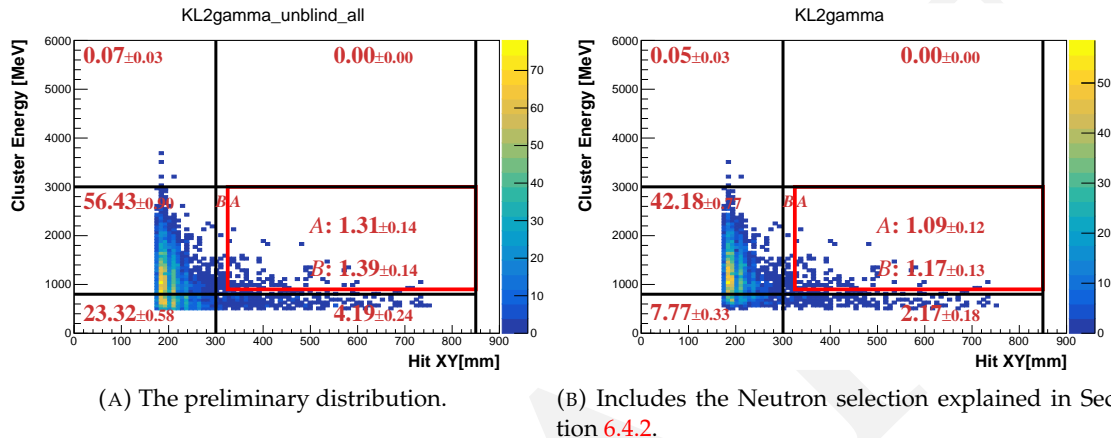


FIGURE 6.7:  $E_\gamma - R_{XY}$  distributions of scattered  $K_L^0 \rightarrow 2\gamma$  decays with various cut. The red frame indicates the signal region. The red number indicates the background level in each region.

894 highly constrains the hit radius ( $R_{XY}$ ) of the cluster. Based on the geometry calculation  
 895 as shown in Figure 6.6, the maximum  $R_{XY}$  of the cluster of upstream decay is 265 mm,  
 896 which is outside the signal region.

897 Figure 6.7 shows the result of  $K_L^0$  selection. A background level of  $1.09 \pm 0.12$  is esti-  
 898 mated in the signal region.

### 899 Other $K_L^0$ decay Backgrounds

900 Besides the  $K_L^0 \rightarrow 2\gamma$  background, the other  $K_L^0$  decay backgrounds are also studied in  
 901 this analysis. Such as  $K_L^0 \rightarrow 3\pi^0$ ,  $K_L^0 \rightarrow \pi^0\pi^0$ ,  $K_{e3}^0$ ,  $K_{\mu 3}^0$  and  $K_L^0 \rightarrow \pi^+\pi^-\pi^0$ . After the  
 902 event selection explained in Section 6.3 and 6.4.2, the event inside the signal region of all  
 903 decays except  $K_L^0 \rightarrow 2\gamma$  is all rejected. All the three mechanisms mentioned above existed  
 904 in these decays. The missing photon is also an ineliminable background, but because the  
 905 decay products are much more than the  $K_L^0 \rightarrow 2\gamma$ , the missing photon background is  
 906 negligible. And the upstream decay background has the same geometry constraint as the  
 907  $K_L^0 \rightarrow 2\gamma$ .

908 The fusion cluster mechanism is the most challenging one because the usual method  
 909 to reject this kind of background is to restrict the decay vertex  $Z$  ( $Z_{vtx}$ ) position in a  
 910 reasonable region. However, in this study, the  $Z_{vtx}$  is not available due to the lack of

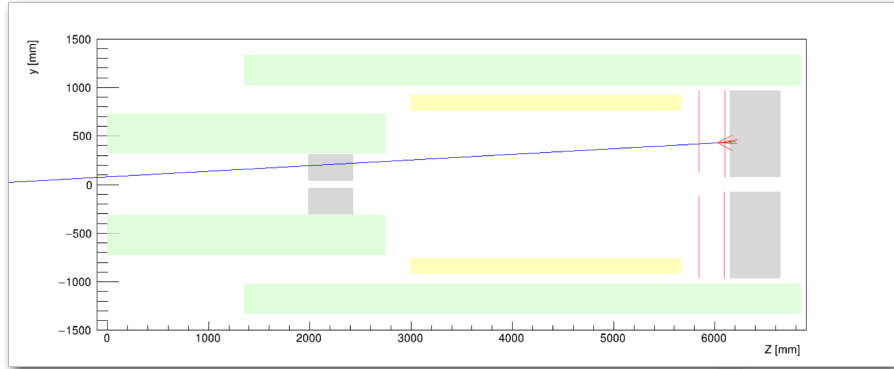


FIGURE 6.8: The schematic geometry diagram of the mechanism of the fusion cluster background.

911 kinematic variables. Therefore, we have to distinguish the fusion cluster from the single  
912 cluster by the cluster shape.

913 The fusion cluster will have a wider shape than the single cluster because the fusion  
914 cluster is the combination of two clusters. Which is more likely to be a hadronic-like clus-  
915 ter. Thus, cluster shape discrimination with deep learning (CSDDL), which is explained  
916 in Section 6.4.2, is sensitive to distinguish the fusion cluster from the single cluster.

917 If we assume the BR to be  $\mathcal{O}(10^{-3})$ , the number of signal events inside the signal region  
918 is  $\mathcal{O}(10^5)$ . That means the Kaon decay background is negligible in this study.

919 Figure 6.9 shows the background level of other  $K_L^0$  decays. The upper limit at 90%  
920 confidence level is estimated in the signal region, as shown in Table 6.3.

## 921 6.4.2 Neutron Background

922 The in-beam neutron background is the dominant background in this study. The neutron  
923 is generated by the hadronic interaction in the beamline, and it is called the "halo neutron"  
924 also. The mechanism is that a neutron hits the CsI calorimeter with one cluster, and there  
925 is no other in-time hit in the rest of the veto counters. Because the signature is the same as  
926 the signal event, the regular background reject method can not reduce this background,  
927 the neutron background is the most challenging in this study. Therefore, we developed  
928 three techniques based on the  $\gamma - n$  discrimination to suppress the neutron background.  
929 The first and most powerful method is to discriminate the neutron cluster by the cluster  
930 shape with deep learning. The second one is discriminating the neutron cluster by the  
931 pulse shape difference with Fourier transformation. The last one is to use the both-end  
932 readout system of CsI crystal to measure the shower depth of the cluster. These three  
933 methods are explained in the following sections.

### 934 Cluster Shape Discrimination with Deep Learning(CSDDL)

935 The Cluster Shape Discrimination (CSD) method is based on the difference in the cluster  
936 shape between the neutron event and the photon event. Because of the shower depth

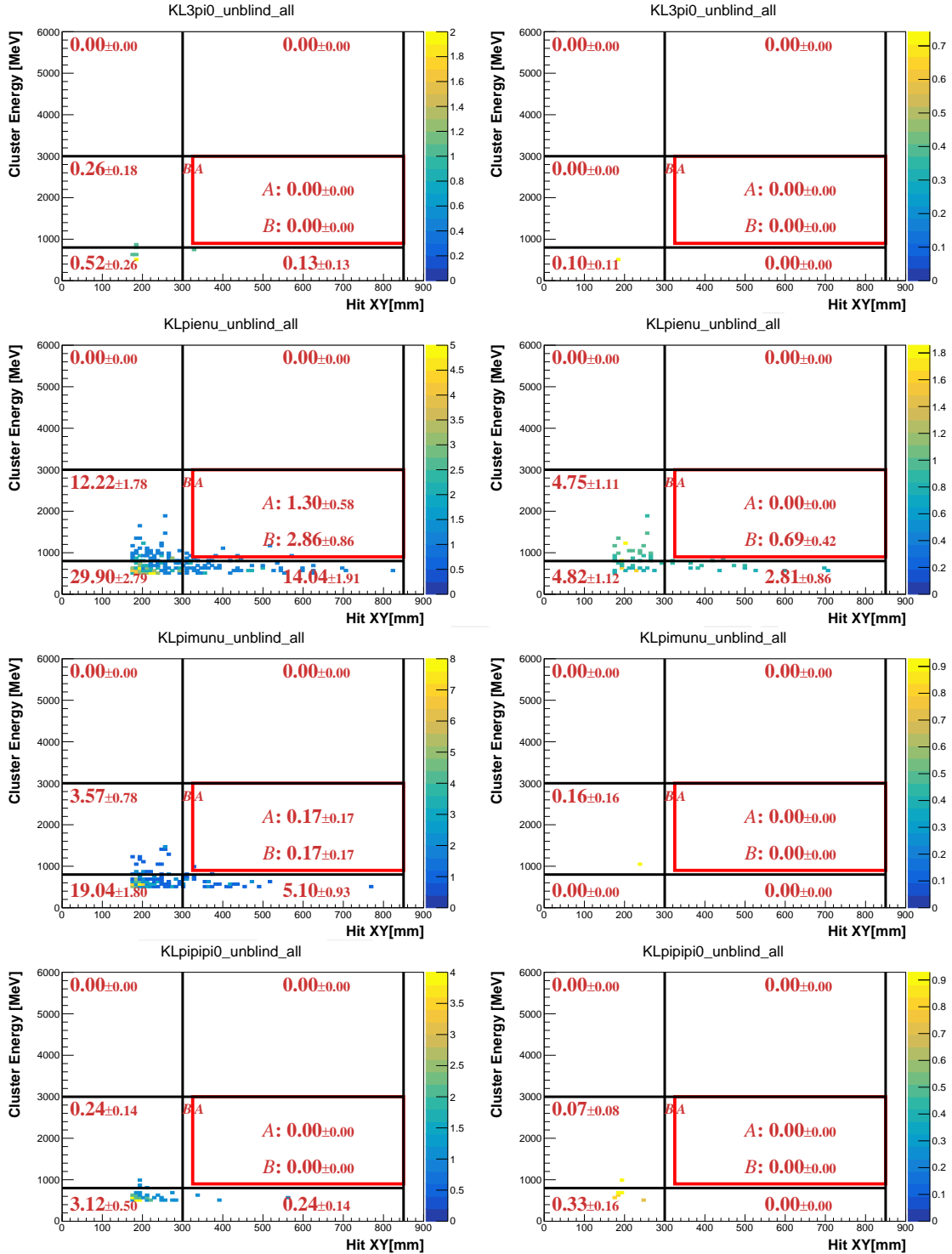


FIGURE 6.9:  $E_\gamma - R_{XY}$  distributions of various background sources after applying all selection cuts. Left-hand side plots exclude the neutron cuts and the right-hand side plots include it. The red frame indicates the signal region. The red number indicates the background level in each region. (Region A indicates the Signal Region and Region B indicates the Blind Region excluding the signal region.)

difference, the neutron-like event will tend to be wider and shallower, and the photon-like event will be more narrow and depth, as shown in Figure 6.10. The difference is very easy to distinguish by the human eye, but it is very difficult to be quantified by the algorithm. Therefore, a neutral network model was developed to quantify the difference of the cluster shape difference.

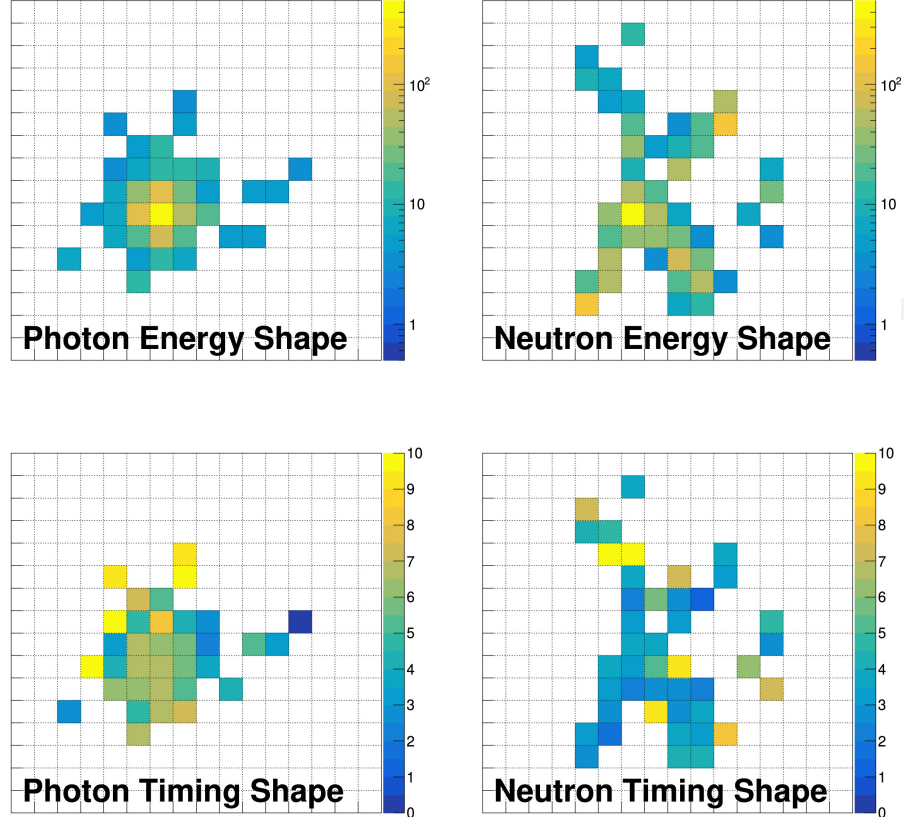


FIGURE 6.10: Example of the energy and timing shapes of photon cluster from the Monte Carlo simulation and neutron cluster from data. The color code represents the deposited energy in MeV and the timing in nanoseconds for each crystal in the cluster. [24]

In this study, the Convolutional Neural Network (CNN) architecture via TensorFlow was employed to classify the neutron and photon clusters by the energy and timing shapes [24]. We use the energy and timing for each crystal the cluster energy and the reconstructed angle on CsI ( $\Phi$ ) as the input parameter of the model training. The architecture of the CNN training process is shown in Figure 6.11.

The model was trained using a photon sample derived from Monte Carlo (MC) simulations and a neutron sample from actual experimental data. Specifically, the photon sample was sourced from the  $K_L^0 \rightarrow \gamma\bar{\gamma}$  decay MC simulation, which includes accidental overlays. The choice of MC for the photon sample is crucial, as the training process relies on the precise measurement of energy and angle of clusters on the CsI detector, which are highly dependent on the assumed decay model. Utilizing a pure photon sample from experimental data, such as the 6-cluster events from  $K_L^0 \rightarrow 3\pi^0$  decay, would risk overfitting the model to this specific decay configuration.

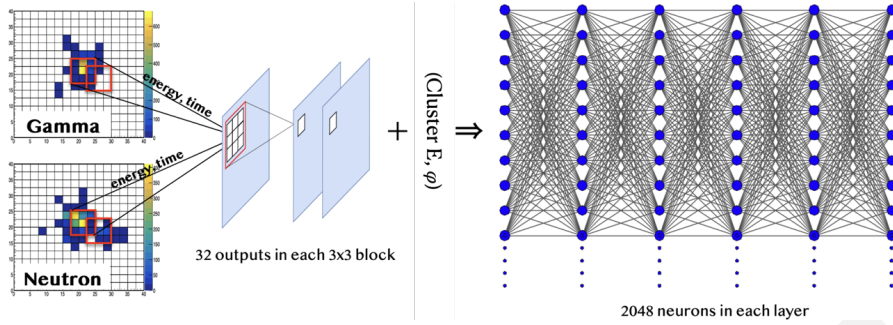


FIGURE 6.11: The architecture of CSD neural network training process.

For the neutron sample, we used data from the Z0-Aluminum (Z0-Al) runs, discussed in Section 4.7. It is important to note that the available Z0-Al data were insufficient for both analysis and training purposes. Consequently, we opted for a pragmatic approach by using data from the last Z0-Al run, specifically RUN82 from 2019, as our training dataset. To validate the suitability of the RUN82 neutron sample, we compared it against a smaller test set of neutrons from RUN85. This comparison, depicted in Figure 6.12, demonstrated a satisfactory alignment between the test results and the training dataset.

The performance of the CSD training result is illustrated by the acceptance of photon clusters in comparison to the rejection of neutron clusters on the CSD score, as shown in Figure ???. This training result gives a very high neutron rejection with high photon acceptance. A selection cut point was decided at a CSDDL score larger than 0.984 based on the 90% signal acceptance. At this point, the inefficiency of the neutron sample is up to  $\mathcal{O}(-\infty)$

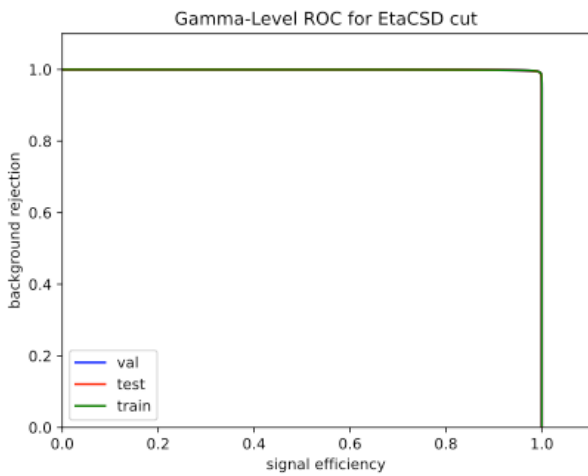


FIGURE 6.12: The ROC curve of the training model. The x-axis is the photon acceptance, and the y-axis is the neutron rejection.

## 968 Fourier transforms for Pulse shape discrimination (FPSD)

969 The difference in shower development of neutron and photon particles also manifests  
970 in the pulse shape difference in the CsI. The neutron pulses have a longer tail than the

971 photon sample because of the difference between the hadronic interaction and electro-  
 972 magnetic interactions, as shown in Figure 6.13

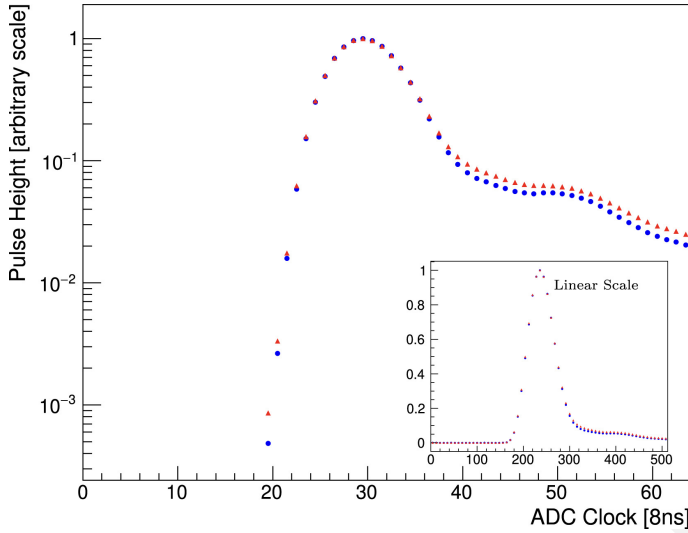


FIGURE 6.13: Average pulse shape of the neutron sample (blue dots) and photon sample (red dots) from one CsI crystal.[24]

973 The datasets for the neutron and photon samples were extracted from the data. The  
 974 photon dataset is obtained from 6-cluster events, predominantly from the  $K_L^0 \rightarrow 3\pi^0$   
 975 decay. The neutron sample, utilized in the CSDDL model testing, comes from the same  
 976 dataset.

977 The FPSD technique is employed to differentiate between neutron and photon clusters  
 978 by analyzing the shape of the ADC waveform. We applied the Discrete Fourier Trans-  
 979 form (DFT) to the raw ADC pulses and subsequently identified distinguishing features  
 980 between neutrons and photons in the frequency domain. Figure 6.14 illustrates the like-  
 981 lihood ratio obtained from this analysis. By setting a threshold that achieves 90% signal  
 982 acceptance, we attained a background rejection efficiency of 89.6% for neutron clusters.

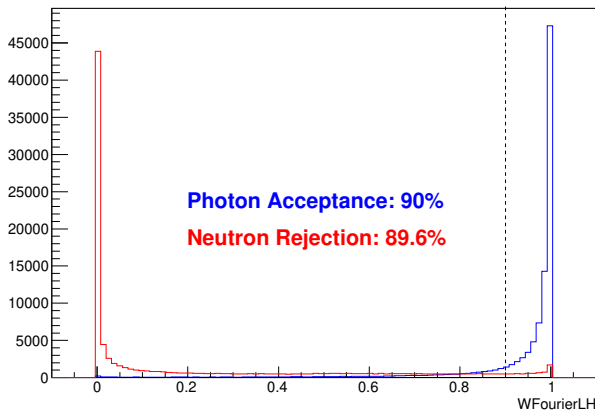


FIGURE 6.14: Distribution of the likelihood ratio for hadronic cluster events (red) and photon cluster events (blue). The photon cluster events are obtained through the  $K_L^0 \rightarrow 3\pi^0$  decay analysis of data. The neutron sample is obtained from neutron data.

983 It is important to highlight that the FPSD algorithm relies on the CsI pulse shape,  
 984 which is not incorporated in the MC simulations. Consequently, to implement this cut  
 985 within the MC simulations, we utilize a table that outlines the FPSD cut efficiency. This  
 986 table is structured based on the cluster energy, its position on the CsI detector, and the

987 specified cut value. When the FPSD is applied to an MC event, the algorithm searches  
 988 for the corresponding cut efficiency in the table and applies this efficiency as a weighting  
 989 factor to the event. This method ensures that the impact of the FPSD cut is accurately  
 990 reflected in the simulation analysis.

### 991 Shower-depth

992 The radiation length for photons is shorter than the interaction length for neutrons, re-  
 993 sulting in different shower depths in the calorimeter for photons and neutrons. Multi-  
 994 pixel photon counters (MPPC) were installed in front of the CsI calorimeter, to consist of  
 995 the both-end readout system with PMT. As shown in Figure 6.15, because of the shower  
 996 depth difference, the timing difference ( $\Delta T$ ) between the front-end (MPPC) and the back-  
 997 end (PMT) is different for the neutron and photon events. The  $\Delta T$  (time difference) for  
 998 photon events tends to be smaller than that for neutron events.

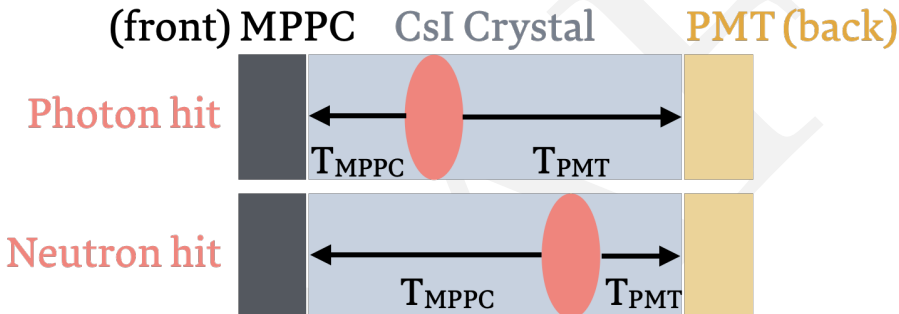


FIGURE 6.15: Illustration of shower depth means. An MPPC is installed on the upstream side. The time difference between the photon arriving upstream and downstream ( $\Delta T = T_{MPPC} - T_{PMT}$ ) is used to measure the depth of the reaction and distinguish between photon events (up) and neutron events (down).

999 The distribution of  $\Delta T$  is shown in figure 6.16. By requiring  $\Delta T$  to be less than 29.5  
 1000 ns, the background rejection efficiency is 84% with a signal loss of 9%. The same data  
 1001 described in Section ?? was used.

## 1002 6.5 Single Event Sensitivity

1003 After considering the 175 mm cut for the low-radius background and all the selection  
 1004 cuts, the single event sensitivity (SES) is calculated by the equation 6.1. The SES is calcu-  
 1005 lated by the  $K_L^0$  yield and the signal acceptance. For this study, The  $K_L^0$  yield is evaluated  
 1006 by the  $K_L^0 \rightarrow 3\pi^0$  decay, because the statistics of the 2-hour special physics data set are  
 1007 not enough to evaluate the yield by  $K_L^0 \rightarrow \pi^0\pi^0$  and  $K_L^0 \rightarrow 2\gamma$  decays. After the selection  
 1008 cuts in Section ??, no event will leave for the  $K_L^0 \rightarrow \pi^0\pi^0$  and  $K_L^0 \rightarrow 2\gamma$  decays. The  
 1009 signal acceptance is evaluated by the Monte Carlo simulation with accidental overlay.  
 1010 After applying all the selection cuts in Section 6.3, the signal acceptance is  $2.66 \times 10^{-3}$ .  
 1011 And the  $K_L^0$  yield is  $1.29 \times 10^{10}$ . The single event sensitivity (SES) is estimated to be  
 1012  $(2.91 \pm 0.05_{stat.}) \times 10^{-8}$ .

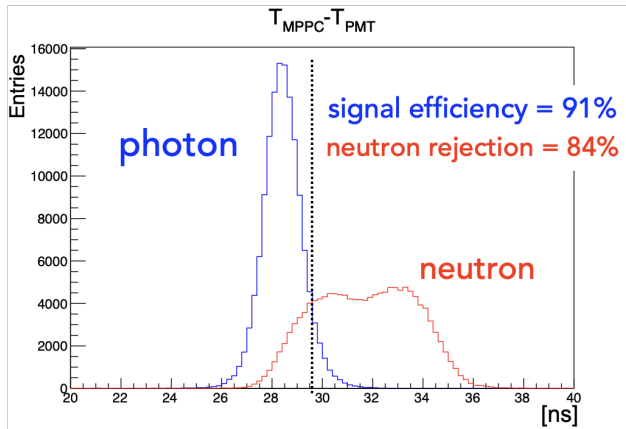


FIGURE 6.16: Distribution of the  $\Delta T$  for neutron events and photon events. The photon cluster events are obtained through the  $K_L^0 \rightarrow 3\pi^0$  decay analysis of data. The neutron sample is obtained by scattering neutrons in the beam with an Al plate.

$$SES = \frac{1}{Y \times A_{sig}} \quad (6.6)$$

$$= \frac{1}{1.29 \times 10^{10} \times 2.66 \times 10^{-3}} \quad (6.7)$$

$$= 2.91 \times 10^{-8} \quad (6.8)$$

### 6.5.1 Systematic Uncertainty of SES

Table 6.2 shows the summary of the systematic uncertainty from each source for the SES.

TABLE 6.2: Summary of Systematic Uncertainty for SES

Sources	Uncertainty
Veto Cuts	6.6%
Kinematic Cuts for $K_L^0 \rightarrow 3\pi^0$	3.3%
Kinematic Cuts for $K_L^0 \rightarrow \gamma\bar{\gamma}$	1.4%
Neutron Cuts for $K_L^0 \rightarrow \gamma\bar{\gamma}$	4.8%
$K_L^0$ momentum spectrum	0.9%
Trigger Effect	1.6%
Branching ratio of $K_L^0 \rightarrow 3\pi^0$	0.6%

## 6.6 Additional Background Source Study

After the event selection, there is a large discrepancy between the data and the simulation in the low-radius region where  $H_{XY} < 175$  mm. As shown in Figure 6.17, the data has a higher level of background in the low-radius region than the simulation. To figure out the contribution of this discrepancy, we studied some extra background sources. In the following subsection, the description of these sources is shown.

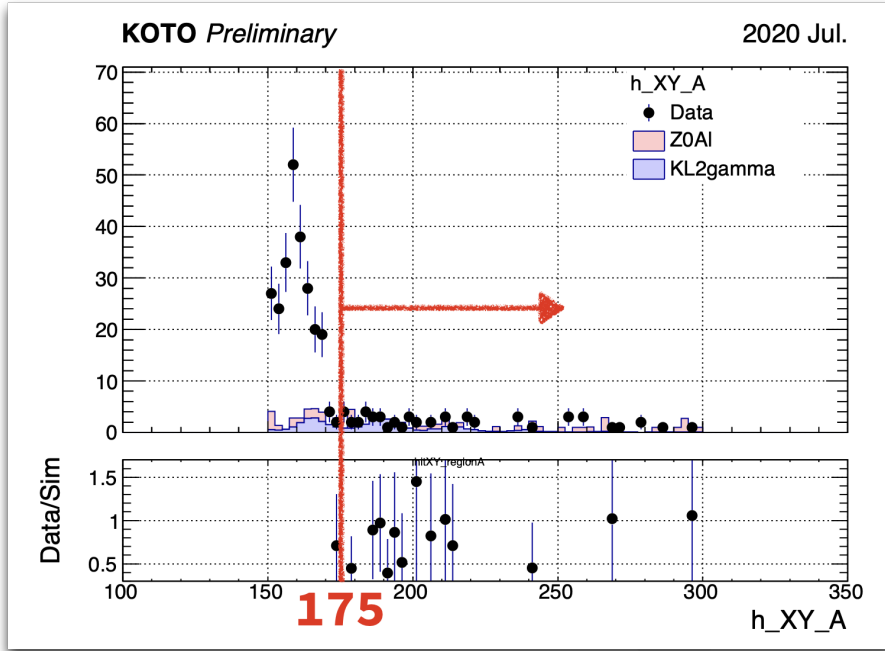


FIGURE 6.17: The  $R_{XY}$  distribution of the region 2. The red line and arrow indicated the cutoff region

### 1021 Upstream Decay from 2nd Collimator

1022 The discrepancy is centered at the region  $R_{XY} < 175$  mm and the maximum  $R_{XY}$  of the  
 1023 cluster of upstream decay is 265 mm, as Section 6.4.1 discussed. This means the upstream  
 1024 decay is a very possible background source. Therefore, we extend the generated position  
 1025 in the Monte Carlo simulation to the start of the 2nd collimator to study the very up-  
 1026 stream decay background. In the usual simulation, the decay position is generated at  
 1027 the end of the 2nd collimator, which is -1507 mm from the upstream of the FBAR. The  
 1028 2nd collimator is 4 m long, which means the new decay position is -5507 mm from the  
 1029 upstream of the FBAR. The geometry calculation, as Figure 6.6, shows that the maximum  
 1030  $R_{XY}$  of the cluster of the new decay position is 133 mm, which completely covers the  
 1031 discrepancy region.

1032 The  $K_L^0 \rightarrow 2\gamma$  decay was studied in this section. The normalization method is the  
 1033 same as the usual Monte Carlo simulation but uses the upstream  $K_L^0 \rightarrow 3\pi^0$  decay ( $Z=-$   
 1034 5507 mm) to estimate the  $K_L^0$  yield.

### 1035 NCC background

1036 When a halo neutron hits NCC, a  $\pi^0$  might be produced by the hadronic interaction. The  
 1037  $\pi^0$  will decay to two photons and if one of them missing due to the inefficiency of the  
 1038 detector, it will become a background source.

1039 **Charge Kaon Decay**

1040 As shown in Figure 4.1, though it is not a large amount, the charge Kaon remains in the  
 1041 beamline.

1042 **Halo  $K_L^0$  Background**

1043 Halo  $K_L^0$  is the  $K_L^0$  particles that are in the periphery of the beam core. As mentioned in  
 1044 Section 4.4.2, the empirical  $K_L^0$  spectrum does not consider the halo  $K_L^0$ . The beamline  
 1045 simulation was required to simulate the halo  $K_L^0$ .

1046 **Summary of the Study**

1047 After the above extra background source study, the discrepancy in the low radius region  
 1048 still exists. Currently, there are no further ideas for the search strategy. It is also possible  
 1049 that just from upstream accidentally hit which is almost impossible to prob because the  
 1050 sources are unknown and unclear. To handle is problem, we simply enlarge the inner-  
 1051 most fiducial cut from 150 mm to 175 mm.

1052 **6.7 Background Level Estimation**

1053 Table 6.3 shows the background level of each background source in the signal region. The  
 upper limit at 90% confidence level is estimated in the signal region.

TABLE 6.3: Number of events predicted for each source inside the signal region

Source		Number of events
$K_L$ decay	$K_L \rightarrow 2\gamma$	$1.09 \pm 0.12$
	$K_L \rightarrow 3\pi^0$	$< 0.18$ (90% C.L.)
	$K_L \rightarrow 2\pi^0$	$< 0.51$ (90% C.L.)
	$K_L \rightarrow \pi^\pm e^\mp \nu_e$	$< 0.27$ (90% C.L.)
	$K_L \rightarrow \pi^\pm \mu^\mp \nu_\mu$	$< 0.25$ (90% C.L.)
	$K_L \rightarrow \pi^+ \pi^- \pi^0$	$< 0.17$ (90% C.L.)
Neutron		$11.57 \pm 4.42$

1054

1055 Figure ?? shows the  $E_\gamma$ -  $H_{XY}$  distribution of physics data for each region. In the side-  
 1056 band region, the expected number shows agreement with the observations. The back-  
 1057 ground level in the signal region is  $12.66 \pm 4.42$ .

1058 **6.8 Unbind the Signal Region**

1059 After all the studies, we decided to open the box. The observed result is 13 events inside  
 1060 the signal region, as shown in Figure 6.19, which agrees with the expected number of  
 1061 events. To estimate the Branching ratio of the  $K_L^0 \rightarrow \gamma\bar{\gamma}$ , the Feldman-Cousins method

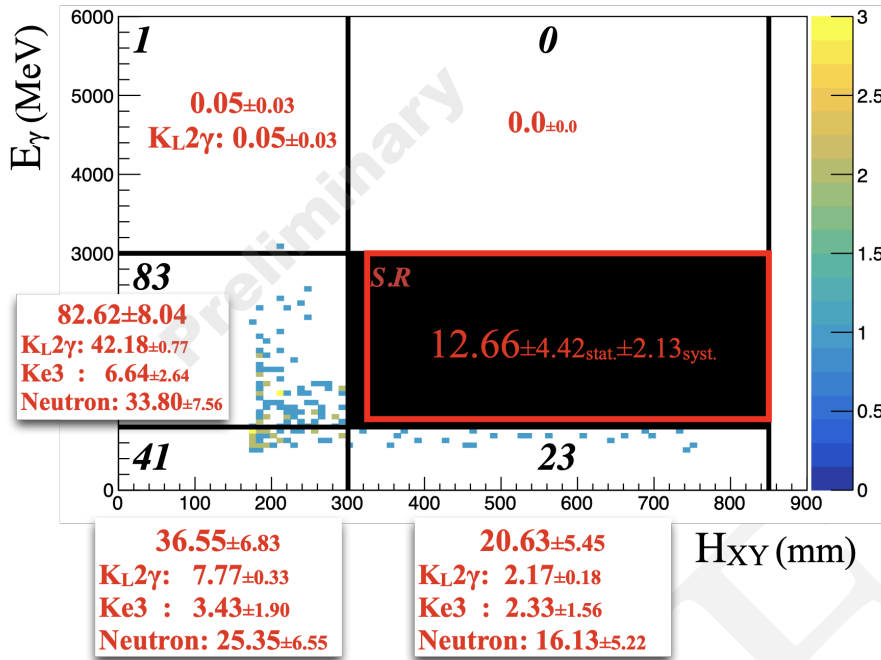


FIGURE 6.18:  $E_\gamma$ -  $H_{XY}$  distribution of physics data after applying all the selection cuts. The black box is the blind region the red frame is the signal region. The black (red) number is the observed (expected) number of events.

1062 was adopted, because we still have numerous expected backgrounds in the signal region.  
 1063 After the calculation, an upper limit of branching ratio was obtained at 90% C.L.,

$$\mathcal{BR}(K_L^0 \rightarrow \gamma\bar{\gamma}) < 11.9 \times SES(K_L^0 \rightarrow \gamma\bar{\gamma}) \quad (6.9)$$

$$= 3.47 \times 10^{-7} (90\% \text{ C.L.}) \quad (6.10)$$

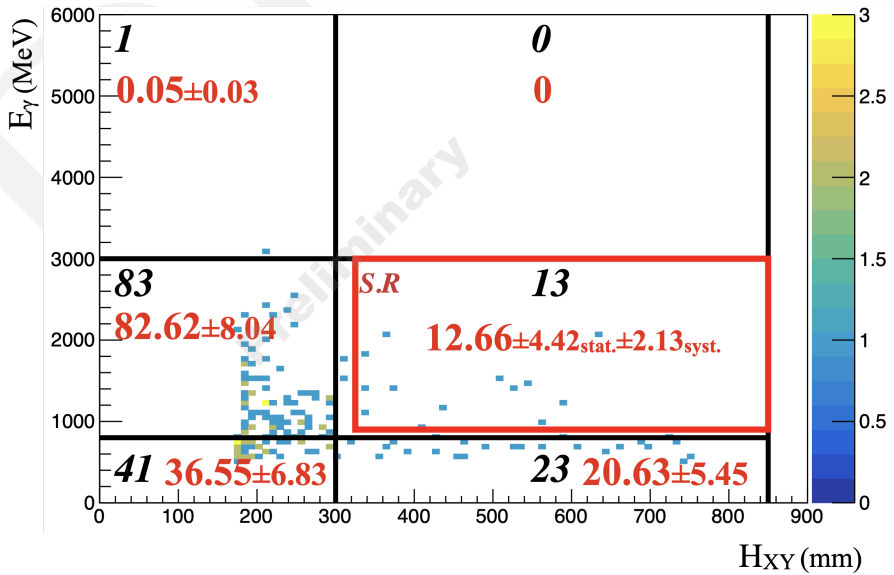


FIGURE 6.19:  $E_\gamma$ -  $H_{XY}$  distribution of physics data after open the blind box. The black (red) number is the observed (expected) number of events.

1064 **Chapter 7**

1065 **Conclusion and Discussion**

1066 We present the study of  $K_L^0 \rightarrow \gamma\bar{\gamma}$  search in this thesis. The  $K_L^0 \rightarrow \gamma\bar{\gamma}$  analysis is based  
1067 on the 2-hour spacial run taken in 2020. The total number of  $K_L^0$  decays is  $1.29 \times 10^{10}$ ,  
1068 which is estimated by the  $K_L^0 \rightarrow 3\pi^0$  decay. Two kinds of backgrounds are major in  
1069 this analysis, the  $K_L^0$  decay background and the in-beam neutron background. We use  
1070 different methods to suppress these two backgrounds.

1071 To suppress the  $K_L^0$  decay source background, we use the veto system of the KOTO  
1072 detector. Because the one cluster signal signature is a pretty strict criterion to reject most  
1073 of the  $K_L^0$  decay channel with multiple products in the final state. The only background  
1074 that can pass the veto system is the  $K_L^0 \rightarrow 2\gamma$  channel. With one photon missing due to  
1075 detection inefficiency, the  $K_L^0 \rightarrow 2\gamma$  background cannot be rejected. Thanks to the her-  
1076 metric veto system of the KOTO Experiment, the  $K_L^0 \rightarrow 2\gamma$  background is well suppressed  
1077 by the veto system with only  $1.09 \pm 0.12_{stat.} \pm 0.05_{syst.}$  events estimated remaining in the  
1078 signal region.

1079 To suppress the in-beam neutron background, we use three techniques based on the  
1080  $n - \gamma$  discrimination to suppress the neutron background. The first one is cluster shape  
1081 discrimination based on deep learning, which is the most powerful technique to classify  
1082 neutrons and photons. The other two are the pulse shape discrimination based on the  
1083 Fourier Transform and the show-depth measure by the CsI both-end readout system.  
1084 These two techniques also provide a good rejection power on the neutron background.  
1085 Combining these three techniques, rejected the neutron background by  $\mathcal{O}(10^{-3})$  for the  
1086 single cluster with 83.9% signal acceptance. After all the selections, the total neutron  
1087 background is estimated to be  $11.57 \pm 4.42_{stat.} \pm 2.13_{syst.}$  events in the signal region.

1088 Combining all the background sources we have studied, the total background is esti-  
1089 mated to be  $12.66 \pm 4.42_{stat.} \pm 2.13_{syst.}$  events in the signal region. After the background  
1090 suppression study, we open the blind region box. The observed events in the signal re-  
1091 gion are 13 events, which is consistent with the background estimation. Because we still  
1092 have a large estimation of the background in the signal region, we decided to use the  
1093 Feldman-Cousins method to evaluate the upper limit on the  $K_L^0 \rightarrow \gamma\bar{\gamma}$  branching ratio.  
1094 At 90% C.L., the upper limit on the  $K_L^0 \rightarrow \gamma\bar{\gamma}$  branching ratio is  $3.47 \times 10^{-7}$ .

## 1095 7.1 Discussion for Next Step

1096 To advance the  $K_L^0 \rightarrow \gamma\bar{\gamma}$  search, the next crucial step is to enhance the sensitivity of  
 1097 the analysis. Given the large number of background events within the signal region,  
 1098 collecting more physics data is not an immediate priority. In the current study, the pri-  
 1099 mary background source is beam neutrons. Despite employing three techniques to sup-  
 1100 press this background, the neutron background remains significantly estimated in the  
 1101 signal region. Thus, increasing the effectiveness of neutron background suppression is  
 1102 paramount. Additionally, enhancing the statistical power of the analysis is vital. At  
 1103 present, the neutron background estimation is plagued by considerable statistical uncer-  
 1104 tainty.

1105 For the next step, I suggest utilizing previously collected data to enhance the statistics.  
 1106 Since we do not use or need the single-cluster Z0-Al data in the analysis, we can repur-  
 1107 pose the data we have already collected. Specifically, data taken before the 2020 RUN85,  
 1108 which includes both physics and Z0-Al data, can be utilized. For single-cluster physics  
 1109 data, we can use the normalization trigger in the physics data, which does not filter based  
 1110 on the number of clusters. For Z0-Al data, we can continue using the two-cluster Z0-Al  
 1111 data, consistent with our current strategy.

## 1112 7.2 Massive Dark Photon Search

1113 We finished the massless dark photon study, the massive dark photon should be also an  
 1114 interesting topic to study. In this study, the search strategy is not strict with the mass of  
 1115 the dark photon. Therefore, the massive dark photon search will use the same strategy as  
 1116 the massless dark photon search. The only need to change is the mass of the dark photon  
 1117 in the MC simulation. Figure 7.1 shows the Upper limit and signal acceptance of each  
 1118 mass of the dark photon.

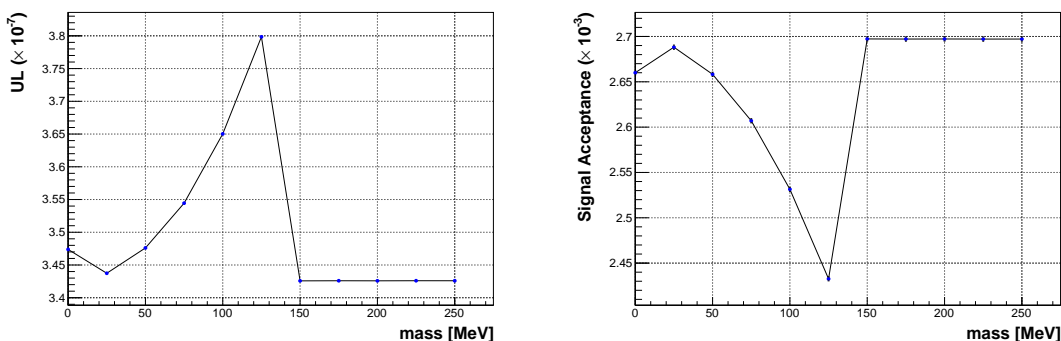


FIGURE 7.1: Upper limit (left) and signal acceptance (right) for each mass dark photon from 0 MeV to 250 MeV, step 25 MeV

# 1119 Bibliography

- 1120 [1] Particle Data Group et al. "Review of Particle Physics". In: *Progress of Theoretical*  
 1121 and *Experimental Physics* 2022.8 (Aug. 2022), p. 083C01. ISSN: 2050-3911. DOI: [10.1093/ptep/ptac097](https://doi.org/10.1093/ptep/ptac097).
- 1123 [2] Marco Fabbrichesi, Emidio Gabrielli, and Gaia Lanfranchi. *The Physics of the Dark*  
 1124 *Photon: A Primer*. Springer International Publishing, 2021. ISBN: 9783030625191.  
 1125 DOI: [10.1007/978-3-030-62519-1](https://doi.org/10.1007/978-3-030-62519-1).
- 1126 [3] Jhih-Ying Su and Jusak Tandean. "Kaon decays shedding light on massless dark  
 1127 photons". In: *The European Physical Journal C* 80.9 (2020), p. 824. DOI: [10.1140/epjc/s10052-020-8338-3](https://doi.org/10.1140/epjc/s10052-020-8338-3).
- 1129 [4] Andrzej J. Buras et al. " $K^+ \rightarrow \pi^+ \nu \bar{\nu}$  and  $K_L \rightarrow \pi^0 \nu \bar{\nu}$  in the Standard Model: status  
 1130 and perspectives". In: *Journal of High Energy Physics* 2015.11 (2015). DOI: [10.1007/jhep11\(2015\)033](https://doi.org/10.1007/jhep11(2015)033).
- 1132 [5] Shoji Nagamiya. "Introduction to J-PARC". In: *Progress of Theoretical and Experi-  
 1133 mental Physics* 2012.1 (Oct. 2012). 02B001. ISSN: 2050-3911. DOI: [10.1093/ptep/pts025](https://doi.org/10.1093/ptep/pts025).
- 1135 [6] Masanori Ikegami. "Beam commissioning and operation of the J-PARC linac". In:  
 1136 *Progress of Theoretical and Experimental Physics* 2012.1 (Sept. 2012). 02B002. ISSN:  
 1137 2050-3911. DOI: [10.1093/ptep/pts019](https://doi.org/10.1093/ptep/pts019).
- 1138 [7] Hideaki Hotchi et al. "Beam commissioning and operation of the Japan Proton Ac-  
 1139 celerator Research Complex 3-GeV rapid cycling synchrotron". In: *Progress of The-  
 1140 retical and Experimental Physics* 2012.1 (Sept. 2012). 02B003. ISSN: 2050-3911. DOI:  
 1141 [10.1093/ptep/pts021](https://doi.org/10.1093/ptep/pts021).
- 1142 [8] Tadashi Koseki et al. "Beam commissioning and operation of the J-PARC main ring  
 1143 synchrotron". In: *Progress of Theoretical and Experimental Physics* 2012.1 (Dec. 2012).  
 1144 02B004. ISSN: 2050-3911. DOI: [10.1093/ptep/pts071](https://doi.org/10.1093/ptep/pts071).
- 1145 [9] Shunzo Kumano. "J-PARC Hadron Physics and Future Possibilities on Color Trans-  
 1146 parency". In: *Physics* 4 (May 2022), pp. 565–577. DOI: [10.3390/physics4020037](https://doi.org/10.3390/physics4020037).
- 1147 [10] K. Takahashi H.and Agari et al. "Indirectly water-cooled production target at J-  
 1148 PARC hadron facility". In: *Journal of Radioanalytical and Nuclear Chemistry* 305.3  
 1149 (2015), pp. 803–809. ISSN: 1588-2780. DOI: [10.1007/s10967-015-3940-9](https://doi.org/10.1007/s10967-015-3940-9).
- 1150 [11] T. Shimogawa. "Design of the neutral K0L beamline for the KOTO experiment". In:  
 1151 *Nuclear Instruments and Methods in Physics Research Section A: Accelerators, Spectrome-  
 1152 ters, Detectors and Associated Equipment* 623.1 (2010). 1st International Conference on  
 1153 Technology and Instrumentation in Particle Physics, pp. 585–587. ISSN: 0168-9002.  
 1154 DOI: <https://doi.org/10.1016/j.nima.2010.03.078>.

- 1155 [12] D. Naito et al. "Development of a low-mass and high-efficiency charged-particle  
 1156 detector". In: *Progress of Theoretical and Experimental Physics* 2016.2 (Feb. 2016). 023C01.  
 1157 ISSN: 2050-3911. DOI: [10.1093/ptep/ptv191](https://doi.org/10.1093/ptep/ptv191).
- 1158 [13] Yosuke Maeda. *Charged-particle veto detector for the  $K_L \rightarrow \pi^0\nu\bar{\nu}$  study in the J-PARC  
 1159  $K^0\text{TO}$  experiment.* 2012.
- 1160 [14] Daichi Naito et al. "Evaluation of the Inefficiency of a Charged Particle Detector  
 1161 for the KOTO Experiment". In: *JPS Conf. Proc.* 8 (2015), p. 024003. DOI: [10.7566/JPSCP.8.024003](https://doi.org/10.7566/JPSCP.8.024003).
- 1163 [15] C. Lin. "Study of  $K_L^0 \rightarrow \pi^0\nu\bar{\nu}$  and  $K_L^0 \rightarrow \pi^0\gamma\gamma$  with the Cluster-Finding Trigger at  
 1164 KOTO". National Taiwan University, 2021. DOI: [10.6342/NTU202102308](https://doi.org/10.6342/NTU202102308).
- 1165 [16] Chieh Lin. "Data-Acquisition System Upgrade for the KOTO Experiment". In: *PoS  
 1166 ICHEP2022* (2022), p. 242. DOI: [10.22323/1.414.0242](https://doi.org/10.22323/1.414.0242).
- 1167 [17] E. Iwai et al. "Performance study of a prototype pure CsI calorimeter for the KOTO  
 1168 experiment". In: *Nuclear Instruments and Methods in Physics Research Section A: Ac-  
 1169 celerators, Spectrometers, Detectors and Associated Equipment* 786 (2015), pp. 135–141.  
 1170 ISSN: 0168-9002. DOI: <https://doi.org/10.1016/j.nima.2015.02.046>.
- 1171 [18] J. Allison et al. "Geant4 developments and applications". In: *IEEE Transactions on  
 1172 Nuclear Science* 53.1 (2006), pp. 270–278. DOI: [10.1109/TNS.2006.869826](https://doi.org/10.1109/TNS.2006.869826).
- 1173 [19] S. Agostinelli et al. "Geant4—a simulation toolkit". In: *Nuclear Instruments and Meth-  
 1174 ods in Physics Research Section A: Accelerators, Spectrometers, Detectors and Associated  
 1175 Equipment* 506.3 (2003), pp. 250–303. ISSN: 0168-9002. DOI: [https://doi.org/10.1016/S0168-9002\(03\)01368-8](https://doi.org/10.1016/S0168-9002(03)01368-8).
- 1177 [20] J. Allison et al. "Recent developments in Geant4". In: *Nuclear Instruments and Meth-  
 1178 ods in Physics Research Section A: Accelerators, Spectrometers, Detectors and Associated  
 1179 Equipment* 835 (2016), pp. 186–225. ISSN: 0168-9002. DOI: <https://doi.org/10.1016/j.nima.2016.06.125>.
- 1181 [21] Kazufumi Sato. "Measurement of the CsI calorimeter performance and KL momen-  
 1182 tum spectrum for the J-PARC KOTO experiment". Ph.D. thesis. Osaka University,  
 1183 2015.
- 1184 [22] Particle Data Group et al. "Review of Particle Physics". In: *Progress of Theoretical and  
 1185 Experimental Physics* 2020.8 (Aug. 2020). 083C01. ISSN: 2050-3911. DOI: [10.1093/ptep/ptaa104](https://doi.org/10.1093/ptep/ptaa104).
- 1187 [23] Kota Nakagiri. "Search for the Decay  $K_L^0 \rightarrow \pi^0\nu\bar{\nu}$  at the J-PARC KOTO Experi-  
 1188 ment". Ph.D. thesis. Kyoto University, 2019. DOI: [10.14989/doctor.k21564](https://doi.org/10.14989/doctor.k21564).
- 1189 [24] Y. C. Tung et al. "Suppression of neutron background using deep neural network  
 1190 and Fourier frequency analysis at the KOTO experiment". In: *Nucl. Instrum. Meth.  
 1191 A* 1059 (2024), p. 169010. DOI: [10.1016/j.nima.2023.169010](https://doi.org/10.1016/j.nima.2023.169010).